A Study of Charge Accumulation and Spacer Flashover in Compressed Gas Insulation

By

Jianping Zhou

B. A. Sc. (Electrical Engineering) Xi'an Jiaotong University, China
M. A. Sc. (Electrical Engineering) Xi'an Jiaotong University, China

A THESIS SUBMITTED IN PARTIAL FULFILLMENT OF
THE REQUIREMENTS FOR THE DEGREE OF
DOCTOR OF PHILOSOPHY

in

THE FACULTY OF GRADUATE STUDIES
ELECTRICAL ENGINEERING

We accept this thesis as conforming
to the required standard

THE UNIVERSITY OF BRITISH COLUMBIA

June 1991

In presenting this thesis in partial fulfilment of the requirements for an advanced degree at the University of British Columbia, I agree that the Library shall make it freely available for reference and study. I further agree that permission for extensive copying of this thesis for scholarly purposes may be granted by the head of my department or by his or her representatives. It is understood that copying or publication of this thesis for financial gain shall not be allowed without my written permission.

Department of Electrical Engineering

The University of British Columbia
Vancouver, Canada

Date Oct. 11, 1991

DE-6 (2/88)

Abstract

Compressed gas insulated substation (GIS) and transmission line (GITL) equipment have been developed rapidly throughout the world during the past decades. Compactness is the main advantage of GIS and GITL over conventional air-insulated substations and transmission lines. Sulphur hexafluoride (SF_6) is used as an insulation gas in GIS and GITL because of its excellent insulating properties. Supporting spacers are identified as the most likely places for flashover to occur and they often determine the overall strength of a system. For energized system, surface charges have been observed on spacer surfaces and are considered to play an important role for anomalous flashover of a GIS or GITL system. The purpose of this research is to study the mechanisms and factors governing the magnitude and distribution of surface charges and their influence on flashover voltage.

In this investigation, experiments to study surface charge accumulation under different experimental conditions have been conducted, with a rod-spacer-plane electrode system. The parameters varied are applied voltage levels, insulating gases, gas pressures, spacer materials, rod electrode diameters, and the duration of applied voltages. Experiments with impulse voltage pre-charging were also conducted. It was found that the mechanisms of surface charging are corona, gas conduction, and photoionization. Surface charge magnitude and distribution

are strongly field dependent and are related to the duration of voltage application. Spacers in SF_6 gas accumulate less charges on the surface than in air and nitrogen , for a given geometry, spacer material, voltage, and gas pressure.

In order to determine the effect of surface charges on overall electric field, a surface charge simulation program (the SSM program) was developed to calculate the overall electric field when there are surface charges on a spacer surface. The calculation results show that surface charges significantly distort the overall electric field magnitude, field direction, and distributions, which may explain the anomalous flashover in GIS/GITL systems. It was found that the flashover propagation field on a PTFE spacer surface may be between 6 kV/cm and 10 kV/cm.

High speed photographic observations, with an image intensifier, are suggested to examine the propagation of a flashover. It may, therefore, be possible that, a reasonable model to predict flashover in SF_6 gas can be built by comparing the flashover propagation model with the electric field pattern on a spacer surface. The role of photoionization near the spacer surface in charge accumulation should also be studied in greater detail.

Contents

List of Figures

Acknowledgments

I wish to express gratitude to my parents, who inspired me to undertake this venture. I wish to thank my sister Jianji and my brother Jim Jianpeng for their understanding, support and encouragement during my doctoral program.

I wish to express my sincere appreciation to my supervisor, Prof. K.D. Srivastava, for his encouragement, readiness to help, and patience. Prof. K.D. Srivastava, despite his very busy schedule, always found time to have very spirited discussions with me and gave me excellent guidance about my research. He has been not only a great supervisor but also a wonderful friend.

I would like to thank Dr. S. E. Cherukupalli for sharing his vast experience and for offering many constructive suggestions during my thesis work. I would also like to thank Dr. J. B. Neilson from Power Tech for the many interesting discussions during my research. I am grateful to all the staff in Electrical Engineering Workshop for all their help with the experimental research conducted in the High Voltage Lab at UBC.

I thank all my colleagues, friends, and office-mates for making my stay at UBC a great one.

Chapter 1

Introduction

During the past decades, development of compressed gas insulated substation (GIS) and transmission line (GITL) equipment has progressed rapidly throughout the industrialized world. The number of GIS in Canada has grown steadily since the first installation in 1975, to the point that more than 160 breaker-bays of GIS were in service in 1985 [1], figure 1.1 . The initial installations of compressed-gas insulated transmission lines or cables (GITL) were in the U.S.A. in 1968/1969 [2–7]. The total length of GITL system installed throughout the world increases as shown in figure 1.2.

The technical, economic and practical aspects were evaluated during an international symposium on GIS [8]. Compactness is the main advantage of GIS over conventional air-insulated substations. This is an important factor in areas where land is expensive or very scarce. Capital costs of GIS are generally higher than those for open-air stations but the maintenance costs are lower. The attempts to design semi-flexible and flexible gas cables are already underway to reduce

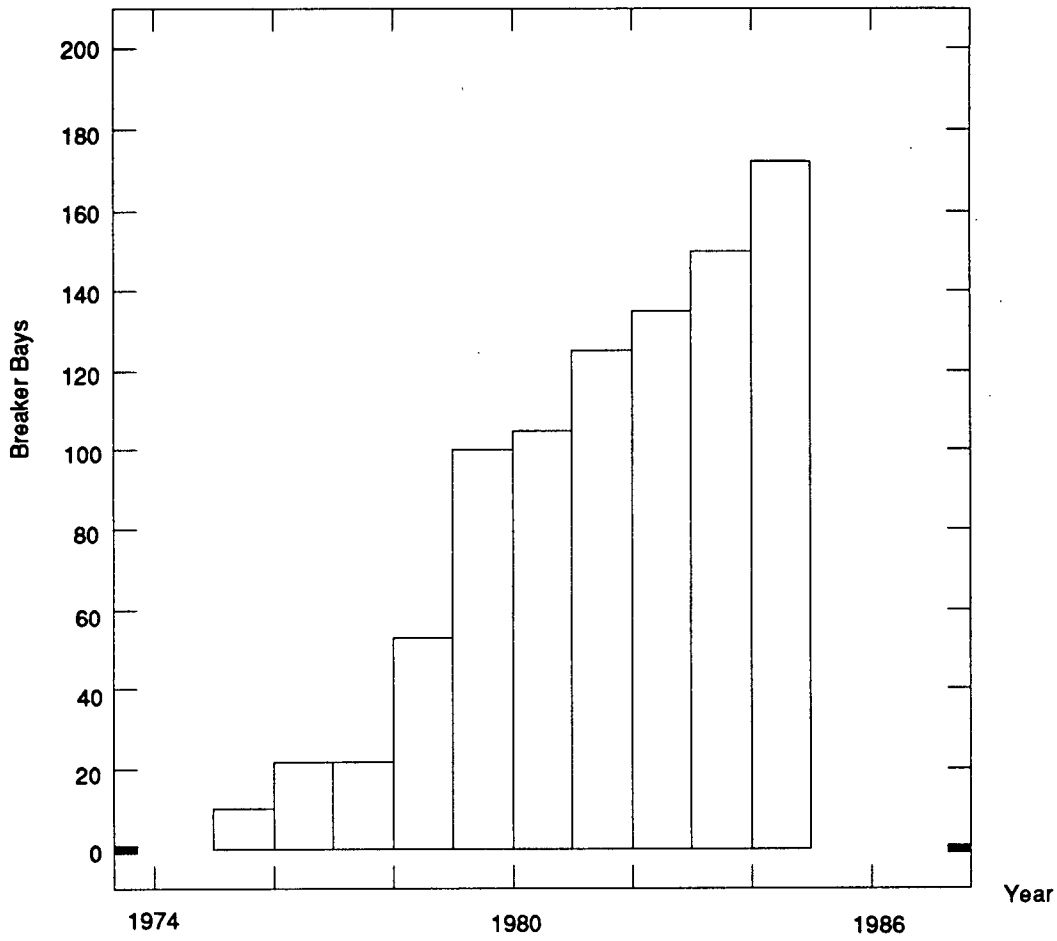

Figure 1.1 Cumulative breaker-bays of GIS in Canada as a function of time [1].

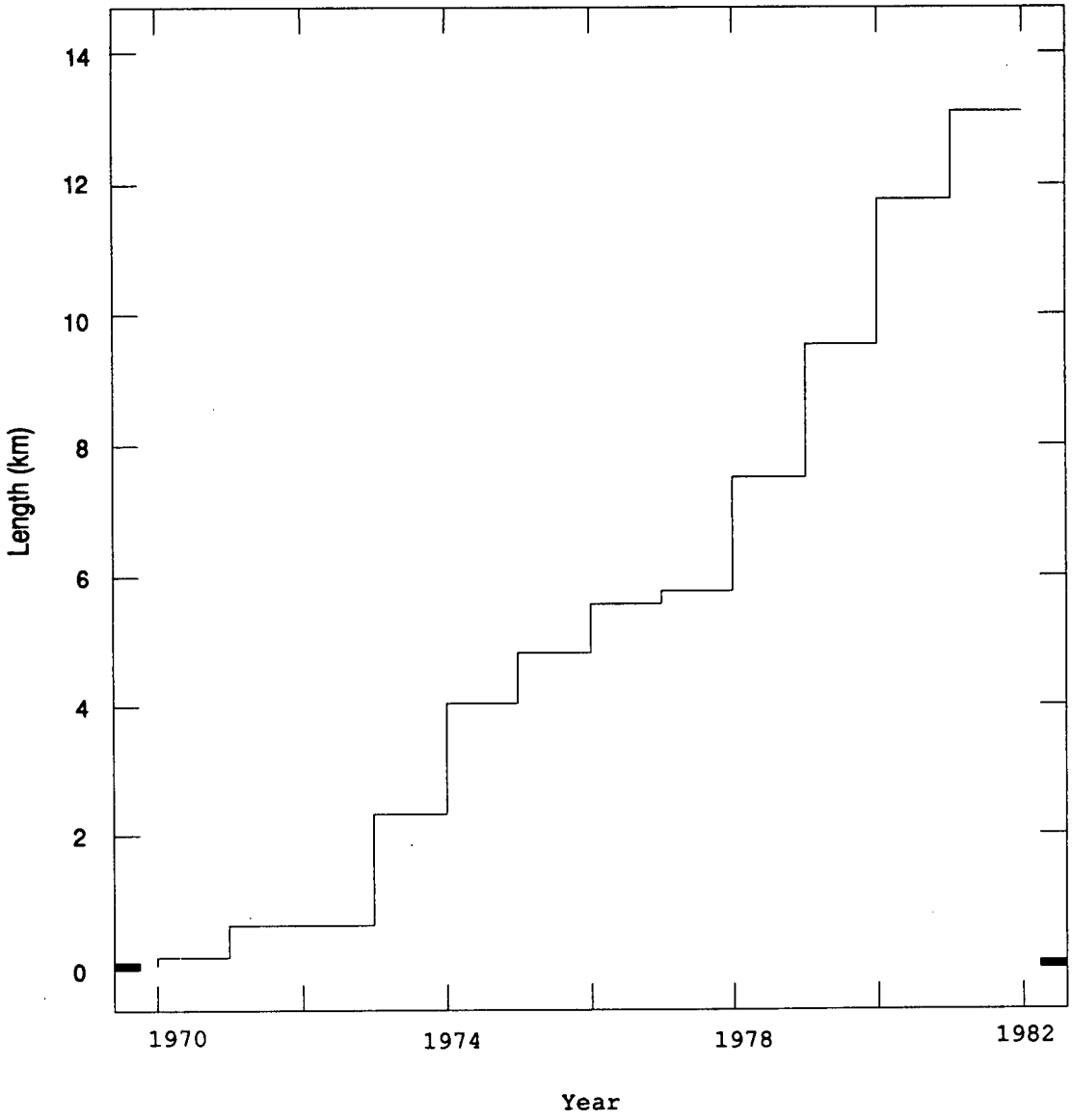

Figure 1.2 Total length of GITL systems installed throughout the world [4].

the number of field joints so that the associated problems will be reduced and reliability will be improved.

Sulphur hexafluoride (SF_6) is used as an insulation gas in GIS and GITL because of its excellent insulating properties. SF_6 is an electronegative or electron attaching gas [9]. The attachment may be direct

$$SF_6 + e^- \rightarrow SF_6^- \tag{1.1}$$

or dissociative

$$SF_6 + e^- \rightarrow SF_5 + F^- \tag{1.2}$$

Highly mobile electrons are in both cases replaced by heavy and relatively immobile negative ions so that the formation of electron avalanches is prevented, thus inhibiting breakdown. Therefore, the breakdown strength of SF_6 is much higher than that of air or nitrogen gas. When dissociated due to spark over at high electric fields, SF_6 molecules recombine rapidly. When the source of spark energy is removed, SF_6 gas recovers its strength quite fast, which makes it uniquely effective in quenching of high energy arcs. Due to its superior insulation properties, SF_6 is used effectively in circuit breakers and switchgear with a gas pressure in the range of 200 to 600 kPa.

Although SF_6 is a non-toxic and non-flammable gas, its decomposition products, like SO_2F_2, SF_4, SOF_2, and S_2F_{10}, are highly toxic and may form

a major threat to public health when they are released into the atmosphere [8, 10]. Arcs are formed in SF_6 filled circuit-breakers during operation, so that containment of the decomposition products is essential. To contain and purify the decomposed gas is a cost-increasing factor.

A fault survey was conducted [11] to study fault types, locations, extent of damage, and performance histories of gas insulated equipment. Figure 1.3 shows where most of the faults have occurred in a GIS. Spacers are identified as the most likely places for faults to occur. Surface flashover along a gas/solid interface is an important limiting factor for the withstand voltage of GIS and GITL. The electric field perturbations at or near the interfaces may arise for a variety of reasons such as triple junctions, contaminating particles, surface charges, and irregular dielectric surfaces. A local field enhancement causes local ionization and when sufficient, triggers flashover.

The triple junctions, which are the gas-spacer-electrode junctions, have been identified as trouble regions [12]. It was found that discharges occurring at the junction can lower the overall flashover voltages by a factor of two to three when compared to the case with no gap [13, 14]. One study [15] determined that the triple junction reduces flashover voltages for SF_6 when the local field values are in excess of 50 kV/cm for pressure from 100 to 300 kPa. For the studies reported later [16], the triple-junction effects were isolated by reducing the field in the contact vicinity to less than 10 kV/cm. In the research conducted in this

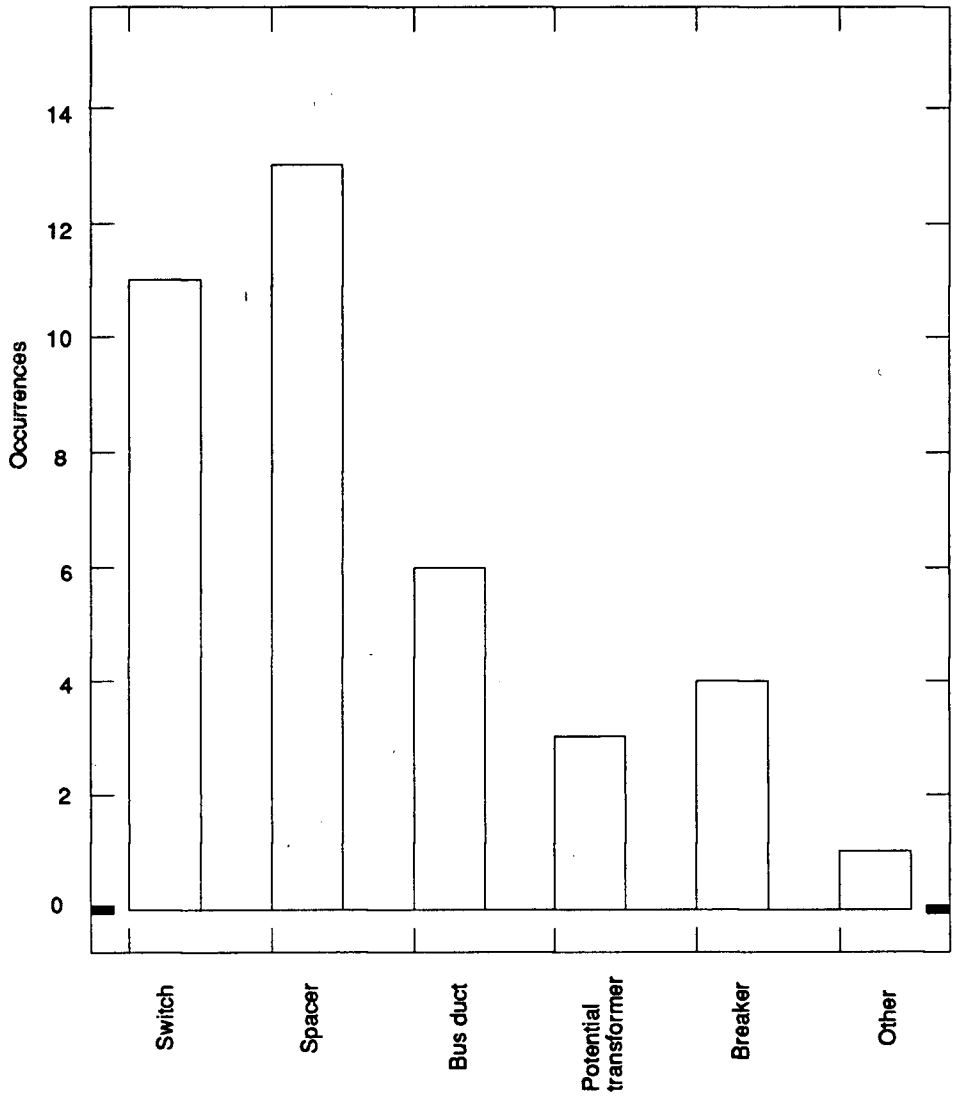

Figure 1.3 Fault locations in north American stations [11].

thesis, the triple junction between the spacer and the plane electrode is shielded by recessing it in the plane electrode.

Conducting particles are one of the major causes for low flashover voltages [17–20]. For AC conditions in a horizontally mounted coaxial GITL, the particles tend to hover near the ground electrode, and the 'bounce height' of the particle increases with voltage. Under DC conditions [21, 22] the particles can cross the gap as soon as the electrostatic force overcomes gravity. They can hover near the inner high voltage conductor and form 'fireflies'. Under lightning and switching impulses, the particles do not have time to move until after the impulse is over, so the large particles are not as harmful as under AC and DC conditions, unless they have already moved onto an insulator. In practical systems, electrostatic particle traps are used to create zero, or very low, fields where the particles are deactivated [23].

Takuma et al [13] studied irregular dielectric surfaces and demonstrated that partial discharges developed in intentionally introduced surface cavities is consistent with the local field enhancement for different types of materials.

Surface charging depends on insulating spacer geometries [24]. There is a lack of agreement on the critical parameters for 'optimized' insulator shapes. Presently there are two basic types of insulators: the insulators which are cast directly on a conductor and the insulators which are made separately. The advantages of

cast insulators are low cost. The second type insulator is where the insulator is premolded, and later fitted on to the conductor. It is preferable to use a low dielectric constant material for the second type of insulators in order to minimize the stress enhancement underneath the insulator at the conductor interface.

It was reported that the accumulation of electrostatic charges on the surface of the insulators is one of the reasons for the reduction in the breakdown strength of high-voltage systems with supporting insulators [25, 26]. Surface flashover voltage of a spacer is a function of the degree of contact between spacer and electrode, the dielectric constant of spacer material, the shape of spacer, the electrode geometry and the type and pressure of the surrounding gas insulation.

Surface charging of spacers under DC, 60 Hz AC and impulse voltages has been studied by several investigators [27–37]. It is believed that surface conduction along the spacer, volume conduction through the spacer material, gaseous ionization and charge generation due to triple-junction and other localized high electric field regions are possible causes for charge accumulation. Local inhomogeneities in the bulk spacer material may also contribute to localized charge accumulation under DC voltage [27]. The charge magnitudes observed [38] do not cause dramatic reduction on the flashover voltage. However, there is experimental evidence to suggest that, under impulse voltages in a non-uniform field geometry, the voltage-time characteristics show a distinct trend to lower time delays to breakdown [34, 35]. Moreover, a reversal of polarity of the applied

impulse voltage results in a significant reduction of the flashover voltage , and may be responsible for anomalous breakdown of spacers [37].

Electrical discharges, surface charging, and flashover in non-uniform fields in SF_6 gas have been the subject of numerous studies over the past decades [39–43]. The object of this thesis is to study the mechanisms and factors governing the magnitude and distribution of surface charges and their influence on flashover voltage in compressed gas insulation.

Chapter 2

Literature Review

Surface charge accumulations on insulating spacer surfaces are recognized as one of the main factors that cause abnormal surface flashover of GIS and GITL systems. Numerous studies have been conducted over the past decades in surface charging and surface flashover. Surface charges have been observed and measured on insulating spacers with different shapes mainly under DC voltages. The resultant electric fields due to surface charges and applied voltage have never been systematically calculated even though several numerical calculation methods have been proposed. Surface flashover in GIS and GITL systems has been one of the major concerns and physical models for the flashover phenomena are still under investigations.

2.1 Surface charge accumulation on insulating spacers

2.1.1 Cylindrical spacer with metal insert under D.C. voltage

The charge accumulation on a cylindrical spacer with metal inserts under D.C. voltage application was studied by several authors [29, 44–46]. The electrode-

spacer geometry was used by Nakanishi et al [45] and the surface charge distribution on the spacer is shown in figure 2.1. This charge accumulation phenomenon was assumed to be determined by the electrical conduction on the surface of a spacer. It is difficult to measure the conductivity of an insulator and its field dependence in the range of high electric fields. However, from the theoretical analysis of surface electrical conductivity, the charge density ρ was obtained as

$$\rho = -\alpha\varepsilon_0 E_Z \frac{\partial |E_Z|}{\partial Z} \tag{2.1}$$

where E_Z is the electric field along the surface and α is a field-dependent coefficient of surface conductivity.

The theoretical charge distribution from equation (2.1) is shown in figure 2.2 (c). Figure 2.2 shows the comparison between the experimental potential distribution and the theoretical counterpart. The distributions are similar except that the residual potential is distributed on a broader area in experiments than the theoretical expectation. This was attributed to the limited space resolution of the electrostatic probe used to measure the surface charges. In this study, the authors found that the deposited charge can be analyzed based on the surface electrical conduction and the theoretical estimations agree reasonably well with the experimental results.

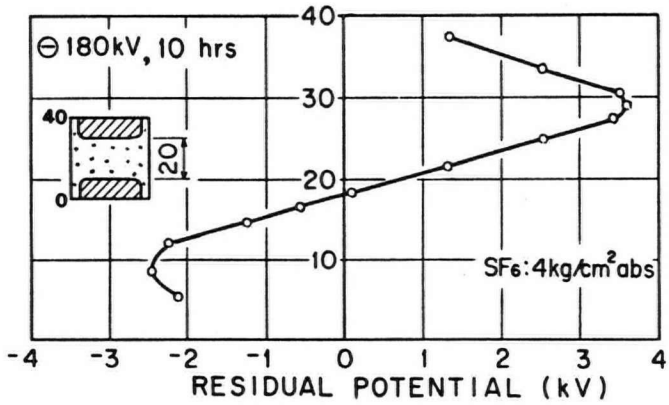

Figure 2.1 Residual potential distribution on untreated silica spacer [45].

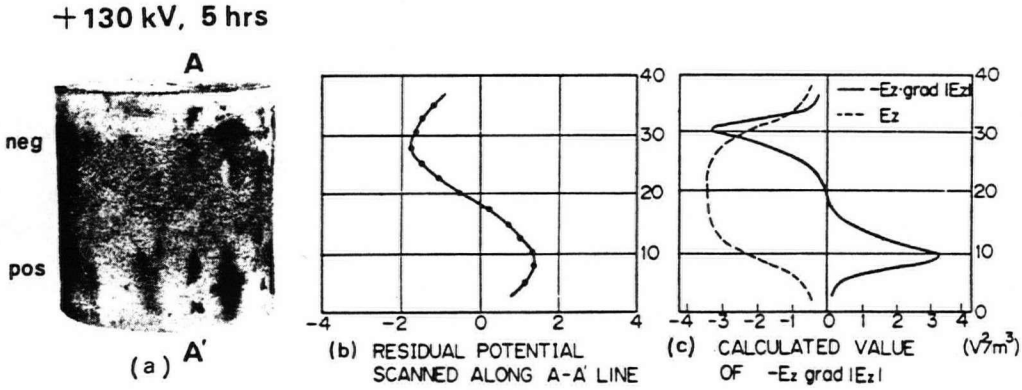

Figure 2.2 Residual potential distribution on untreated spacer and the theoretical calculation on charge accumulation. The gap spacing between metal inserts is 20 mm [45].

Knecht [44] studied the charge distribution for various electrode profiles. Fundamental differences in charge distributions were found, as shown in figure 2.3. The volume or surface conductivity of the epoxy resin used in these experiments is very small. Thus, Knecht concluded that the significant qualitative difference in the global charge distribution measured for the profiles of figure 2.3 cannot be explained in terms of bulk or surface conductivity of the epoxy resin, but can be explained by conduction in the surrounding gas. The gas conductivity is determined by the concentration and mobility of charge carriers. The charges will move in the direction of the prevailing electric field. Thus, the charge accumulation occurs at places where the electric field lines penetrate the epoxy resin surface. The local inhomogeneity in surface charges is thought to be a result of the inhomogeneous ohmic conductivity in the bulk material caused by material impurities.

Fujinami et al [46] did similar experiments for the arrangement shown in figure 2.4, and computed the electrostatic field by the charge simulation method. Figure 2.5 shows the charge distributions on the surface of spacers along Z-direction. Figure 2.6 shows the electric field distributions on the surface of spacers. From figures 2.5 and 2.6, Fujinami et al concluded that the accumulated charge distribution on the spacer surface has a close relationship with the normal component E_n of the electric field. They also found that the accumulated charge distribution is strongly influenced by the surface roughness, as shown in figure 2.7.

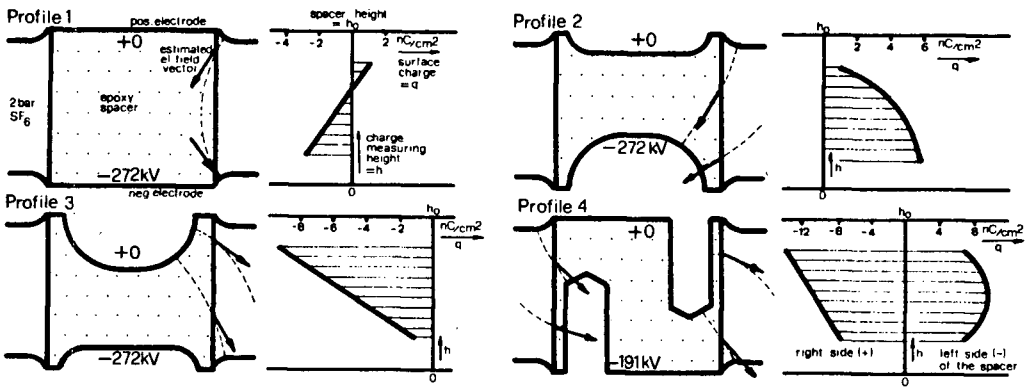

Figure 2.3 Charge distribution along spacer surface for various electrode profiles [44]. Profile 1: pos. charges near pos. electrode, neg. charges near neg. electrode. Profile 2: only pos. charges. Profile 3: only neg. charges. Profile 4: observations of profile similar to 2 and 3 on the same spacer.

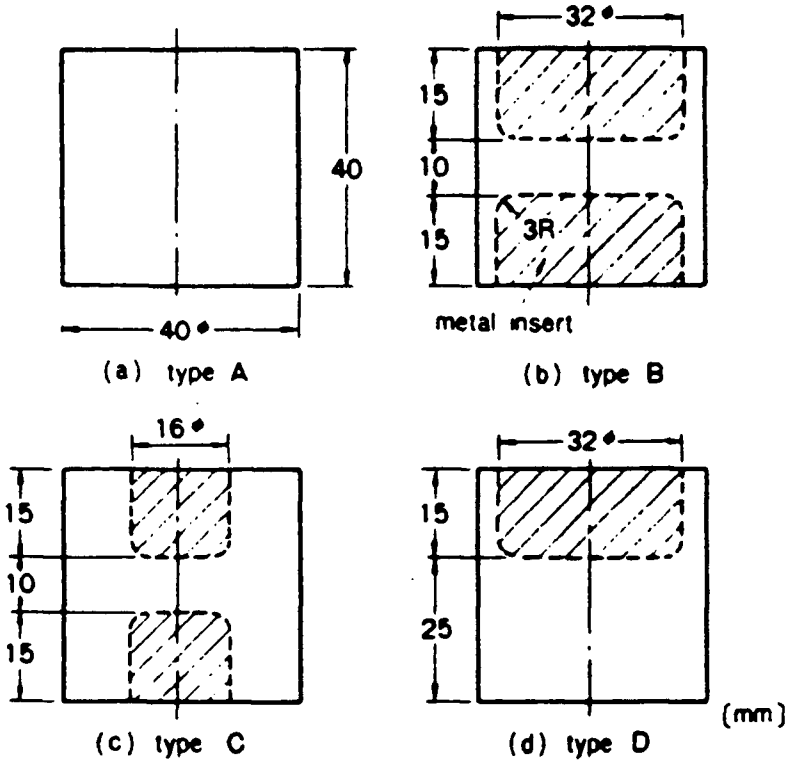

Figure 2.4 Sectional view of model spacers [46].

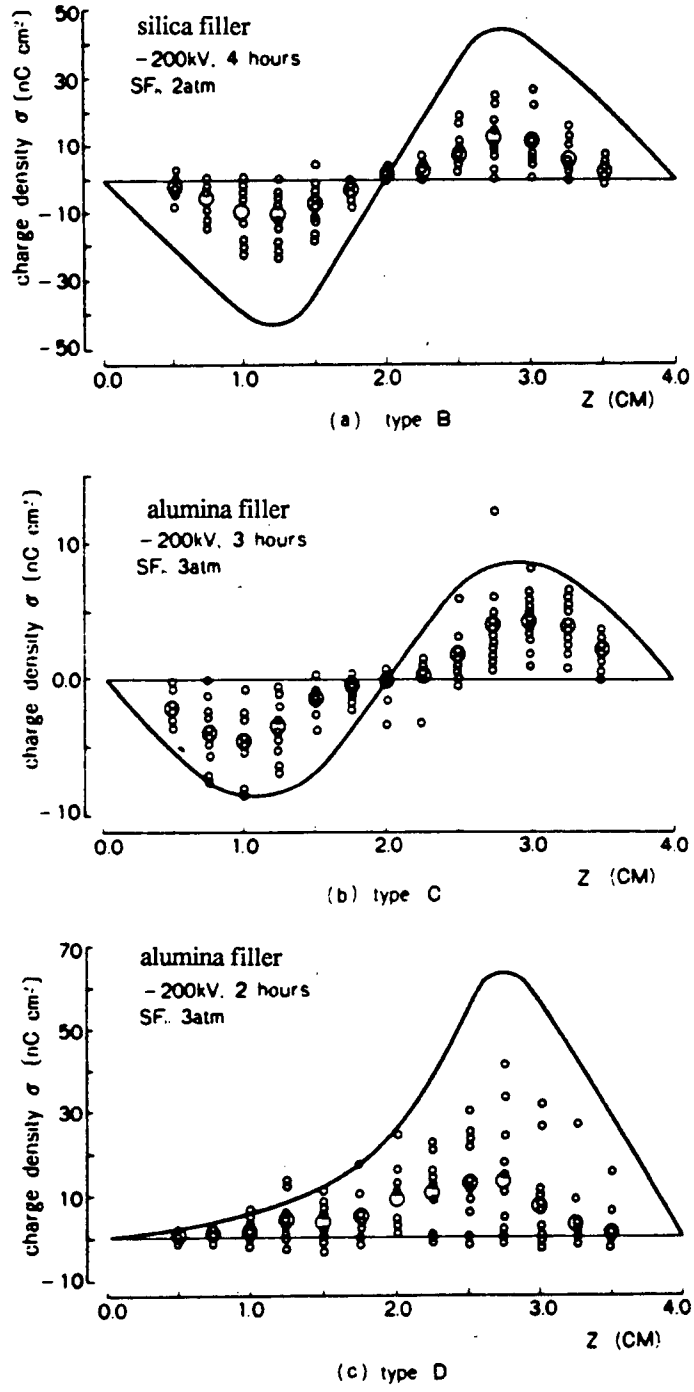

Figure 2.5 Measured charge distributions for the model spacers in figure 2.4 [46]. The solid curves are the normal component E_n of the electric field on the spacer surfaces.

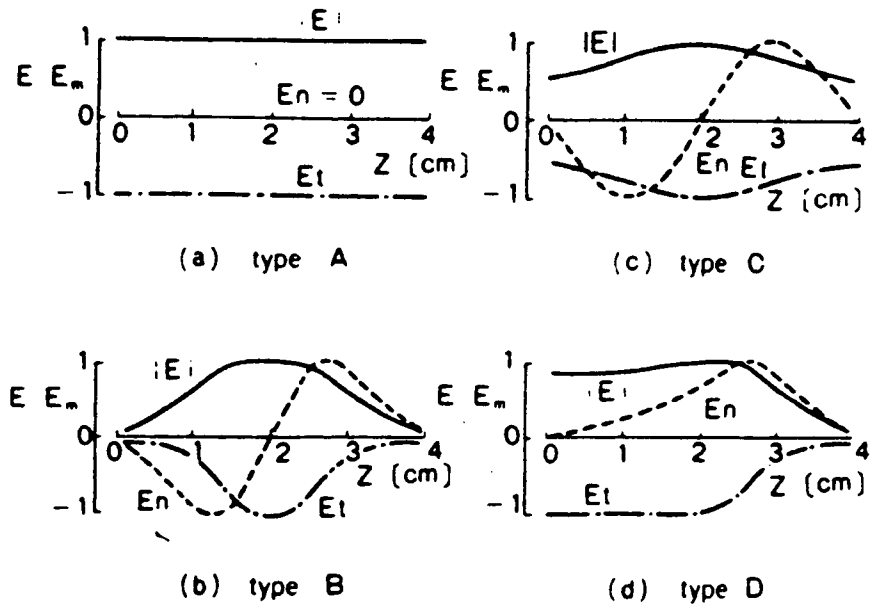

Figure 2.6 Electric field distributions on the surface of the model spacers in figure 2.4 [46].

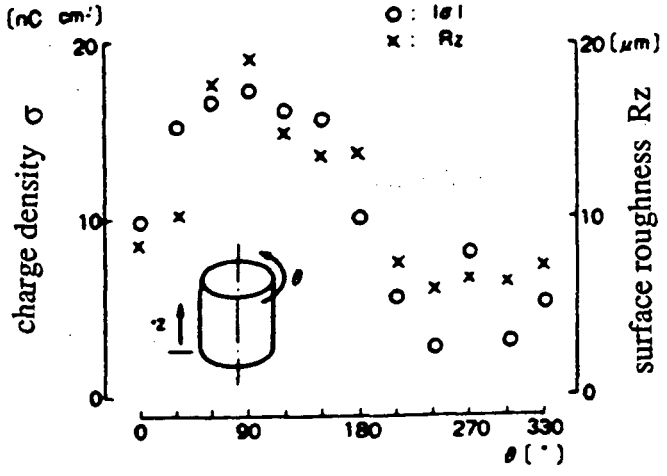

Figure 2.7 Relation between charge density and surface roughness on a spacer surface [46].

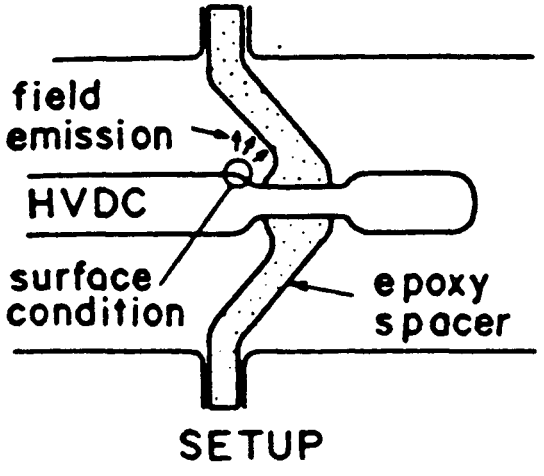

Figure 2.8 Conical spacer set in coaxial cylinder bus [29].

2.1.2 Conical spacer under DC voltage

Nakanishi et al [29] measured the charge accumulation on a model conical spacer in compressed SF_6 gas. The test configuration is shown in figure 2.8. When negative 150 kV DC voltage is applied to the conductor for 5 hours, negative charge was obtained on a concave part of the spacer. However, there was no negative charge after positive DC voltage application. They considered the negative charge to be caused by the field emission at the sharp edges on the electrode when energized with negative DC voltage.

Ootera's study on a 500 kV GIS system gave similar results [47]. The authors suggested that the surface charging due to field emission can be prevented by the use of fine finish on the electrode, particularly at the highly stressed area.

2.1.3 Cylindrical spacer with rod-plane electrode geometry

Recently, quite a few authors have studied charge accumulation on cylindrical spacers with rod-plane electrode geometry [24, 48, 49]. Cherukupalli [24] did several experiments with impulse voltages and found that from the electric field point of view, under uniform field conditions, insulating spacers subjected to impulse voltage in SF_6 at atmospheric pressure do not acquire significant charge, but under non-uniform field conditions, spacers can get charged significantly. Both lightning and switching impulse voltage showed similar behavior.

Tsuruta et al [49] conducted experiments with both DC and lightning impulse voltages. They found that for lightning impulse application at a voltage below corona onset, no charge accumulates on the spacer. But for DC voltage application, at voltages below corona onset, there is low level charging on the spacer with the same polarity as the applied voltage, as shown in figure 2.9 and figure 2.10. The main mechanism for the observed charge pattern under DC voltage, at voltage below corona onset, is drifting charge in the gas. But this mechanism is not effective for lightning impulse because the actual charge accumulation by this mechanism requires a longer duration of voltage application.

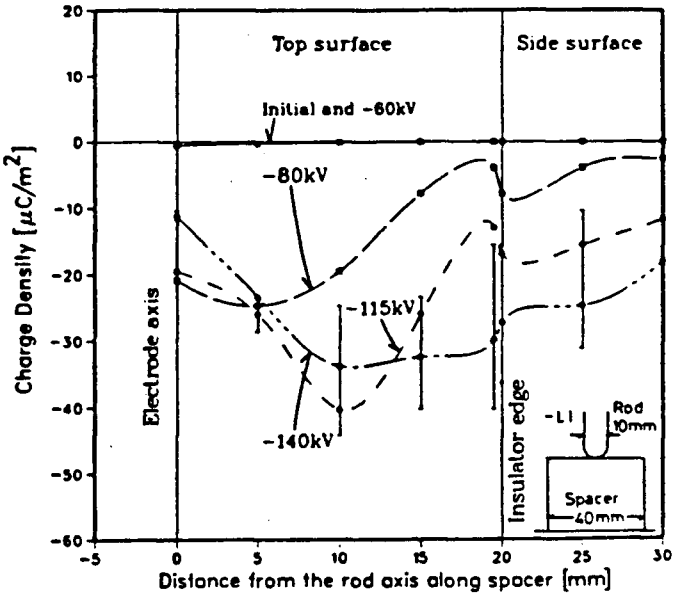

Figure 2.9 Surface charge distribution for negative lightning application (nylon 30 mm height, rod diameter 10 mm) [49].

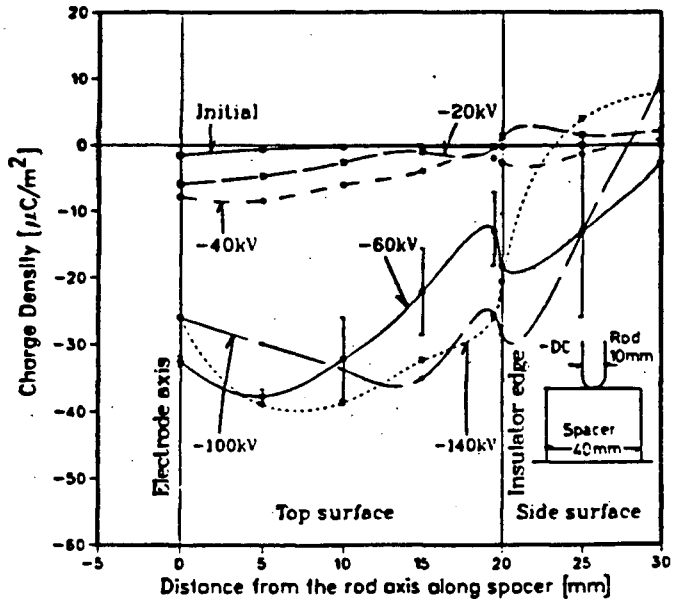

Figure 2.10 Surface charge distribution for negative DC application (PTFE 30 mm height, rod diameter 10 mm) [49].

The mechanisms suggested by many researchers to explain charge accumulation on spacers in insulating gas are:

- Surface conductivity along spacer.
- Bulk conductivity in spacer.
- Gas conduction.
- Field emission or micro-discharges from electrode surface.
- Corona discharge in gas.
- Transport of charged dust particles present in the gas.

There is no general agreement on the mechanisms to explain charge accumulation. The reason is that charge accumulation is a very complex phenomenon and cannot be explained clearly by only one mechanism. In order to have a better understanding about surface charge accumulation, a series of experiments are conducted in this research under different experimental conditions. The details are given in Chapter 6.

2.2 Surface charge field computation

2.2.1 Numerical methods for electric field calculations

Numerical techniques of analysis are based on approximate solutions of a set of equations describing a physical problem. They can be classified into three major methods: finite difference method (FDM), finite element method (FEM) and boundary element method (BEM).

The finite difference method (FDM) was the first widely known approximate method. It uses local expansions for the variables, with truncated Taylor series. It is approximate in the sense that derivatives (i.e.$\frac{\partial \phi}{\partial x}$) are replaced by difference quotients (i.e. $\frac{\delta \phi}{\delta x}$) over a small interval. The smaller the interval, the higher the accuracy of the solution. The regular grids are the only ones used in practice now. In fact, a regular grid is not suitable for the field with very non-uniform distribution and also not suitable for curved boundaries or interfaces.

The finite element method (FEM) divides a field region into subregions so that the unknown quantities are represented by suitable interpolation functions which contain the values of the potential at the respective nodes of each element. The main feature of the finite element method is the use of irregular grids. Flexibility is its greatest advantage with respect to the traditional finite difference method. Elements with various shapes can be easily adapted to any shape of boundary and interface geometries. Like FDM, FEM has more variables because it considers the whole domain surrounded by boundaries. However, the final equations form a symmetric banded matrix with dominant diagonals. CPU time and machine memory can be saved by using these features. For open boundary problems, the infinite regions have to be truncated for most cases.

The boundary element method (BEM) is now firmly established as an important alternative numerical technique to the above two methods. BEM transforms the differential equations inside and on the boundary of the domain into integral equations relating only boundary values by introducing image charges, and then finds out the numerical solution of those equations. Values at internal points can be calculated afterwards from the boundary data. Since all numerical approximations take place only at the boundaries, BEM has fewer variables compared with FDM and FEM. The final equation has a full matrix, but it can be symmetric. These advantages reduce CPU time and the computer memory requirements. It is easy for BEM to handle open boundary problems and boundaries with surface charges.

In electrical engineering applications, two derivations of BEM are charge simulation method (CSM) and surface charge simulation method (SSM). The image charges in CSM are located inside a domain and choosing and locating image charges are strongly dependent on an individual's experiences. Line charges and ring charges are the most common image charge functions used in CSM. Image charges in SSM are located right on the boundaries. It is much easier for SSM to deal with asymmetry in field and with charges on the boundary surfaces than CSM. As discussed in Chapter 5, several image charge functions used in SSM are compared and a simplified charge function is chosen for the field calculation in this investigation.

2.3 Spacer flashover in gas insulated systems

2.3.1 Spacer flashover behavior

With the development of gas-insulated transmission lines (GITL) and substation equipment (GIS) , there has been a tremendous increase in the interest in high-voltage gas breakdown and surface flashover of insulators in GIS or GITL. Considerable work has been done to establish the factors affecting the flashover voltage of gas insulated systems.

In a practical GIS system, there may be free conducting particles, fixed conducting particles, non conducting particles, water vapor, or decomposition

by-products of the insulting gas. Systems with spacers are more sensitive to contamination [50].

In a horizontally mounted GIS/GITL system, the free conducting particles, once they become charged under the influence of the applied voltage, oscillate between the electrodes and may impact on the conductor and the spacer surface, thus reducing the dielectric strength of the system. Figure 2.11 shows the effect of free copper wires on the breakdown voltage of the system with coaxial geometry [51]. Figure 2.12 shows the effects of fine copper powder on the breakdown voltage of the system shown in the same figure [52]. For fixed conducting particles, their effect on flashover voltage depends on their locations on conductors or insulators. On some locations, their effects can be ignored, but on other locations, their effects can be significant as shown in figure 2.13.

The effect of non-conducting particles is much less severe compared to that of conducting particles. Under DC, AC, or impulse voltage application, no movement of these particles was observed. Experiments with epoxy spacers show that no reduction in the flashover voltage was observed in the presence of non-conducting particles [50].

Figure 2.14 shows the effect of the surface temperature on the AC flashover voltage of cylindrical spacers in a gas having various moisture contents [52]. The almost constant value of the flashover voltage in the dry condition when the

temperature is lower than 0^oC means that the water frosted on the spacer surface does not impair the flashover performance. When the temperature rises above 20^oC, the flashover voltage increases towards the dry condition level because of the evaporation of the condensed water.

Particle contamination can be avoided by using electrostatic particle traps in practical systems. Particle traps can create zero or very low fields where the particles are deactivated.

2.3.2 Effects of spacer and surface charge on flashover

The reduction of breakdown voltage can either be caused by contamination as discussed above, or improper design of the insulating arrangement or an interaction between gas and insulator during predischarge development. The contamination can be minimized by proper design. The insulating arrangement seems more important in GIS. Pfeiffer et al [51] found that the flashover voltage, both in N_2 and SF_6, is reduced in the presence of an insulator by about 10 - 15 %. Figures 2.15 and 2.16 [37] show the breakdown voltage and the time to breakdown with and without spacer. The breakdown voltage with spacers is lower than that without spacers and the time to breakdown with spacers is shorter than that without spacers. In gas-insulated systems, discharges before the flashover occurs produce free charge carriers. These charges may deposit on insulator surfaces and change the surface field so that the ambient field may be distorted. This phenomena may result in an increase or decrease in the flashover voltage. The flashover voltage

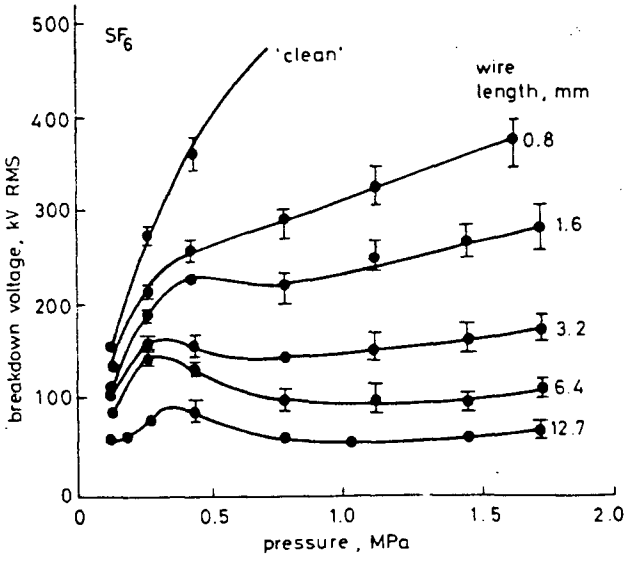

Figure 2.11 Breakdown initiated by free copper wires, 0.4 mm diameter, in 150 mm /250 mm diameter coaxial geometry [50].

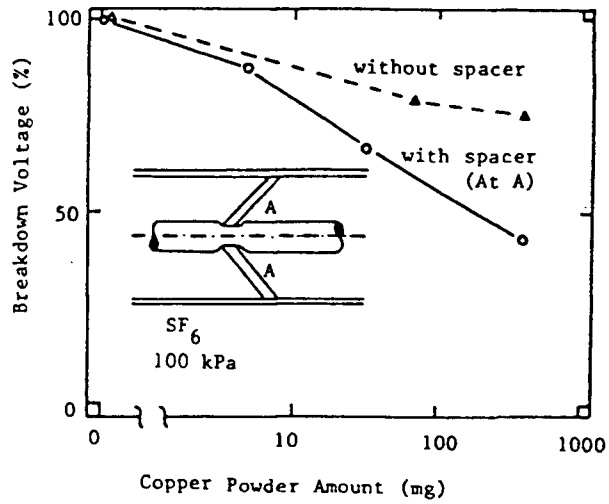

Figure 2.12 Effect of amount of fine copper powder (≤ 30 μm diameter) on the alternating breakdown voltages of a coaxial system with a cone-type spacer [52].

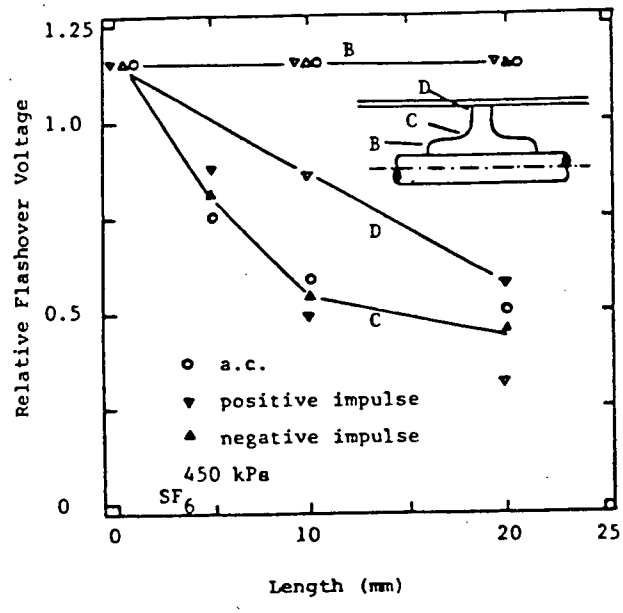

Figure 2.13 Influence of the length of a copper wire on the flashover voltage of a disc-type spacer [52].

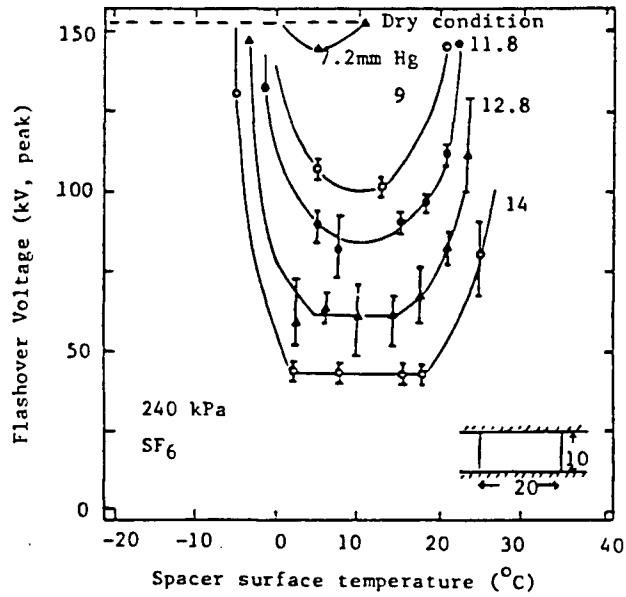

Figure 2.14 Flashover voltage as a function of spacer surface temperature with various water contents in SF_6 [52].

of a highly charged spacer decreases considerably at the time of polarity reversal [53] as shown in figure 2.17.

Yu et al [30] conducted an experiment to measure impulse flashover voltage after a disc-type spacer has been exposed to a negative DC voltage for several hours. The experimental results are shown in figure 2.18. The charges caused by the negative DC voltage do have some effects on the impulse flashover voltages. The negative impulse flashover voltage slightly increases and reaches a saturation value after a negative DC voltage pre-charging for about 5 hours. However, the positive impulse flashover voltage decreases due to negative DC pre-charging. Abdul-Hussain and Cornick [32] reached a similar conclusion that for the rod-plane system and applications of same polarity impulses, the effect of surface charges was always towards increasing the flashover voltage; the surface field due to charges acts in opposition to the applied voltage field. But under other conditions, such as oscillatory impulse waves or impulse voltage polarity reversal, this would not be the case, and the surface field would aid the applied voltage field, leading to a reduction of flashover voltage.

More recently, flashover experiments at KEMA [54] were carried out on cylindrical insulators with a diameter of 40 mm and a height of 20 mm between Rogowski-shaped electrodes. The flashover voltage was determined with DC, AC and impulse voltages. The surface charges with a peak value of 50 $\mu C/m^2$ were produced by a corona needle before voltage applications. The corona voltage was

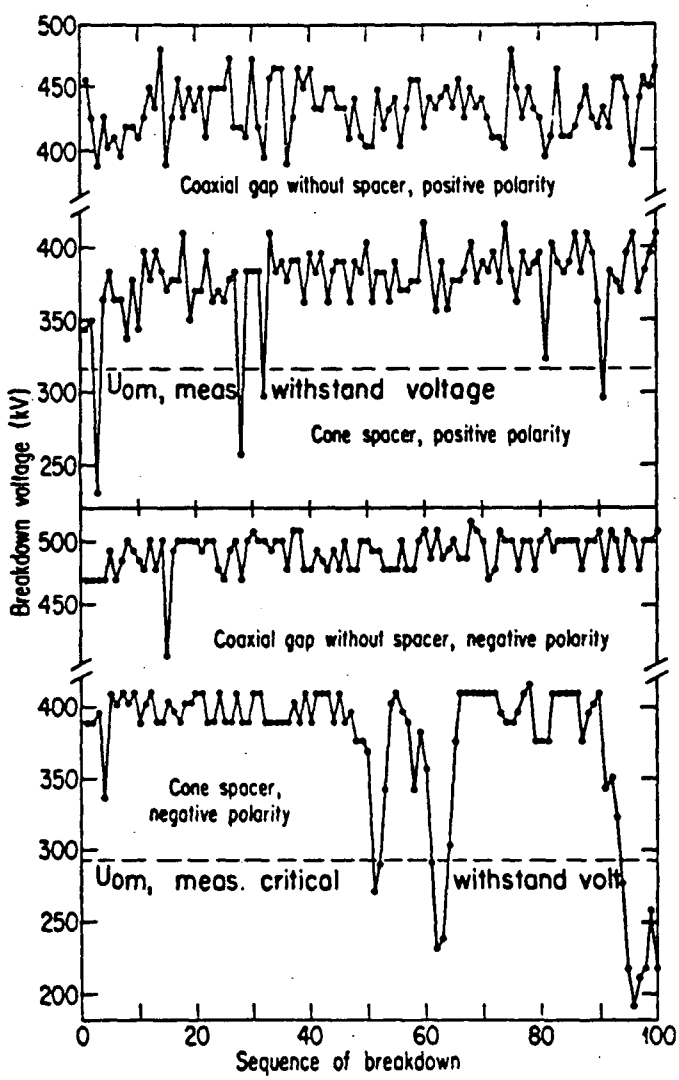

Figure 2.15 Typical sequential variations of the breakdown voltage of a coaxial conductor without and with a composite-profile cone spacer [37].

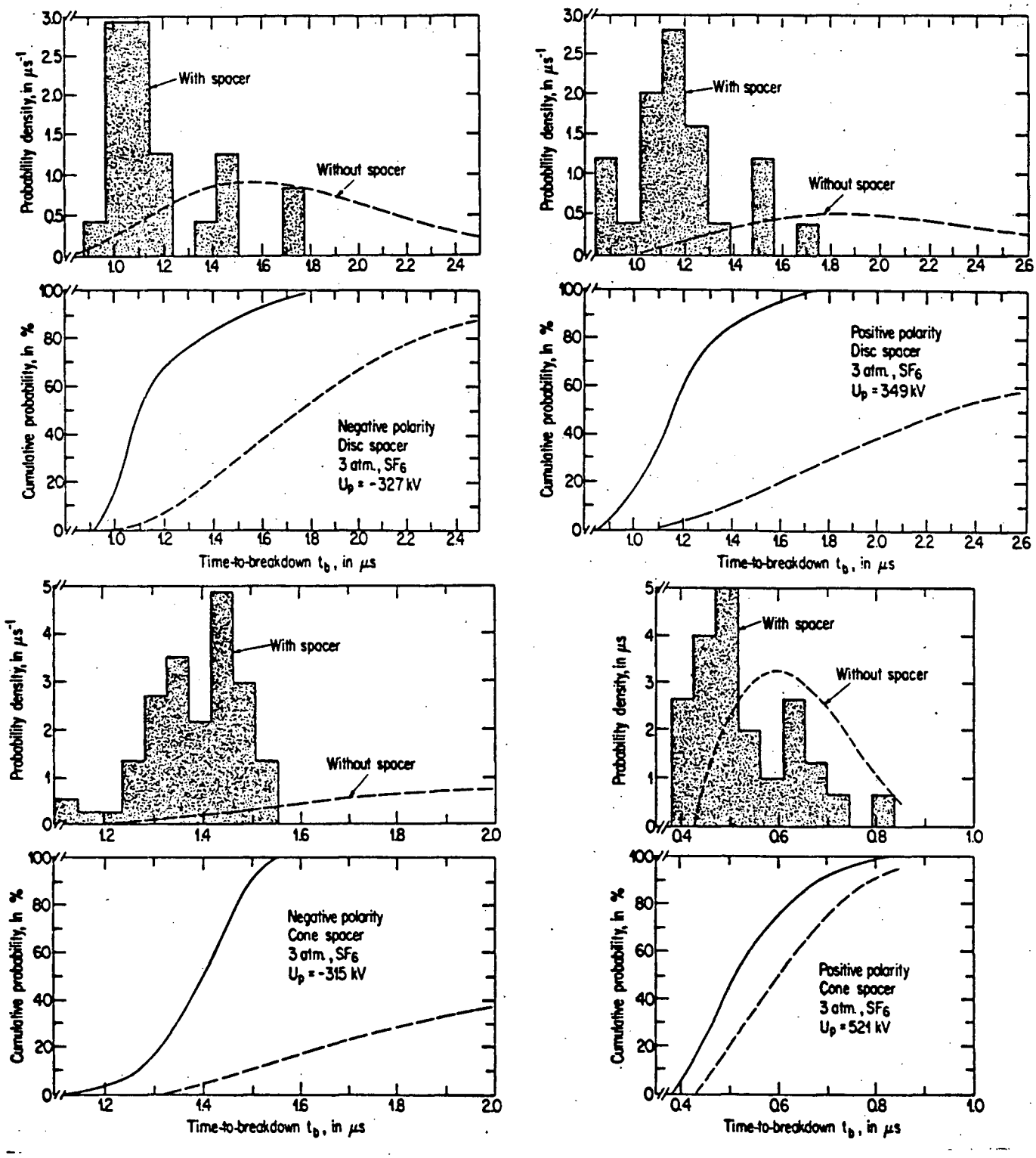

Figure 2.16 Typical distributions of the time-to-breakdown in presence of a spacer in SF_6 [37].

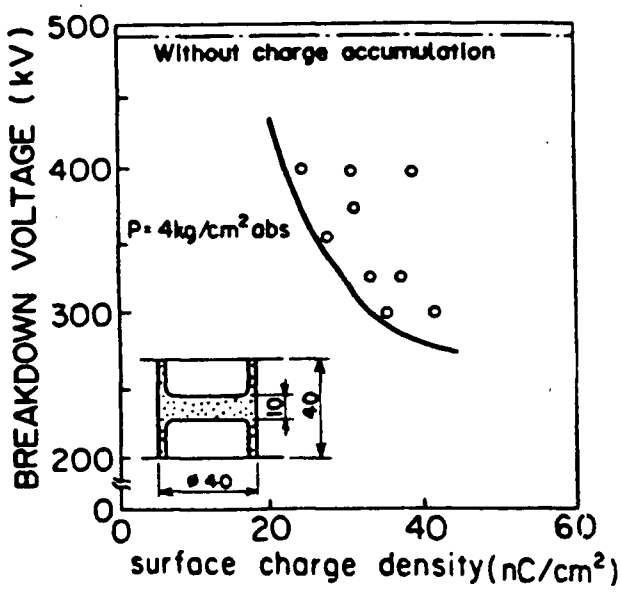

Figure 2.17 Effect of accumulated charge on flashover voltage in polarity reversal test [32].

supplied by an adjustable 30 kV high-voltage DC unit of either polarity. The effect of surface charge on AC flashover along cylindrical insulators is illustrated in figure 2.19. From figure 2.19, we see that both negative and positive charges on spacer result in reduction of the breakdown voltage of the systems. Figure 2.20 shows the effect of surface charge on lightning impulse flashover along cylindrical insulator.

Breakdowns taking place in a GIS are often associated with the insulators that support the high-voltage conductors. The surface flashover process may be modeled as a two-step event: initiation, followed by propagation across the entire gap [55]. The initiation results from a local field perturbation of sufficient

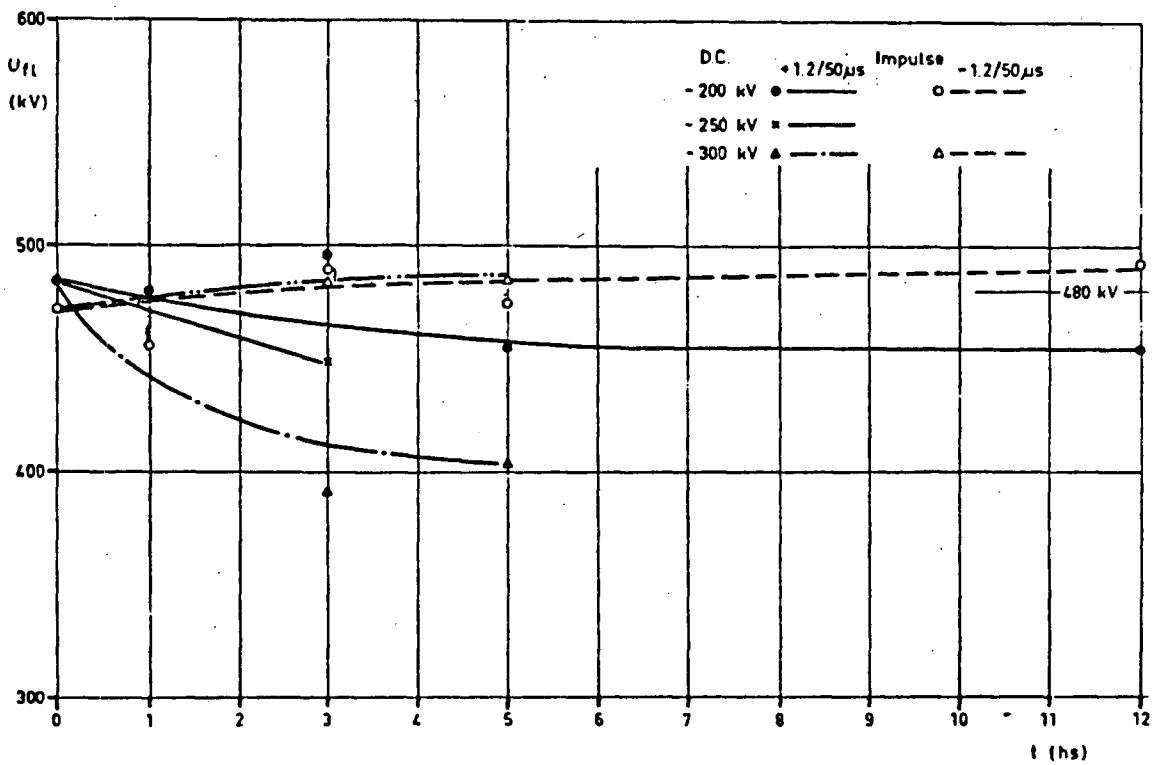

Figure 2.18 The impulse flashover voltage of clean smooth spacers exposed to a negative DC voltage as a function of the exposure time and the DC voltage amplitude [30].

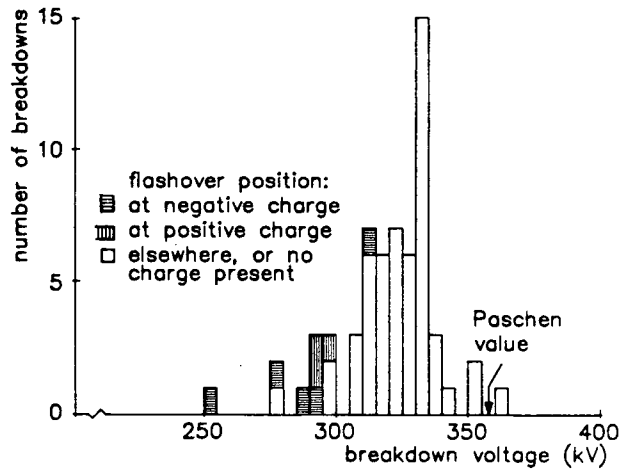

Figure 2.19 The number of flashovers as a function of AC flashover voltage (20 mm) for PTFE insulator [54].

magnitude to start ionization. Within the ionization zone, only when a level of 10^8 electrons in an avalanche is reached, which is the discharge inception criterion [56, 57], flashover can be expected. The propagation, however, is very much dependent on the electric field along the propagation path. It is generally assumed that the field necessary for propagation is much lower than for ionization initiation. Contaminating particles and surface charge accumulations are found to be influential when they significantly perturb the surface fields. The detailed propagation models are presently not well developed.

Surface charge accumulation and surface flashover have extensively been stud-

ied since 1985 at University of British Columbia. This thesis is the continuation of the previous work, which will be reviewed in Chapter 3 in some detail.

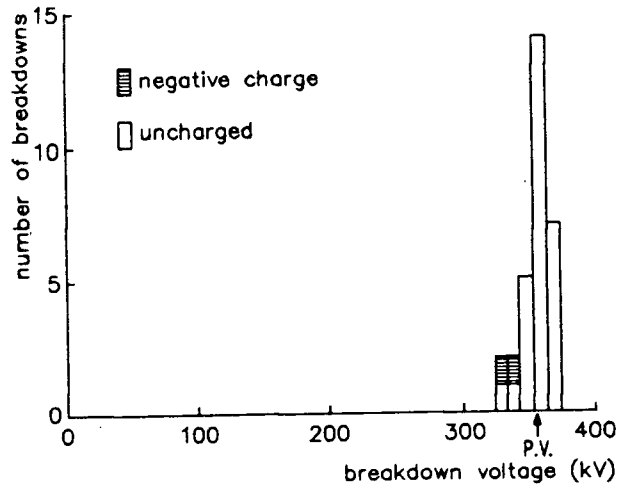

Figure 2.20 The number of breakdowns as a function of the crest voltage of the lightning impulses [54].

Chapter 3

Statement of Problem

3.1 Previous Work at UBC

3.1.1 Introduction

The study of surface charge accumulation on spacer surface and surface flashover is a long term continuing investigation. Considerable work has been done in the high voltage laboratory of the Electrical Engineering Department, the University of British Columbia. Previous work includes [24]:

- Pre-breakdown phenomenon.
- Surface charge accumulation with different voltage levels (switching and lightning impulses), different insulating spacer surface finish, and different electric field distribution (uniform and non-uniform).
- Effect of AC pre-charging on impulse flashover.

Since the investigation reported in this thesis is a continuation of the previous work, it is useful to review the earlier finding in some detail. This will establish the context of the present investigation.

3.1.2 Pre-breakdown phenomenon

By measuring pre-breakdown current on an oscilloscope, corona pulses can be observed. The corona pulse current with applied voltage is shown in figure 3.1.

The corona inception time may be taken as the time interval from the virtual zero of the applied impulse wave to the appearance of the first corona pulse on the current wave. The mean value of the corona inception time at voltage levels from the inception level up to those close to breakdown is shown in figure 3.2. It can be seen that both the spacer material and the spacer surface finish have considerable influence on the mean corona inception time, which is in agreement with the observations reported earlier [31].

The most suitable distribution fitting the experimental values of corona inception time t is the log-normal distribution given by

$$p(t) = \frac{1.0}{\sigma 2\sqrt{\pi}} \cdot \exp\left(\frac{-(\ln t - \ln \bar{t})^2}{2\sigma^2}\right) \quad 0 \ll \ln t \ll \infty \tag{3.1}$$

where $\bar{t}$ is the mean value of time t and σ is the log standard deviation. Figure 3.3 shows the computed distribution, using measured corona inception data, for a system (with a rod electrode diameter of 5 mm) with and without an epoxy spacer. It is apparent that with increasing voltage, the average value of the time delay and standard deviation decrease. The presence of the insulating spacer causes a considerable decrease in the time delay.

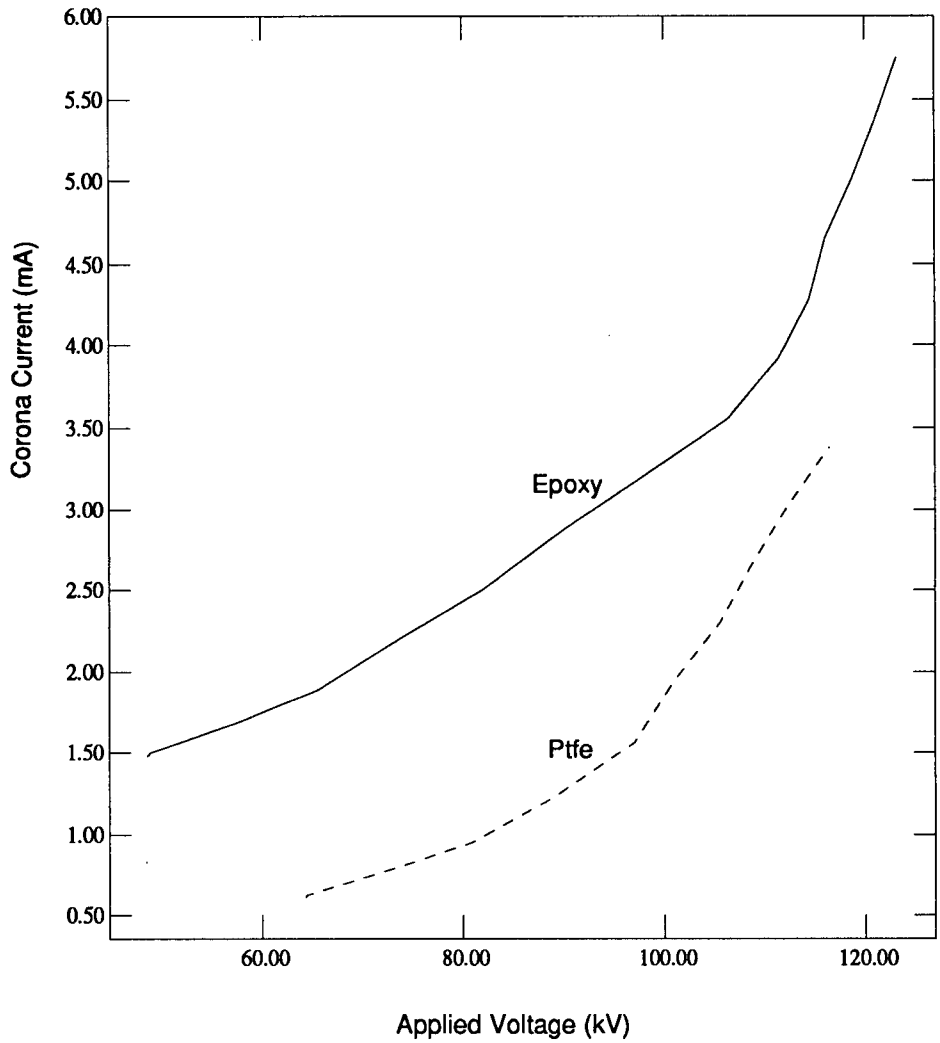

Figure 3.1 The mean corona pulse current with switching impulse applied voltage for epoxy and PTFE spacers at 0.1 MPa for 5 mm diameter rod electrode [24].

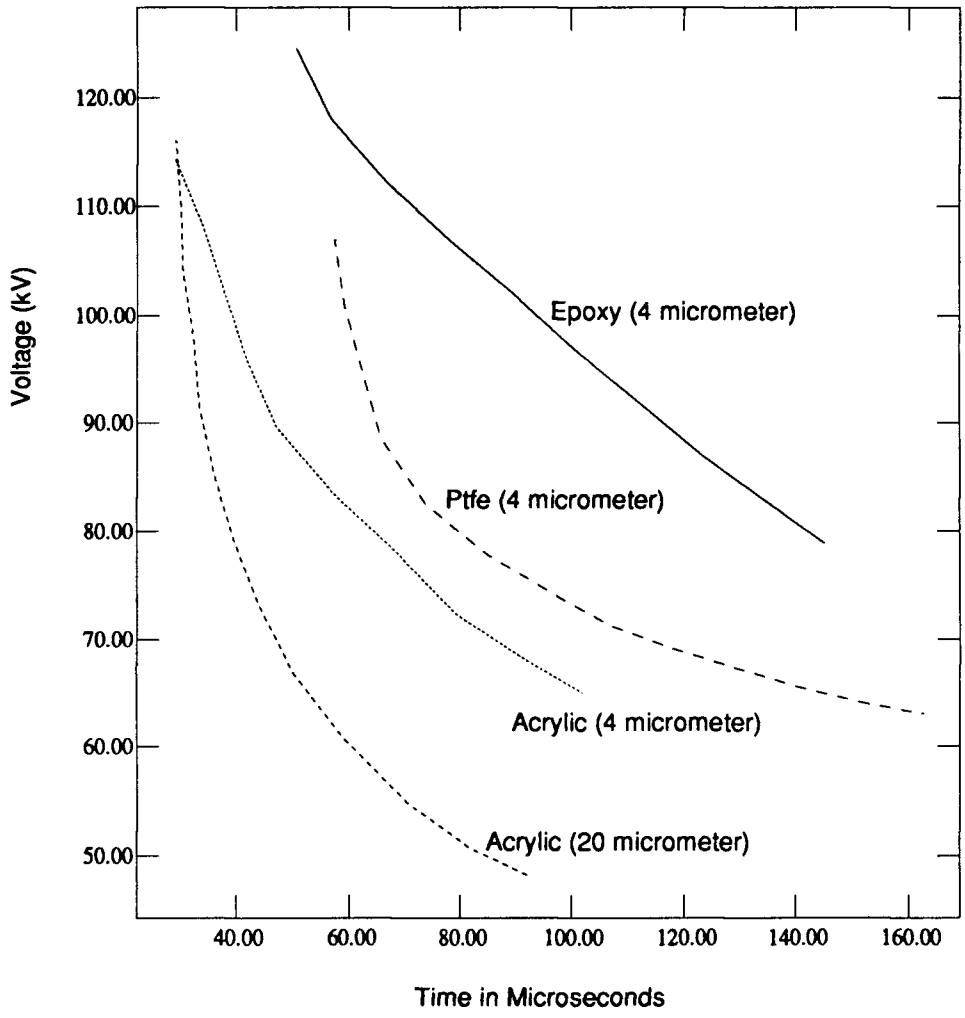

Figure 3.2 Variation of the mean corona inception time with applied voltage for different material and surface finish which is indicated in bracket [24].

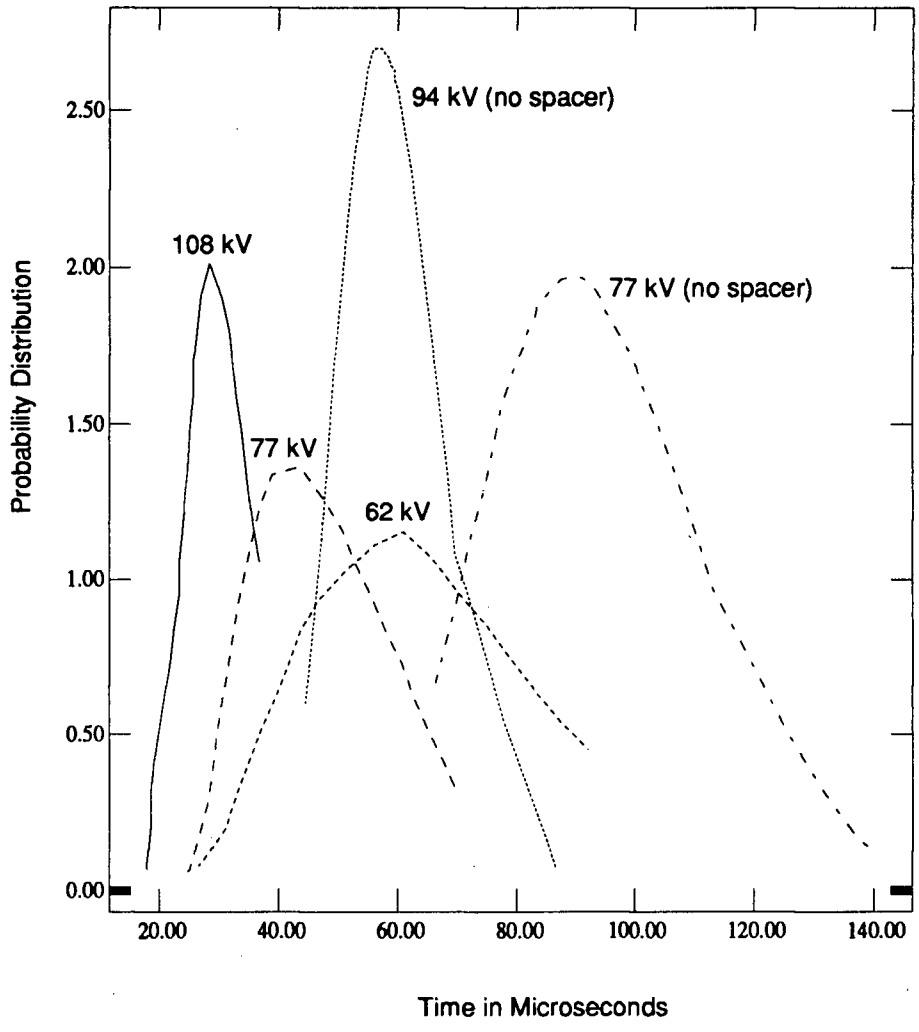

Figure 3.3 Computed log-normal distributions of the corona pulses with and without epoxy spacer at different voltages with 5 mm diameter rod electrode [24].

The plot of $-\log(1-p(t))$ versus time to appearance of the first corona, where $p(t)$ represents the probability of a corona discharge occurring before time t, is called a Von-Laue plot. Figure 3.4 shows the Von-Laue plots for epoxy spacer at +77 kV with 5 mm and 10 mm rod electrode diameter. A larger slope in this figure is indicative of a higher electron production rate. As expected, the rate of electron production is very much field dependant. The higher fields associated with the 5 mm imply a higher photon efficiency providing for a larger number of charge carriers from the spacer resulting in a higher slope of the Von-Laue plot.

The above results suggest the following for the pre-breakdown behavior of a rod-plane spacer system:

- The presence of a spacer significantly reduces the corona inception time of a spacer gap.
- Both the material and its surface roughness have some influence on the pre-breakdown behavior.
- The rate of electron production is very much field-dependent.
- Due to the presence of the spacer in the high field region, photon emissivity from the spacer surface has been suggested to be a possible mechanism for the charge generation contribution to the streamer growth.

3.1.3 Surface charge accumulation

The nature of surface charging on an insulating spacer depends on many

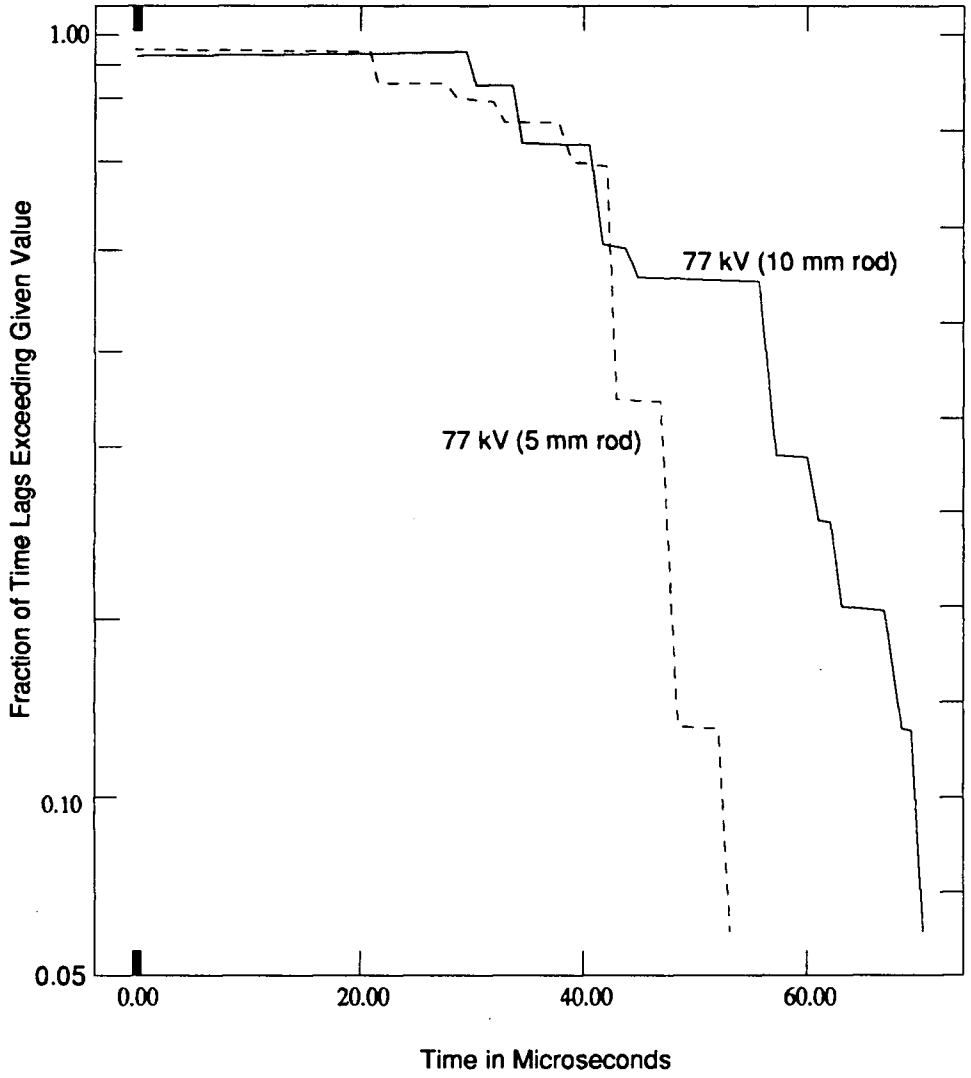

Figure 3.4 Von-Laue plots for epoxy spacer at 77 kV (rod electrode diameter is 5 mm and 10 mm) [24].

parameters. In order to examine the effect of some parameters on surface charging, the following work has been done in the high voltage laboratory at UBC [24].

- Surface charging versus ambient electric field distribution, i.e. uniform field of a plane-parallel electrode system and non-uniform field of a rod-plane electrode system.
- Surface charging versus insulating spacer surface finish.
- Surface charging versus the type of applied voltage, i.e. switching impulse and lightning impulse.

The experiments were done by applying impulse voltage starting from +45 kV up to 190 kV on the same insulating spacer with both plane-parallel electrodes and rod-plane electrodes. The results show that under uniform field conditions, insulating spacers, subjected to impulse voltages in SF_6 at atmospheric pressure, do not acquire significant surface charges. However, defects present on a spacer or the electrode surface can cause charge deposition which may be attributed to the field distortion created by the imperfection. The magnitude and the distribution of the surface charges depend on the severity and location of the imperfection. Under non-uniform field conditions, significant charge deposition on the insulating spacer was obtained. Therefore, the conclusion is that surface charging is very much depend on the ambient electric field distribution.

The experiments were done for 4 μm and 20 μm surface finish acrylic

insulating spacers. The results show that no significant differences were observed in charge magnitudes for the different surface roughness of the selected acrylic spacer, although surface roughness has some influence on the pre-breakdown behavior.

In order to examine the effect of the rate of rise of the impulse voltage on surface charging, both switching and lightning impulse voltages were used. The results show similar charging behavior for both switching and lightning impulse voltages.

3.1.4 AC pre-charging

Under normal conditions, a GIS system is stressed with a rated AC voltage of a system. A switching or a lightning transient can appear on the system under abnormal conditions. In order to study how a GIS system would behave under a composite stress, AC pre-charging experiments were conducted on cylindrical spacers (40 mm in diameter and 30 mm in length) between rod-plane electrodes [24]. In the experiments, an AC voltage at a desired level was applied to an insulating spacer, with negligible initial residual charge, for a certain period of time. Then, the AC voltage was removed and an impulse voltage close to breakdown level was applied to the same spacer. The flashover voltage and flashover time were recorded as shown in figure 3.5 and figure 3.6.

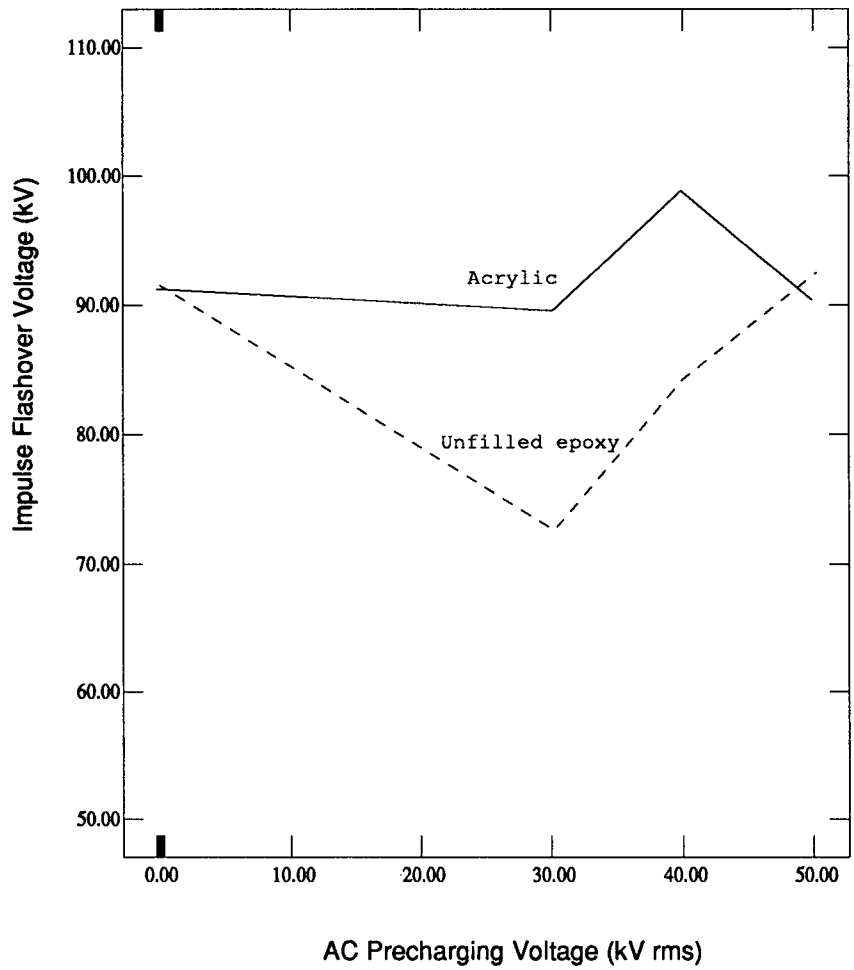

Figure 3.5 Impulse flashover voltage versus AC pre-charging for 30 minutes on cylindrical spacer between rod-plane electrodes (10 mm diameter rod) [24].

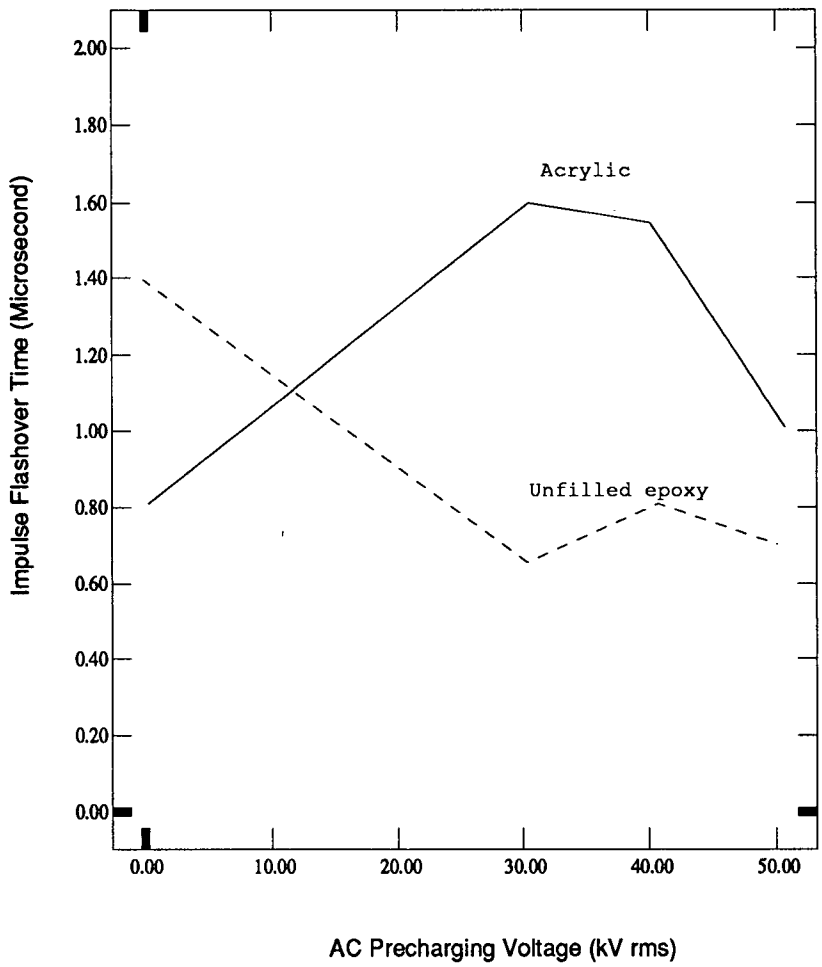

Figure 3.6 Impulse flashover time versus AC pre-charging for 30 minutes on cylindrical spacer between rod-plane electrodes (10 mm diameter rod) [24].

The results of the spacer flashover under sequential application of impulse voltage show a considerable scatter, amounting up to ±30%. The presence of charges on the insulating spacer surface results in a perturbation of the symmetric ambient field distribution. The asymmetric ambient field distribution due to surface charges may account for the scatter in the breakdown voltages. The variation of the flashover voltage and time to flashover fall well within the statistical scatter for positive impulse with AC pre-charging.

3.2 Present investigation

The previous research on pre-breakdown phenomenon is relatively complete. By pre-breakdown current measurement, three kinds of graphs, which are the mean corona inception time versus applied voltage, computed log-normal distributions of corona pulses, and Von-Laue plots, can be used to show how each parameter affects corona pulses. The parameters identified are the presence of insulating spacer, applied voltage level, insulating spacer materials, spacer surface finish, non-uniformity of ambient electric field, and the ambient gas pressure.

The previous research on surface charge accumulation shows that non-uniform ambient electric field distribution is the critical factor that results in surface charge accumulation on the insulating spacer surface under impulse voltage. Spacer surface finish and the types of impulse voltages (i.e. switching and lightning impulse) show no significant effect on surface charge accumulation.

Further questions are addressed in this investigation such as how surface charge accumulation is affected by the other parameters, for example, the surrounding gas pressure, the types of surrounding gases, and spacer materials, how surface charge accumulation is related with corona inception voltage, what happens to the surface charge patterns after impulse voltage pre-charging, and how surface charges actually alter ambient electric field distributions.

As a continuation of the previous work on this long term project, the two major areas investigated in this thesis are the roles of surface charge accumulation and the critical field conditions for spacer flashover. The following aspects were studied in this research:

1. Surface charging and corona. Surface charges were measured at different voltage levels under different gas pressures for different geometries and compared with the calculated corona inception.
2. Surface charge variation with gas pressure.
3. Surface charges with different ambient fields near the rod electrode.
4. Surface charges with different ambient gases.
5. Comparison of surface charging under impulse and DC voltages.
6. Surface charge variation with impulse pre-charging.
7. Surface charge simulation (SSM) computer program development for total electric field computation of a rod-plane electrode system with a charged

cylindrical spacer between the electrodes.

8. The effect of surface charge field on spacer flashover. The necessary combined field from applied voltage and surface charges for surface flashover propagation.

Since in the previous work by Cherukupalli [24] extensive pre-breakdown corona measurements were made, no attempt has been made to duplicate that data. The trends observed in the pre-breakdown corona pulses have been utilized in interpreting the results observed in the present investigation.

Chapter 4

Experimental Setup

4.1 Introduction

A hemispherical capped rod-plane electrode geometry is chosen for the experimental research in this investigation for the following reasons:

- No significant surface charges were observed in uniform fields under impulse voltages [24]. The rod-plane electrode geometry provides an extreme non-uniform field distribution and is used for studying surface charge accumulation at impulse voltages.
- It is easy to vary the degree of the field non-uniformity in rod-plane electrode geometry by varying the rod electrode diameter.
- For rod-plane configurations, a reasonably low applied voltage may produce a high electric field at the point apex.
- Data from the previous work [24] are available for comparison.

4.2 Experimental setup

The basic rod-plane electrodes and cylindrical insulation spacer arrangement is shown in figure 4.1. The high voltage rod electrodes used are hemispherical capped steel rods with 1.6 mm and 3.2 mm diameter. The low voltage plane electrode is made of aluminum with 150 mm diameter and 30 mm thick with round edges. On the center part of the plane electrode there is a recess, approximately 45 mm in diameter and 2 mm in depth which shields the triple junction.

The cylindrical spacers used in this investigation are made of PTFE or nylon, these two materials have significantly different dielectric constants (2.1 for PTFE and 3.8 for nylon). All samples are 40 mm in diameter and 30 mm in length. The surface finish is approximately 4 μm.

The schematic of experimental setup is shown in figure 4.2. There are two capacitive probes. One is for scanning surface charges on the top surface and the other is for scanning surface charges on the side surface of a spacer. The signal from either of the two capacitive probes is sent to an electrometer and then displayed on a Type 3036 X-Y plotter as Y signal. The X signal of the X-Y plotter is from a potentiometer driven by a DC motor, which monitors the probe location.

The motor drive system consists of two DC motors. The one on the right side is used for an up-down motion of the plane electrode and the other on the left side is used for rotation of the plane electrode, around the axis of symmetry.

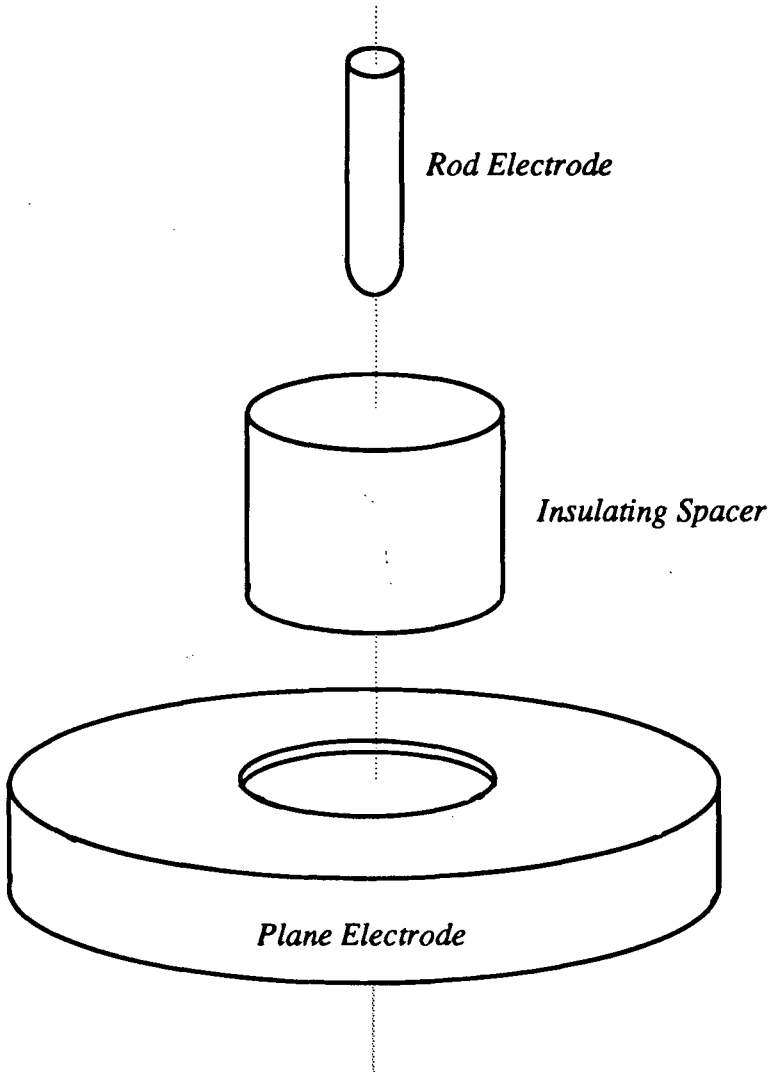

Figure 4.1 Elements of the electrodes-spacer system used in the experiments.

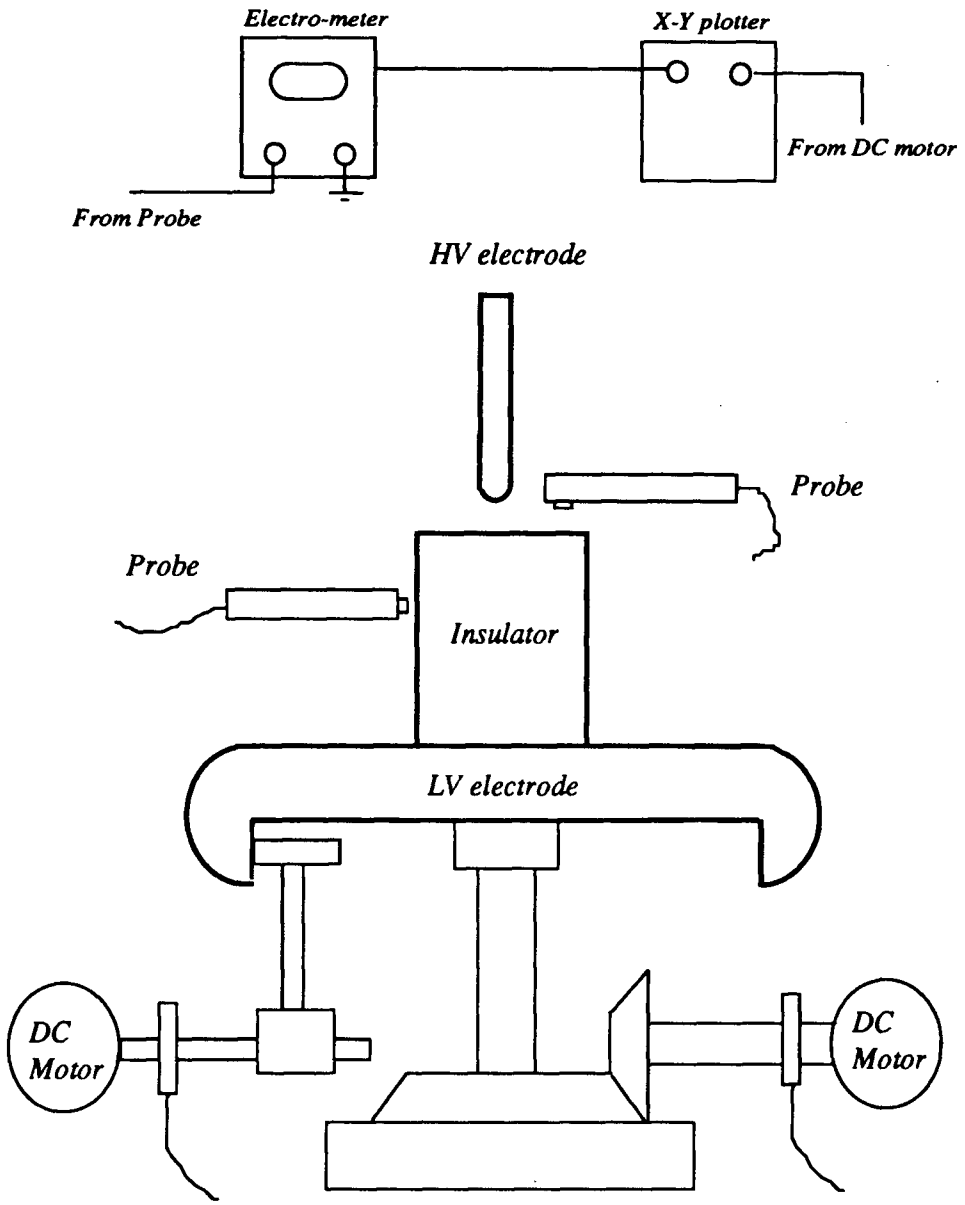

Figure 4.2 Schema of experiment setup.

The voltage source is a Haefely Muti-test system. It can generate 190 kV lighting impulses (1.2/50 μs), 180 kV switching impulses (200/2500 μs), 200 kV DC, and 80 kV_{rms} AC voltage. The maximum storage energy of the impulse generator is 300 J, the rated current of the DC source is 10 mA, and the rated output of the AC source is 5 kVA. Through a capacitive voltage divider (500 pf), the voltage is measured by an impulse peak voltmeter and displayed on a Model 5630 oscilloscope which was connected with a 6500 Biomation waveform digitizer. The model 6500 waveform digitizer is an analog-to-digital converter with a solid-state memory that stores the digital equivalent of an analogue electrical signal. This equipment can record at sample rates up to 2 ns per sample, storing 1024 sample (a 6–bit resolution per sample). The output of the Model 5600 can be interfaced to display equipment used in this research, such as oscilloscopes. The digitizer unit is triggered by the trigger spark signal from the impulse generator. The gap current can be monitored by connecting a resistor between the low voltage electrode and ground.

The pressure vessel, shown in figure 4.3, was made of steel with inside diameter 510 mm and height 1681 mm. It has four port holes. Two of the port holes, on the left and right sides, are utilized for motor shafts and two probes shafts. The port hole on the back of the vessel is used for a vacuum pipe and a gas pipe. A high pressure dial gauge and a thermocouple gauge head are connected to this flange from outside of the vessel to monitor the gas pressure and the vacuum.

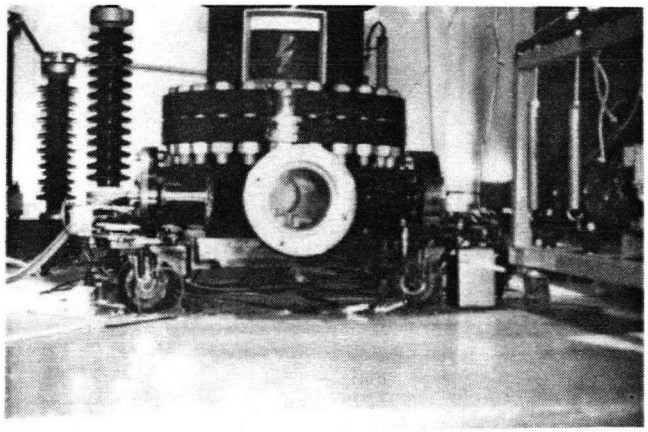

Figure 4.3 The test vessel.

The port hole on the front of the vessel is used for installations of electrodes and spacer. The test vessel is fitted with a bushing rated at 150 kV_{rms} and the highest gas pressure used is 0.3 MPa.

4.3 Testing procedure

The experimental procedures are described below:

1. Before an experiment, the spacer was ultrasonically washed with Alconox detergent for 20 minutes, rinsed in tap water, deionized water and finally dried at 65^oC for about 4 hours. Before it is introduced into the test vessel,

it was again washed with alcohol and dried under a high intensity (1000 W) lamp for 3-4 minutes to ensure that the spacer was relatively free of charge before voltage application.

2. The spacer is placed on the low voltage plane electrode after cleaning.
3. The plane electrode was lowered. The probe on the right side was introduced to be 2 mm away from the spacer top surface by operating the DC motor on the right side to adjust the plane electrode position, at each different radial position of the right probe to get a 360^oscan. The probe voltage is measured by a 610C Kiethley Electrometer and plotted on a Type 3036 X-Y plotter.
4. Once all measurements were finished on the top surface, the probe on the right side was withdrawn fully and the probe on left side was introduced, to be 2 mm away from the cylindrical side surface.
5. By operating the DC motor on the right side, the vertical position of the probe on the left side can be changed, and similar scanning is conducted. All the measurements were done in order to ensure that the spacer was relatively free of charge before voltage application.
6. The distance between the rod electrode and the top surface was adjusted by operating the DC motor on the right side.
7. If SF_6 or N_2 gas was to be used, the test vessel was evacuated to 0.01 kPa and then filled with commercially pure (99.98 %) pre-dried SF_6 or N_2 gas to the desired pressure. Absolute pressure was used in this thesis.

8. Following a voltage application, the spacer surface was scanned as described above.

Experiments were done under several voltage levels. Between the voltage applications, no attempt was made to clean the spacer surface and change the insulating gas unless flashover occurs. It will be shown in Chapter 6 that the charge pattern measured at a certain voltage level, which increased step by step from a low voltage, is similar to the charge pattern at the same voltage level which is applied to the clean spacer for the first time. After each test, compressed gas was released and spacer was cleaned following step 1 as described above. In case of flashover between the charged surface and the probe when applied voltage is increased close to flashover voltage, the gas pressure was increased a little bit before the probe was introduced for the surface charge measurements.

4.4 Surface charge measurements by capacitive probe

The insulation strength of solid dielectric spacers, sandwiched between electrodes and stressed by applied voltage, can be influenced by surface charges deposited during voltage application. The measurement of these deposited charges is difficult during the charge accumulation process, but can be carried out by means of well defined probes, by interrupting the voltage application. There are several techniques for measuring the charge distributions [44, 58–60]. The technique used in this thesis is the capacitive probe method [61–63].

The probe assembly is shown in figure 4.4. The probe sensor, which has an end diameter of 2 mm, is insulated from the shielding cylinder tube by PTFE . A coaxial cable connects the probe to a electrometer which measures the potential acquired by the probe by virtue of the static charge facing its end.

The probe, cable, and insulating spacer can be represented by a simple capacitive equivalent circuit shown in figure 4.5, where C_1 represents dielectric capacitance beneath the probe, C_2 represents the gap capacitance between the probe and spacer surface, and C_3 represents the electrometer input capacitance and cable capacitance. V_1 is the spacer surface potential and V_3 is the probe sensor potential measured by the electrometer. The measured potential V_3 is given by

$$V_3 = \frac{C_2}{C_2 + C_3} V_1 \tag{4.1}$$

The overall capacitance C between the spacer surface and earth is given by

$$C = C_1 + \frac{C_2 C_3}{C_2 + C_3} \tag{4.2}$$

So that if A is the effective area of dielectric 'seen' by the probe and σ is the surface charge density, then

$$C V_1 = A\sigma \tag{4.3}$$

Substituting equation (4.1) and (4.2) in (4.3) gives

$$V_3 = \frac{A\sigma}{C_1 + C_3 + \frac{C_1 C_3}{C_2}} \tag{4.4}$$

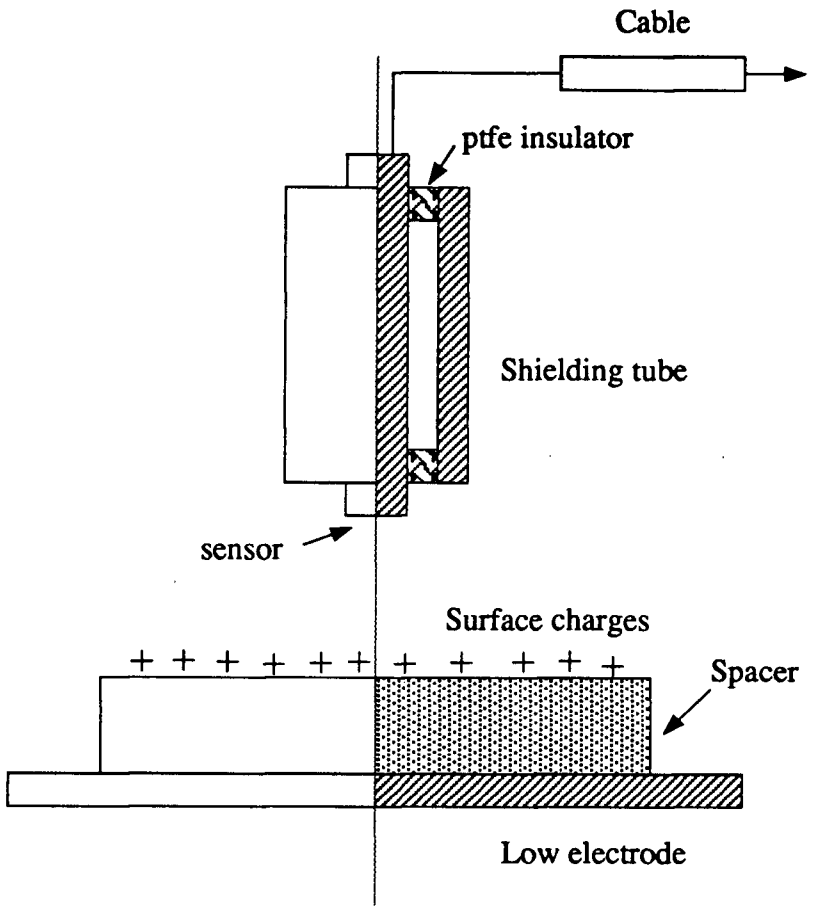

Figure 4.4 A schematic diagram of a capacitive probe.

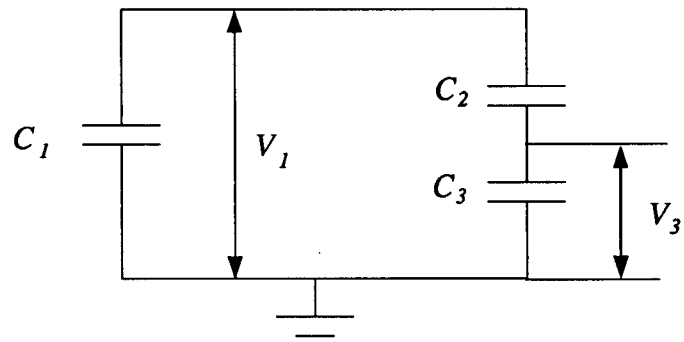

Figure 4.5 Equivalent circuit of probe assembly.

By writing $C_2 = A\varepsilon_0/d$ and $C_1 = A\varepsilon_r\varepsilon_0/t$, where d is the spacing between the probe and the surface, t the thickness of the spacer, ε_r the relative permittivity of the spacer and ε_0 the permittivity of free spacer (i.e. $8.854\times10^{-12}Fm^{-1}$), then equation (4.4) becomes

$$\sigma = \left(\frac{C_3}{A} + \frac{\varepsilon_0\varepsilon_r}{t} + \frac{C_3}{A}\frac{\varepsilon_r d}{t}\right)V_3 \tag{4.5}$$

Numerical evaluation of the charge density σ on a dielectric surface is clearly possible from the measured values of V_3 once all the terms within the bracket in equation (4.5) are known. The values of d and t can be determined by direct measurement. The ratio C_3/A for a particular probe and electrometer can be derived from a calibration test.

In the calibration test, a metal spacer maintained at a fixed potential of known value V_1 is used in place of the dielectric spacer. From equation (4.1), we have

$$V_3 = \frac{V_1}{1 + \frac{C_3}{A}\frac{d}{\epsilon_0}} \tag{4.6}$$

Therefore, C_3/A can be directly derived from the measured value V_3. This procedure applied to the probe system used in this thesis gives $\sigma = 10V_3$ for top surface and $\sigma = 8V_3$ for side surface, σ being in $\mu C/m^2$, when V_3 is measured in volts.

The measurement principle assumes that the electric field in the space between the probe head and dielectric spacer surface is uniform, i.e. d/t is small. The sensitivity and accuracy of the capacitive probe measurement depend on the spacing between probe and charged spacer surface and the probe sensor area. The smaller the spacing the higher the sensitivity of the probe. However, reducing this spacing can cause sparkovers between the charged surface and the probe. It was found that 2 mm spacing between probe and charged surface is optimum for the high sensitivity with low risk of unwanted flashover [24]. The probe resolution was determined such that the minimum line charge width that can be identified by the probes is 0.5 mm and the minimum space between positive and negative charges (with 2 mm in width) is 0.25 mm. The capacitive probe method does not provide us with a means to distinguish surface charges and bulk or volume charges. Although capacitive probe method has been a subject of controversy

[64, 65], it has been used by many investigators [32] [38] [44, 45] [47] [54] [66, 67]. It was found that the capacitive probe method is very convenient and a reasonably accurate method of measuring the magnitude and distribution of electric charges on an insulating surface. It is also a good way for comparing the measurement results and fundamental studies of mechanism of static charge generation and dissipation.

Chapter 5

Surface Charge Simulation Method

5.1 Introduction

For the field computation investigation in this thesis, the surface charge simulation method (SSM) has been chosen as the computation technique for the following reasons:

1. The rod-plane electrode geometry has open boundary.
2. There are surface charges on the cylindrical spacers.
3. It is much easier to deal with 3-D problems with SSM.
4. Normally the highest electric field locates on some special point on a electrode and can be easily obtained from the charge density at this point: $E_i = \frac{\sigma_i}{\varepsilon_0}$

The principle of SSM is that electric field strengths or potentials anywhere in a domain can be calculated by the distributed surface charges on the electrode surfaces and/or dielectric interfaces. The effect of the dielectric constant is taken into consideration by determining the distributed image charges such that

the boundary conditions are satisfied. Therefore, all dielectrics are replaced by vacuum with dielectric constant ε_0.

Some authors [24, 68–70] used sheet like charges to substitute the distributed charges on the boundary surface. If a field does not have rotational symmetry, Fourier-type surface charges, i.e. ring charges whose density varies with angle of rotation α, are used. The charge distribution is given by [71]:

$$\lambda = \sum_{\mu=0}^{n} \lambda_\mu \cos(\mu\alpha) + \sum_{\mu=0}^{n} \lambda_\mu \sin(\mu\alpha) \tag{5.1}$$

where n represents the order of the harmonic charge distribution and λ is the charge density. Considering only the cosine function in the charge representation, the potential expression at any point $P(r_p, \psi, Z_p)$ due to the mth harmonic charge, whose coordinates are $Q(r_c, \theta, z_c)$, is

$$\phi_m(r_{p,\theta,z_p}) = \frac{\lambda_\mu}{2\pi\varepsilon}\sqrt{\frac{r_c}{r_p}} Q_{\mu-\frac{1}{2}} \frac{(z_p - z_c)^2 + r_c^2 + r_p^2}{2rr_c} \cos(\mu\psi) \tag{5.2}$$

where $Q_{\mu-\frac{1}{2}}$ is referred to as the torus function. Cherukupalli successfully developed a computer program to calculate the electric field due to surface charges [24]. His results showed that the Fourier-type SSM is a good method for dealing with the field with surface charges existing on dielectric boundaries, although there are some difficulties such as CPU time and programming complexity.

Misaki et al [72, 73] divided boundary surfaces into curved triangular surface elements. The distributed surface charges on the boundary surfaces are substituted by discrete elemental charges. The charge density q_e at any point on the element is obtained from the charge density of the three vertices of the element by the following equation:

$$q_e(L_1,L_2) = L_1 q_1 + L_2 q_2 + (1 - L_1 - L_2) q_3 \tag{5.3}$$

where, q_1, q_2, and q_3 are the charge densities at vertex 1, 2 and 3 respectively. L_1, L_2, and L_3 are the area coordinates of each element. The potential and field strength at any point I are

$$V_I = \frac{1}{4\pi} \int_0^1 \int_0^{1-L_2} \frac{q_e(L_1,L_2)}{d(L_1,L_2)} |\vec{n}(L_1,L_2)| dL_1 dL_2 \tag{5.4}$$

$$E_I = \frac{1}{4\pi} \int_0^1 \int_0^{1-L_2} \frac{q_e(L_1,L_2)\vec{d}(L_1,L_2)}{d(L_1,L_2)^3} |\vec{n}(L_1,L_2)| dL_1 dL_2 \tag{5.5}$$

Because of numerical integration involved, long CPU time is need for the computation.

In order to reduce the computing time, a simplified SSM is proposed in this investigation by simply using uniform image charge density on each boundary element.

5.2 Principle of simplified SSM

5.2.1 Electric potential and electric field inside a domain

The electric potential and electric field at point j inside a domain, shown in figure 5.1, are expressed

$$\varphi(j) = \sum_{i=1}^{N} \frac{1}{4\pi\varepsilon_0} \int_{S_i} \frac{\sigma_i}{r_{ij}} dS_i \tag{5.6}$$

$$\vec{E}(j) = \sum_{i=1}^{N} \frac{-1}{4\pi\varepsilon_0} \int_{S_i} \sigma_i \cdot \mathrm{grad}\left(\frac{1}{r_{ij}}\right) dS_i \tag{5.7}$$

where σ_i is the apparent charge density of the boundary element i which has the area S_i and r_{ij} is the distance between the point j and the boundary element i. $\varphi(j)$ and $\vec{E}(j)$ are potential and electric field at the point j produced by all apparent charges on all the boundary surfaces.

Assume that charge distribution on each element is uniform, therefore

$$\varphi(j) = \sum_{i=1}^{N} \frac{S_i}{r_{ij}} \cdot \frac{\sigma_i}{4\pi\varepsilon_0} = \sum_{i=1}^{N} P(i,j) \cdot q(i) \tag{5.8}$$

$$\vec{E}(j) = \sum_{i=1}^{N} F_x(i,j)q(i)\vec{x} + \sum_{i=1}^{N} F_y(i,j)q(i)\vec{y} + \sum_{i=1}^{N} F_z(i,j)q(i)\vec{z} \tag{5.9}$$

where the equivalent apparent charge density $q(i)$ and the potential coefficient

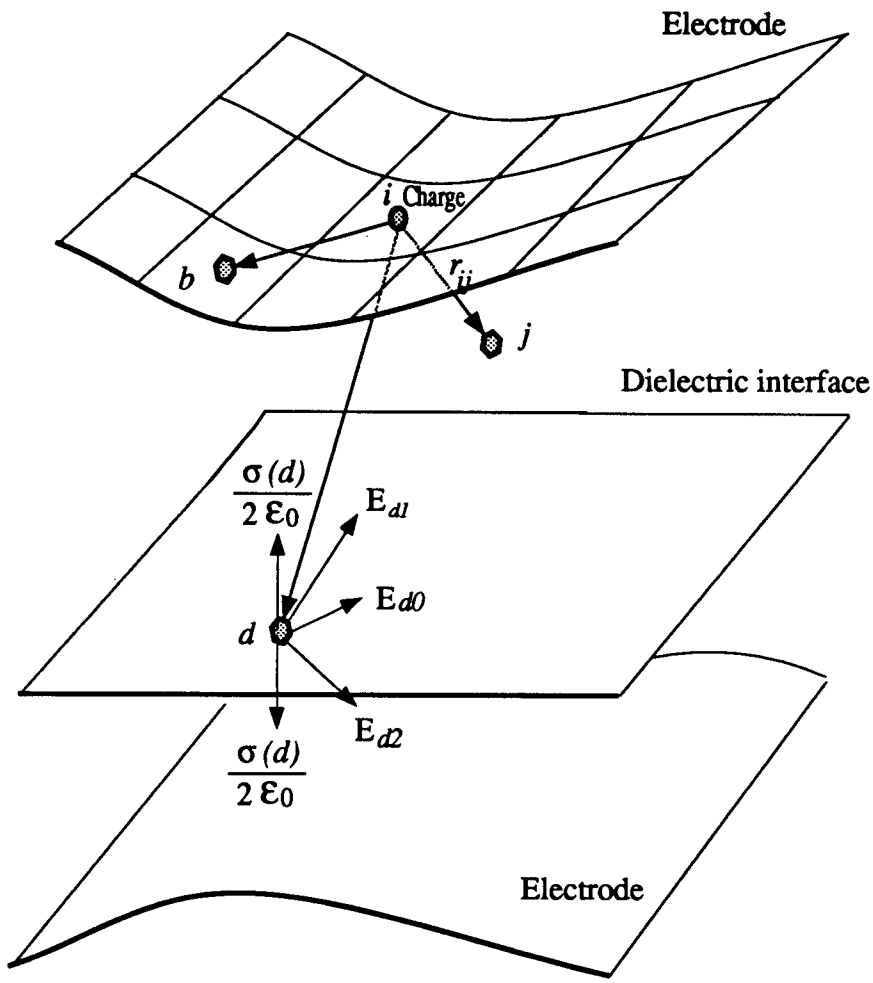

Figure 5.1 Two dielectric system.

$P(i,j)$ are given by

$$q(i) = \frac{\sigma_i}{4\pi\varepsilon_0} \tag{5.10}$$

$$P(i,j) = \frac{S_i}{r_{ij}} = \frac{S_i}{\sqrt{(X(i)-X(j))^2 + (Y(i)-Y(j))^2 + (Z(i)-Z(j))^2}} \tag{5.11}$$

Field coefficient $F_x(i,j)$, $F_y(i,j)$, and $F_z(i,j)$ are the field components on $\vec{x}$, $\vec{y}$, and $\vec{z}$ directions. They are expressed by

$$F_x(i,j) = -\frac{S_i}{r_{ij}^2} \cdot \frac{X(i)-X(j)}{r_{ij}} \tag{5.12}$$

$$F_y(i,j) = -\frac{S_i}{r_{ij}^2} \cdot \frac{Y(i)-Y(j)}{r_{ij}} \tag{5.13}$$

$$F_z(i,j) = -\frac{S_i}{r_{ij}^2} \cdot \frac{Z(i)-Z(j)}{r_{ij}} \tag{5.14}$$

5.2.2 Electric potential at boundaries

The potential equation (5.6) and the electric field equation (5.7) are continuous functions of the location of point j, differentiable to all orders everywhere except some points on boundary surfaces.

The potential at the boundary point b $(X(b), Y(b), Z(b))$ is produced by all apparent charges distributed on the boundary surfaces. If the point b coincides with

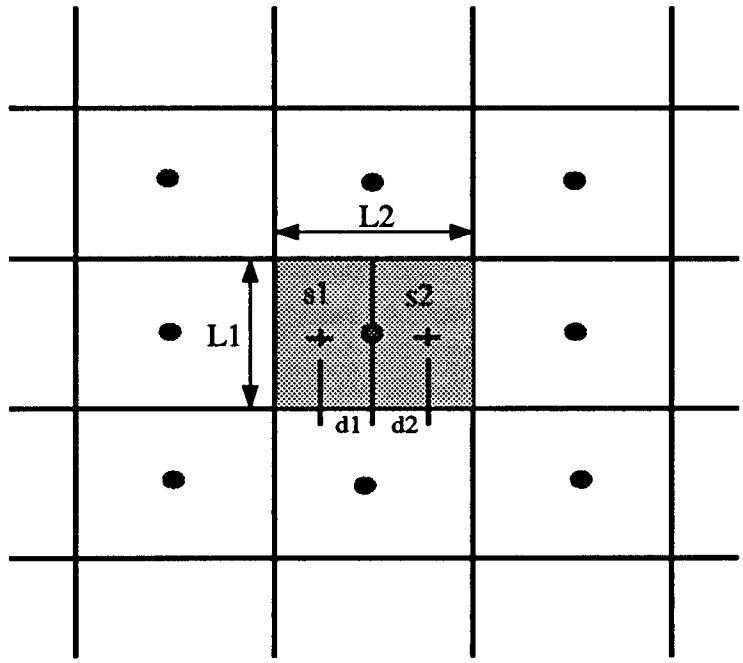

Figure 5.2 The approach to avoid a singularity.

the point i on an element at a boundary, then $X(i) - X(b) = 0$, etc. in equation (5.11) . The corresponding potential coefficient is singular, i.e. $P(i, b) = \infty$. In order to avoid the singularity, the charge element i is divided into two parts as shown in figure 5.2. The potential contributions of the two small elements are equivalent to the potential contributions of the element i.

$$\varphi(b) = \sum_{i=1, i \lesseqgtr b}^{N} P(i, b)q(i) + P(b, b)q(b) \tag{5.15}$$

where $P(i, b)$ is given by equation (5.11) when $i \lesseqgtr b$, i.e.

$$P(i, b) = \frac{S_i}{\sqrt{(X(i) - X(b))^2 + (Y(i) - Y(b))^2 + (Z(i) - Z(b))^2}} \tag{5.16}$$

The potential coefficient $P(b, b)$ at the point b is derived from the figure 5.2.

$$P(b, b) = \frac{S_1}{d_1} + \frac{S_2}{d_2} = 2\left(\frac{\frac{1}{2}L_1 L_2}{\frac{1}{4}L_2}\right) = 4L_1 \tag{5.17}$$

where $S_1 + S_2 = S_b$ (S_b is the area of the element b). L_1 and L_2 are the length and width of the element i ($i = b$).

5.2.3 Electric field at boundaries

The electric field $\vec{E}(e)$ at a point e on an electrode surface, produced by all the apparent charges on boundary surfaces, can be obtained directly from the apparent surface charge density $\sigma(e)$ at that point using the Gauss theorem:

$$\vec{E}(e) = \frac{\sigma(e)}{\varepsilon_0}\vec{n}_e \tag{5.18}$$

where $\vec{n}_e$ is the unit normal vector.

At a point d on an interface of the dielectrics, the electric field $\vec{E}_{d_1}$ on one side of the interface is different from the field $\vec{E}_{d_2}$ on the other side, figure 5.1. They are given by:

$$\vec{E}_{d_1} = \vec{E}_{d_0} + \left(\frac{\sigma(d)}{2\varepsilon_0}\right)\vec{n}_d \tag{5.19}$$

$$\vec{E}_{d_2} = \vec{E}_{d_0} - \left(\frac{\sigma(d)}{2\varepsilon_0}\right)\vec{n}_d \tag{5.20}$$

where $\vec{E}_{d_0}$ is the field intensity produced by all apparent charges except charge $\sigma(d)$ at the point d and $\vec{n}_d$ is the unit normal vector at the point d.

5.2.4 Boundary conditions

On electrode surfaces, the potential $\varphi(e)$ at a point e produced by all apparent charges on boundaries should be equal to the electrode potential V_e.

$$\varphi(e) = \sum_{j=1}^{N} P(i,j)q(j) = V_e \tag{5.21}$$

On the interface of the dielectrics, the dielectric flux is continuous at a point d if no true charges exist on the interface. We have

$$\left(\varepsilon_0\varepsilon_1\vec{E}_{d_1} - \varepsilon_0\varepsilon_2\vec{E}_{d_2}\right)\cdot\vec{n}_d = 0 \tag{5.22}$$

If there are true surface charges $\tilde{\sigma}_d$ existing on the interface, we have

$$\left(\varepsilon_0\varepsilon_1\vec{E}_{d_1} - \varepsilon_0\varepsilon_2\vec{E}_{d_2}\right)\cdot\vec{n}_d = \tilde{\sigma}_d \tag{5.23}$$

Substituting the equation (5.10), (5.19) and (5.20) into the equation (5.23), we get

$$(\varepsilon_1 - \varepsilon_2)\vec{E}_{d_0} + 2\pi(\varepsilon_1 + \varepsilon_2)q_d = \frac{\tilde{\sigma}_d}{\varepsilon_0} \tag{5.24}$$

where $\tilde{\sigma}_d$ is the true surface charge density locating on the interface at point d and q_d is the equivalent apparent charge density at point d on the interface. Therefore, the equation(5.21) and (5.24) give the boundary conditions.

On electrode surface:

$$\sum_{j=1}^{N} P(i,j)q(j) = V_c \tag{5.25}$$

On dielectric interface:

$$\sum_{j=1}^{N} f(i,j)q(j) = \frac{\tilde{\sigma}_d}{\varepsilon_0} \tag{5.26}$$

5.2.5 System equations

From equation (5.25) and (5.26), the system equations are given by

$$\begin{bmatrix} P(i,j) \\ F(i,j) \end{bmatrix} \begin{Bmatrix} q_1 \\ q_2 \\ \cdot \\ \cdot \\ q_n \end{Bmatrix} = \begin{Bmatrix} Ve \\ \cdot \\ \cdot \\ \cdot \\ \frac{\tilde{\sigma}_d}{\varepsilon_0} \end{Bmatrix} \tag{5.27}$$

i.e.

$$[P][Q] = [V] \tag{5.28}$$

Coefficient matrix $[P]$ consists of potential coefficient $P(i,j)$ and electric field coefficient $F_d(i,j)$ ($F_d(i,j)$ is the field coefficient component on the unit normal vector $\vec{n}_d$ direction). Vector $[V]$ consists of electrode potential V_e and true surface charge $\tilde{\sigma}_d$, which can be obtained from probe measurements on the dielectric interfaces. Vector $[Q]$ contains the apparent charges on the boundary surfaces. $[P]$ and $[V]$ are known. $[Q]$ is unknown, which can be solved from the equation (5.28). Once we know the apparent surface charges on the boundaries,

electric potential and electric field anywhere in a domain or on a boundary can be obtained directly from equation (5.8) and (5.9).

5.3 Examples and calculation accuracy

In order to examine the proposed SSM numerical calculation method and its accuracy, two examples were considered. They are a coaxial cylinder model and a rod-plane model. The coaxial cylinder model is chosen because its analytical solution can be obtained so that the accuracy of the proposed SSM method can be examined. For the rod-plane model, a numerical solution can be obtained from the CSM program developed by Cherukupalli [24], so that the numerical solution of the proposed SSM program can be compared.

5.3.1 Coaxial cylinder model

Consider a coaxial cylinder model as shown in figure 5.3. In the vertical direction, the surfaces were divided into five parts. In the circumferential direction, the internal electrode surface was divided into ten parts and the external electrode surface was divided into eleven parts. The element areas are 12.6 mm^2 on the internal cylinder surface and 34.3 mm^2 on the external cylinder surface. Apparent charge density on each element is assumed to be uniform. The calculation results of the proposed SSM method were compared to the theoretical values of an infinitely long cylinder. The results are shown in figure 5.4.

Figure 5.4 shows that the SSM numerical calculation results are reasonably accurate in comparison with the theoretical values. The average potential error is 12.9 % and electric field error is 2.3 %. The calculation error in field intensity is smaller than the electric potential error in the case of coaxial cylinder model. It is known that the field calculation error by finite element method or by charge simulation method is ten times larger than potential error [74, 75]. Therefore, comparing with the CSM or finite element method the proposed surface charge simulation method (SSM) has an advantage in getting a high field calculation accuracy.

5.3.2 Rod-plane model

The rod-plane model is shown in figure 5.5. The low voltage plane electrode surface was divided into ten parts in the circumferential direction and five parts in the radial direction so that the element areas varied from 5.0 mm^2 to 45.0 mm^2. The high voltage rod electrode surface was divided into ten parts in the circumferential direction and six parts in the vertical direction. The element area on the rod electrode was 0.53 mm^2. The numerical calculation results of potential and electric field along the axis between the rod electrode and the plane electrode by the SSM are compared with the results obtained from the CSM program, as shown in figure 5.6. The two calculation results are very close. However, the calculation time of the SSM program is much shorter than the calculation time of the CSM program. This is another advantage of the SSM for the system with

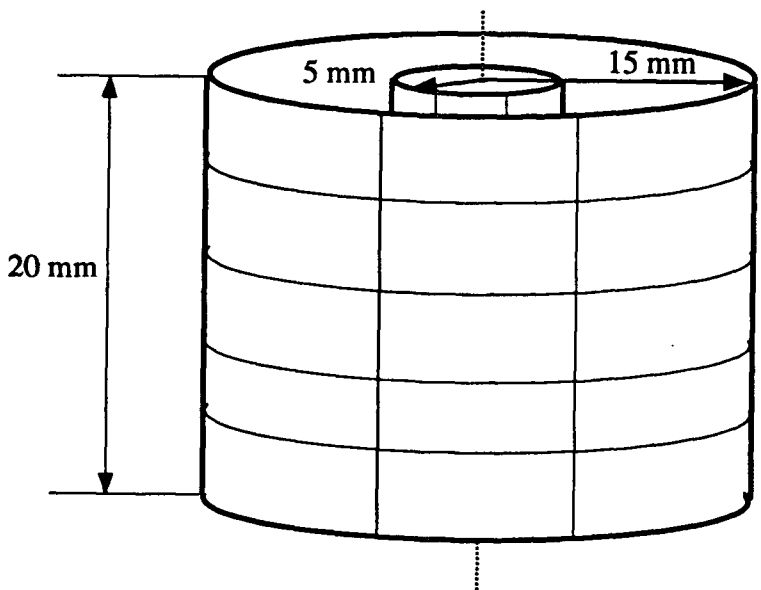

Figure 5.3 The coaxial cylinder model.

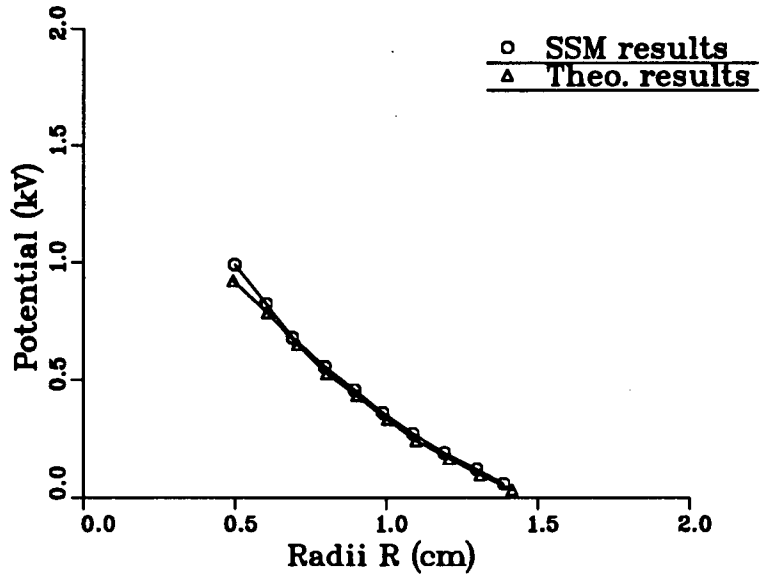

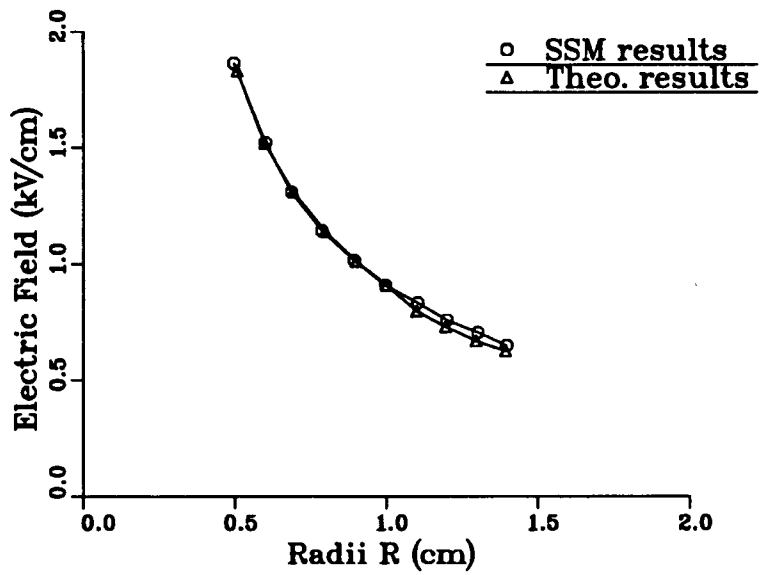

Figure 5.4 Calculation results for the coaxial cylinder model at 1.0 kV applied voltage.

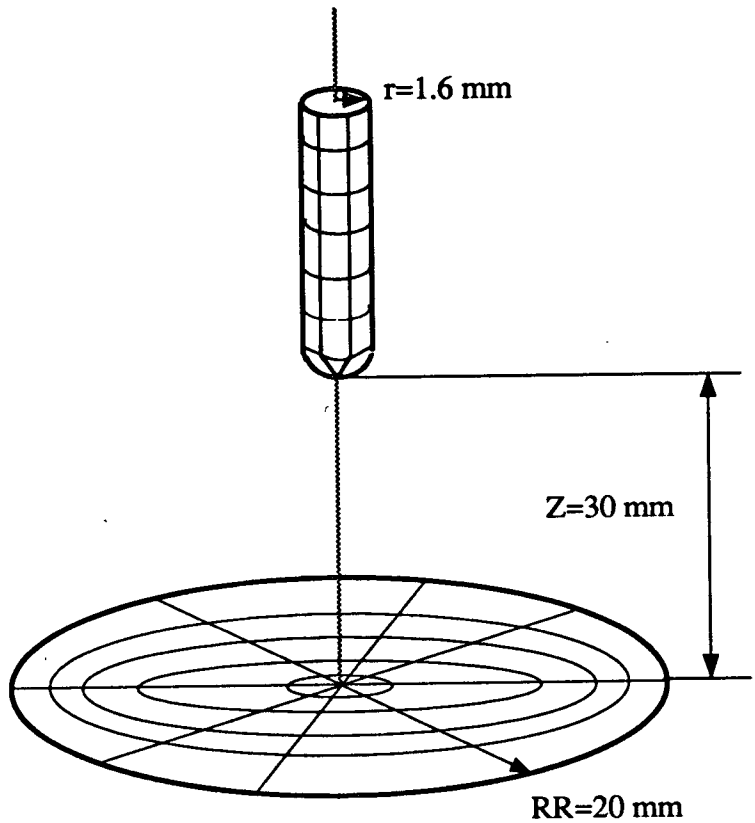

Figure 5.5 The rod-plane model.

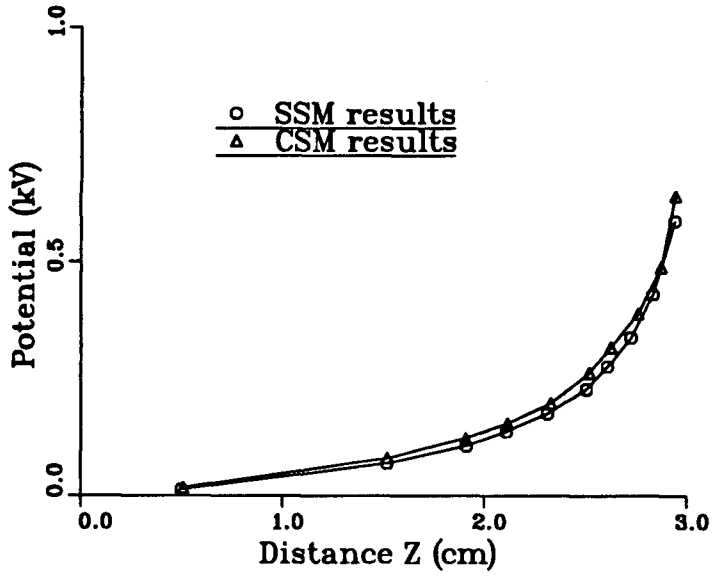

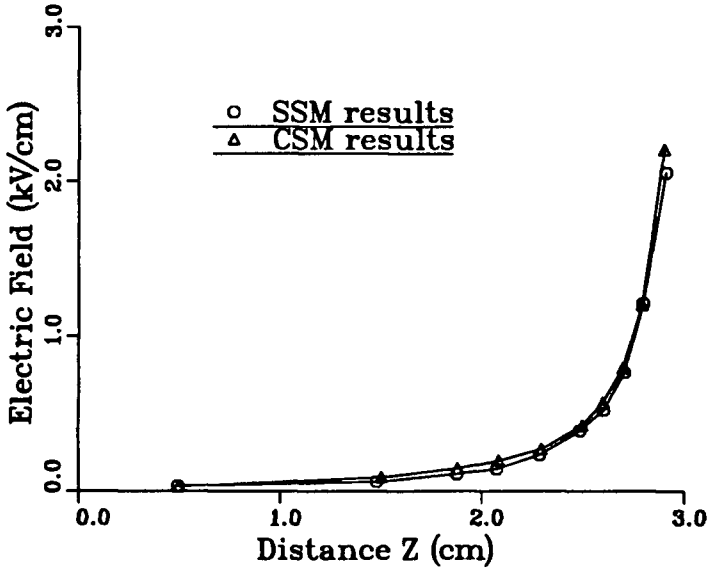

Figure 5.6 Calculation results for the rod-plane model at 1.0 kV applied voltage.

complex boundaries. Using the CSM method, it is very difficult to arrange line charges, ring charges etc. to fit the complex boundary conditions while using SSM method, complex boundary conditions do not increase calculation complexity a great deal and small boundary surfaces make calculation even simpler.

Chapter 6

Experimental Results and Discussions

6.1 Introduction

In this chapter, the experiments to study the mechanisms and factors governing surface charge accumulations are discussed. A rod-spacer-plane geometry, as shown in figure 4.1, was used in this research. Such a geometry represents very onerous conditions encountered in practice for corona charging. Moreover, the considerable data available from previous work for the same geometry [24] would be used as a comparison. Standard lightning impulses and DC for either 5 minutes or 30 minutes, at various levels, were used as applied voltages. Two spacer materials (PTFE and nylon) and three insulating gases (air, N_2, and SF_6) were used in the experiments.

Experiments were arranged and conducted in such a way that the surface charge sources and governing factors were studied. Surface charges were measured under different impulse voltage levels and compared with the corresponding corona inception voltages calculated by the charge simulation method (CSM). It was found that surface charging is closely related with corona discharges. Surface

charge accumulations were also studied at different gas pressures. Photoionization was identified as one of the sources of surface charge accumulation at high gas pressure and high applied voltage. By varying the degree of non-uniformity in the ambient electric field, that is, with different diameter rod electrodes and spacer materials with different dielectric constant, surface charge distributions and magnitudes were found to be very much field dependent. Lightning impulse pre-charging was utilized to study the pre-charging effect on surface charge patterns. Finally, the experiments in three different gases (air, N_2, and SF_6) with impulse and DC voltages show that electronegative characteristic of SF_6 inhibits surface charging and results in considerably lower surface charge accumulation when compared with a non-attaching gas like N_2.

6.2 Corona and surface charging

From previous studies, it was found that no noticeable surface charges were observed in the experiment with plane-parallel electrode after impulse voltage applications [24]. However, in an experiment conducted with an imperfect spacer (which had its edge damaged accidentally) higher levels of charge were measured on the spacer surface at the same voltage levels. This could be attributed to the field enhancement created by this imperfection. The distorted electric field leads to partial discharges due to the resulting high stress in the localized area even at low voltages. In order to study how surface charging relates to corona discharges,

a rod-plane electrode geometry, with a cylindrical insulating spacer in between, is used in this research.

The charge density distribution on a PTFE spacer surface was measured as a function of increasing applied voltages and gas pressures. Before voltage application, the charge density on the spacer surface was measured to confirm that the residual charge on the spacer surface was sufficiently low ($\pm 0.5 \mu C m^{-2}$) and this result is shown in figure 6.1. The X-dimension is defined in figure 6.2 for 3D graphs.

One positive lightning impulse voltage was applied at each voltage level commencing from a relatively low level (27 kV for PTFE). No attempt was made to discharge the spacer between each impulse application. The charge density at the top surface is negative (possibly due to the initial residual charge) at low voltage level, and changes its polarity to a positive value with the charge density increasing gradually with the applied voltage as shown in figure 6.3.

The computed corona inception voltage for the rod-plane electrode with cylindrical spacer is based on a technique developed by Parekh et al [20]. They computed the corona inception voltage for a spherical particle resting between plane-parallel electrodes with a dielectric coating. In their technique, however, they had assumed that the relative permittivity ε_r of the insulating coating was unity to simplify the computation. In this work the field computations were done accounting for the relative permittivity of the insulating spacer using a charge

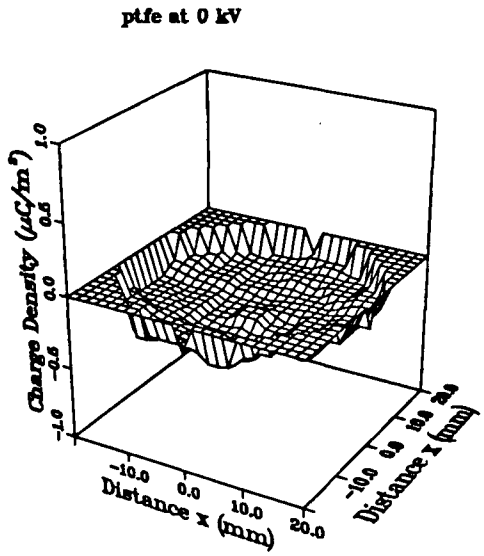

Figure 6.1 Residual charges on PTFE top spacer surface before voltage applications.

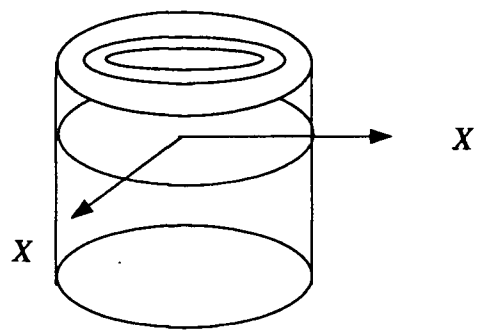

Figure 6.2 X-dimension diagram for 3D graphs.

simulation technique (CSM). The principal assumption made here was that at a voltage close to corona inception, since the residual charge on the spacer was low, these charges do not perturb the overall electric field distribution.

Figures 6.3 and 6.4 show the surface charge accumulation on PTFE spacer surface. The rod electrode diameter is 3.2 mm and there is no gap between the rod electrode and the spacer. The corona inception voltages calculated for this geometry were 17.3 kV at 0.1 MPa, 31.0 kV at 0.2 MPa, and 44.5 kV at 0.3 MPa.

Before voltage application, there are some negative residual charges on the spacer surface. With 27 kV positive lightning impulse voltage application, there are some very weak corona discharges on the spacer surface at 0.1 MPa gas pressure. The initial negative charge density is neutralized by the positive charges due to the corona. Therefore, the negative charge density is reduced after the voltage application. With 0.2 MPa and 0.3 MPa gas pressure, the corona inception voltages are higher than the applied voltage 27 kV. Therefore the charge distributions with 27 kV positive lightning impulse applied voltage under 0.2 MPa and 0.3 MPa remain the same as the charge distribution before the voltage application. It is interesting to observe from the figure 6.3 that the charge density on the spacer top surface changes its polarity at approximately the calculated corona inception voltage, suggesting that the onset of corona caused the observed charge deposition. At 0.3 MPa with a 60 kV impulse voltage, corona streamer partially neutralizes and charges positive charges on the part of the top surface.

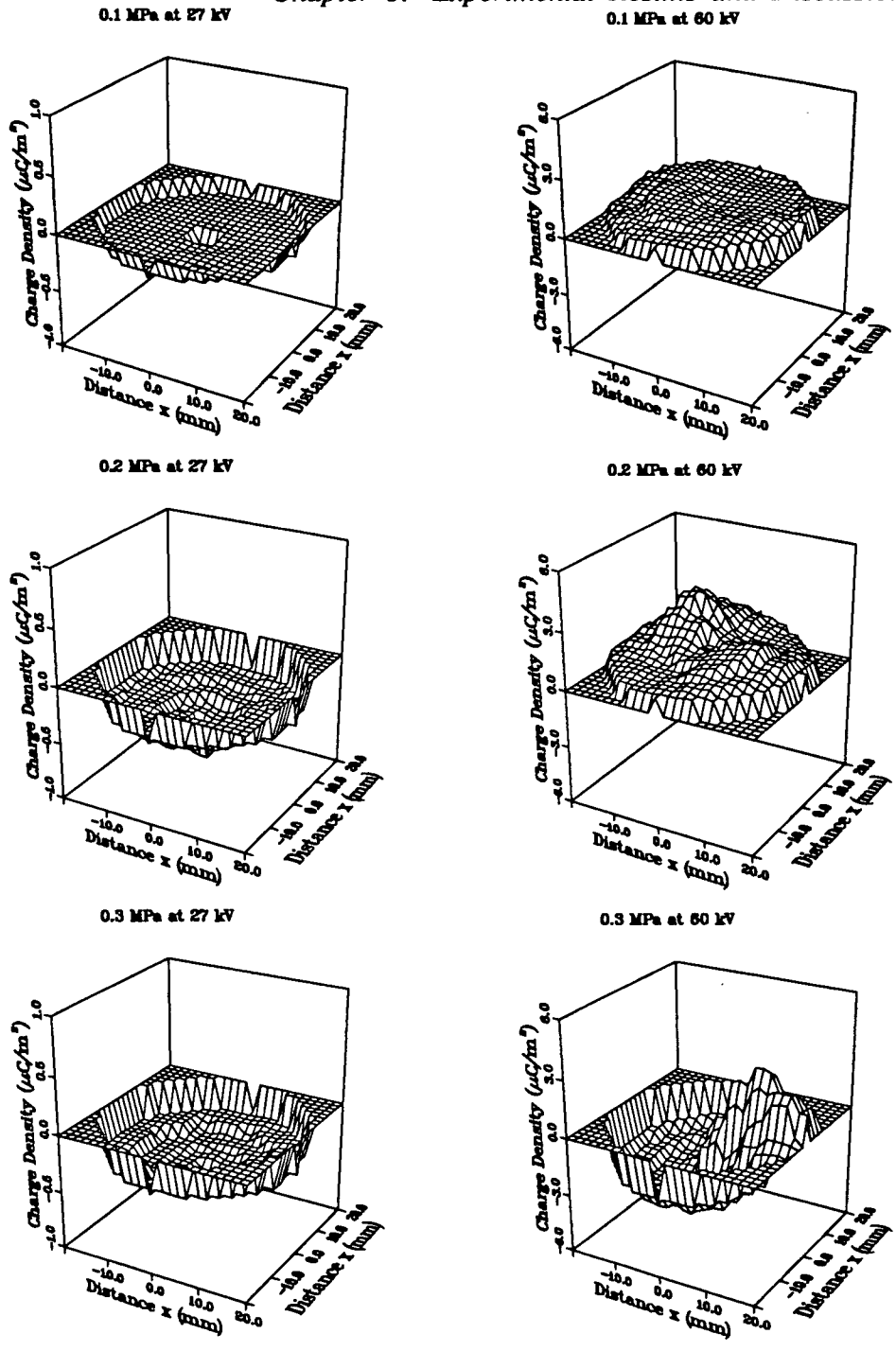

Figure 6.3 Charge patterns on PTFE spacer top surface under 27 kV and 60 kV lightning impulse voltages at three SF_6 gas pressures with 3.2 mm rod diameter.

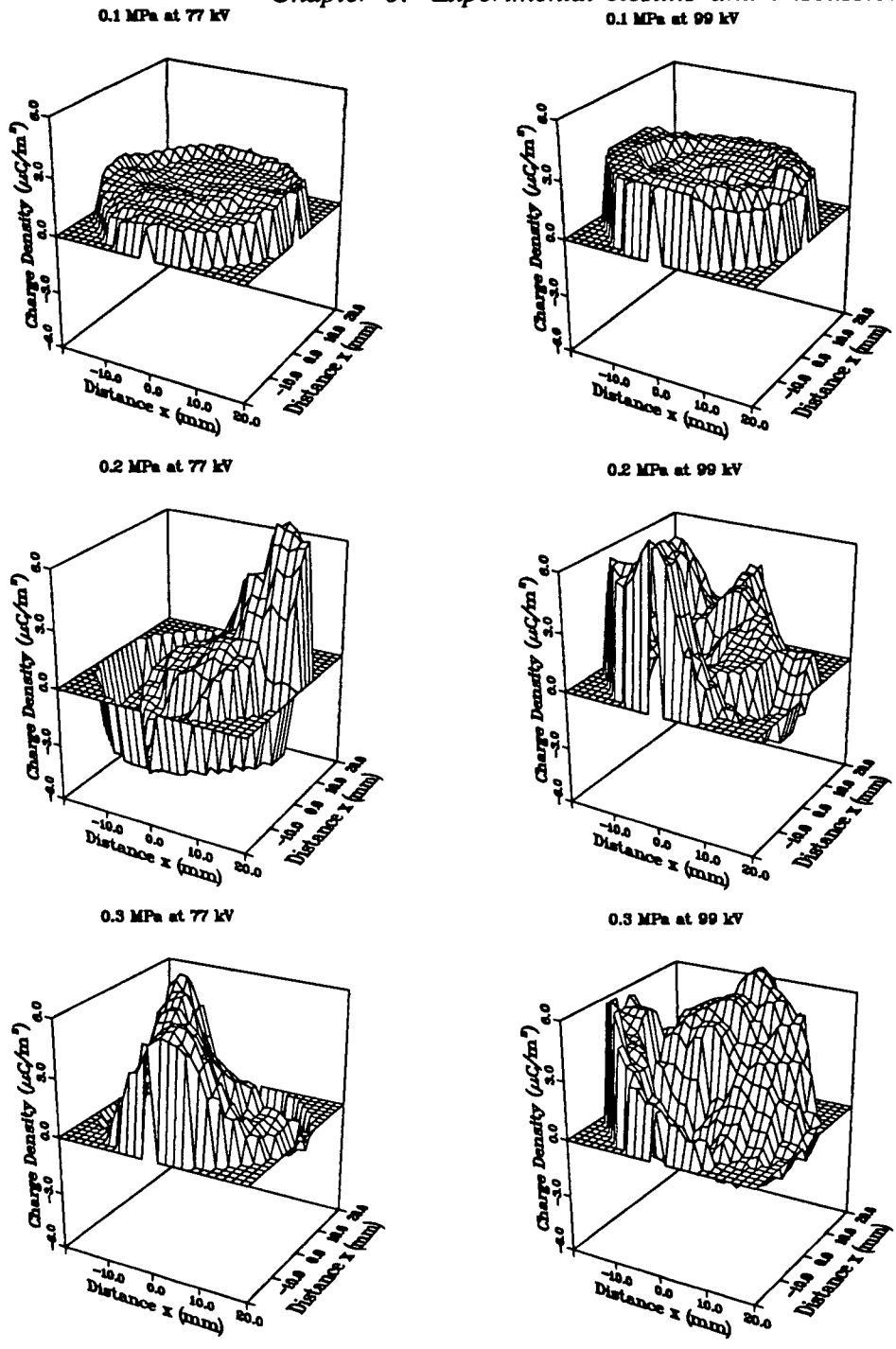

Figure 6.4 Charge patterns on PTFE spacer top surface under 77 kV and 99 kV lightning impulse voltages at three SF_6 gas pressures with 3.2 mm rod diameter.

Comparing figure 6.4 with figure 6.3, it can be seen that maximum positive charge magnitude is significantly increased when applied voltage is much higher than corona inceptions at each gas pressure level.

Figure 6.5 and figure 6.6 show the surface charge distribution on nylon spacer top surface for two voltages (27 kV and 51 kV) and three gas pressures with the same electrode configuration. Positive lightning impulses were applied at each voltage level commencing from a relatively low level (27 kV). At this voltage there is a concentration of positive charges on the spacer in the vicinity of the rod electrode. As expected at 27 kV, the charge magnitude on the center decreased as the gas pressure increases. Calculations of the corona inception voltage for each gas pressure resulted in values of 14 kV at 0.1 MPa, 24.4 kV at 0.2 MPa, and 34.8 kV at 0.3 MPa. Obviously due to the higher dielectric constant of nylon ($\varepsilon_r = 3.8$), the corona inception voltages are lower at all pressures when compared to PTFE ($\varepsilon_r = 2.1$). It is also interesting to observe that close to the calculated corona inception voltage there is a dramatic change from the initial charge distribution. At 0.3 MPa gas pressure the corona inception voltage is higher, thus at 27 kV, there is no significant change in the charge distribution on the spacer as compared to the initial charge distribution prior to voltage application. It is also seen from figure 6.6 that at higher voltages charges spread to the edge of the spacer surface.

Figures 6.7 to 6.10 show the charge distributions on the cylindrical side surface

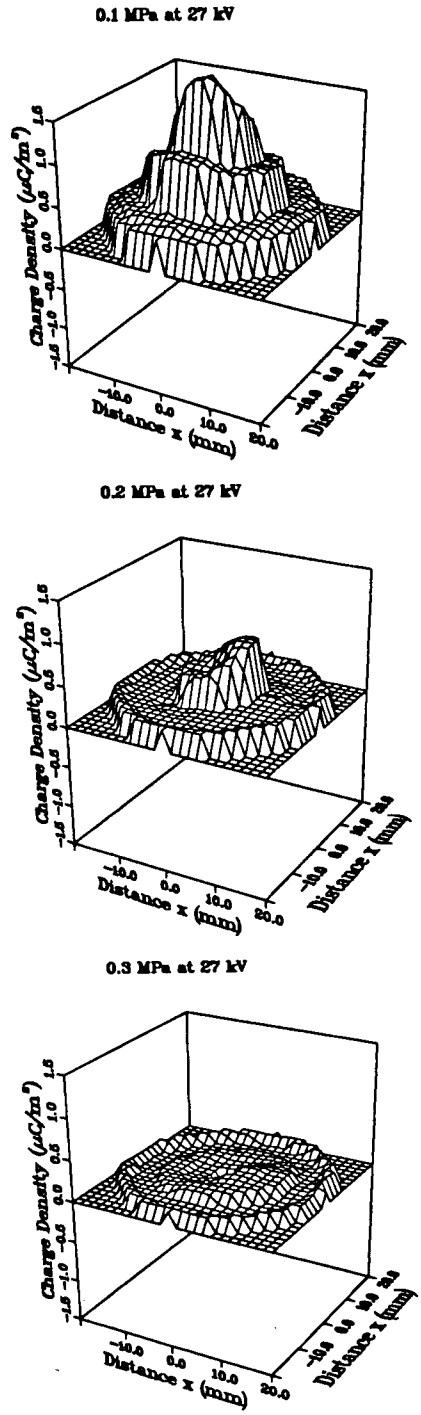

Figure 6.5 Charge accumulation on nylon spacer top surface under 27 kV lightning impulse voltages at three SF_6 gas pressures with 3.2 mm rod diameter.

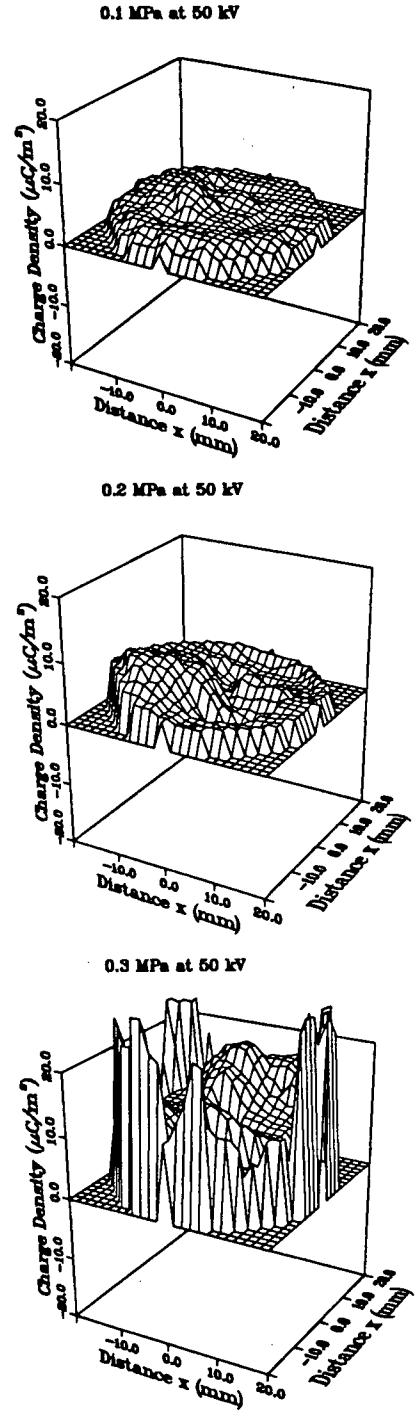

Figure 6.6 Charge accumulation on nylon spacer top surface under 50 kV lightning impulse voltages at three SF_6 gas pressures with 3.2 mm diameter rod.

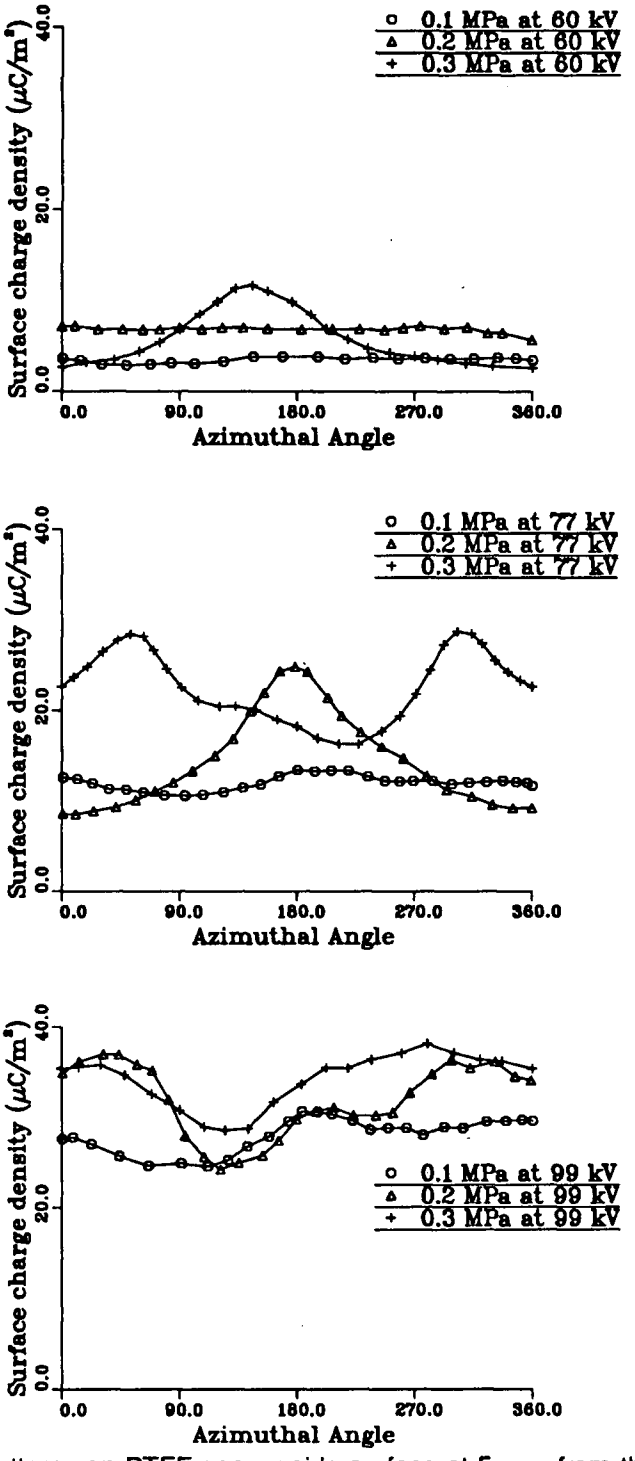

Figure 6.7 Charge patterns on PTFE spacer side surface at 5 mm from the top edge under lightning impulses with 3.2 mm diameter rod.

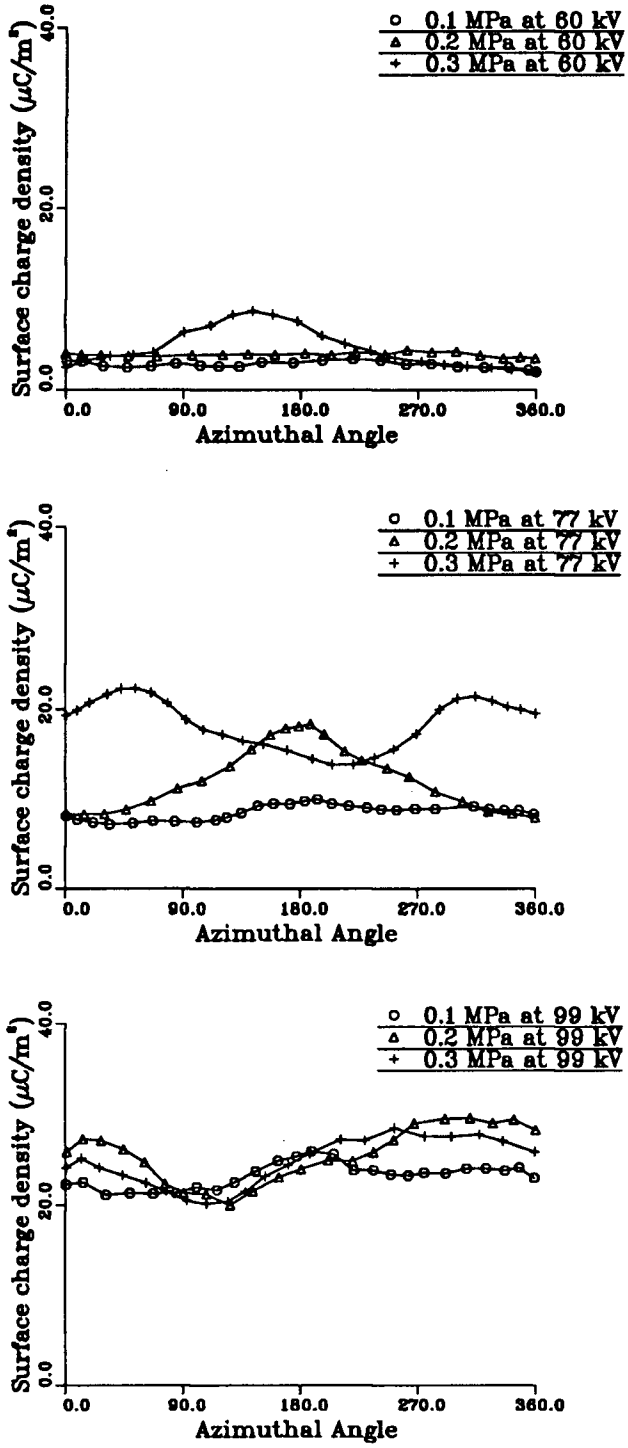

Figure 6.8 Charge patterns on PTFE spacer side surface at 10 mm from the top edge, under lightning impulses with 3.2 mm diameter rod.

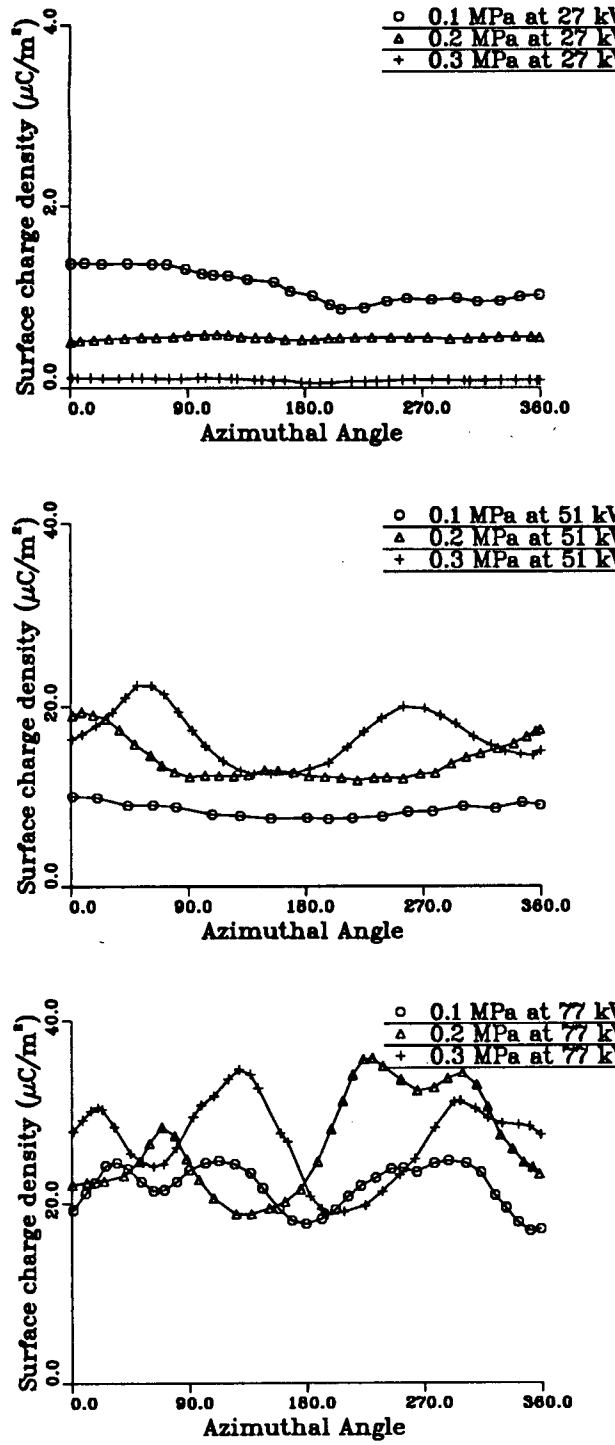

Figure 6.9 Charge patterns on nylon spacer side surface at 5 mm from the top edge, under lightning impulses with 3.2 mm diameter rod.

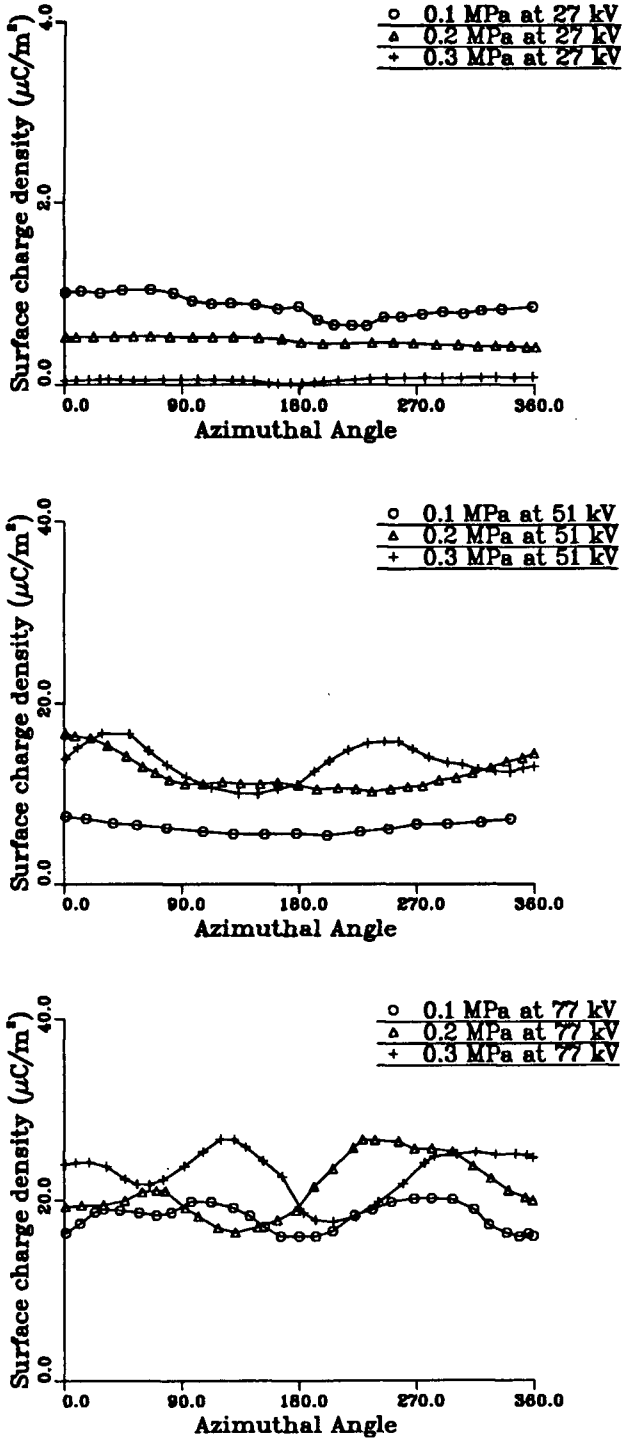

Figure 6.10 Charge patterns on nylon spacer side surface at 10 mm from the top edge, under lightning impulses with 3.2 mm diameter rod.

measured at two different heights (5 and 10 mm) from the top edge of PTFE and nylon spacers. Once again, it is observed that when a voltage is higher than corona inception surface charges have a dramatic increase.

Moreover, for applied voltages well above the corona inception the observed peak charge density tends to saturate with voltage and gas pressure (figure 6.4, figure 6.7 to figure 6.10). At a given gas pressure and electrode-spacer geometry, the charge density at the center of the top surface of the spacer initially increases with applied voltages. The charge distribution, however, becomes more and more non-uniform as the applied voltage and gas pressure increase, indicating that perhaps local surface discharges take place on each impulse voltage application [32, 76]. At an applied voltage slightly above the corona onset, there is negligible charge accumulation on the cylindrical surface of a spacer. As the applied voltage increases, the length and number of positive streamers would increase [76] and the charge magnitude observed on the cylindrical surface should also increase.

6.3 Surface charge variation with gas pressures

In a conventional GIS, the operating gas pressures typically vary between 0.1 MPa and 0.4 MPa. Therefore, the phenomenon of spacer surface charge accumulation at higher pressure would be of practical interest.

Figures 6.5 and 6.6 show the charge accumulations on nylon spacer top surface in SF_6 gas with 3.2 mm diameter rod electrode. The surface charge density

decreases with the gas pressure at low applied voltage level (27 kV) as shown in figure 6.5, but increases with the SF_6 gas pressure at high voltage level (51 kV) as shown in figure 6.6. Figures 6.3 and 6.4 show the charge accumulations on PTFE spacer top surface in SF_6 gas with 3.2 mm diameter rod electrode at different gas pressures. At 27 kV impulse voltage level, no positive charges were found on the spacer surface, but the negative charge magnitudes at 0.1 MPa gas pressure are much smaller than the initial negative charges, which were kept the same at higher gas pressures. When the applied voltage was much higher than all the corona inception voltages (17.3 kV, 31.0 kV , and 44.5 kV at 0.1 MPa, 0.2 MPa, and 0.3 MPa respectively), positive charges were found on the PTFE top surface. The maximum charge magnitudes at 60 kV, 77 kV, and 99 kV impulse voltages increase with the gas pressure from 0.1MPa to 0.2 MPa, and saturate at the gas pressure from 0.2 MPa to 0.3 MPa. Another significant observation is that at a given voltage the inhomogeneity in surface charge distribution increases with gas pressure. For example, in figure 6.3 and figure 6.4 the surface charges under 0.1 MPa gas pressure at 60 kV, 77 kV, and 99 kV impulse voltages are positive and have more or less uniform distribution. However, the surface charges under 0.2 MPa or 0.3 MPa gas pressures at the same voltage levels are bipolar and have very non-uniform distribution.

These phenomena were confirmed by the surface charge patterns on spacer side surfaces, as shown in figures 6.7 and 6.8 for PTFE spacer and figures 6.9

and 6.10 for nylon spacer. The surface charge distributions on the side surface of a spacer were measured at two different heights (5 and 10 mm) from the top edge of the spacer. The plots have been arranged as to show the effects of both voltage and gas pressure on the nature of the charge accumulation. In figure 6.7 and 6.8 for PTFE spacer at voltage 60 kV, 77 kV, and 99 kV impulse voltages, which are much higher than the corona inception voltages, the maximum surface density increases with gas pressures and saturates at high applied voltage under high gas pressure, for example, at 99 kV with 0.3 MPa gas pressure. In figure 6.9 and figure 6.10 for nylon spacer, with gas pressure changing from 0.1 MPa to 0.3 MPa, the charge magnitude decreases at 27 kV impulse voltage and increases at 51 kV impulse voltage. At 77 kV voltage level, the maximum surface charge magnitude increases from gas pressure 0.1 MPa to 0.2 MPa and saturates at gas pressure 0.2 MPa to 0.3 MPa. Also, inhomogeneity in surface charge distributions for both nylon and PTFE increases with gas pressures. For example, in figure 6.9 at 51 kV the charge distribution is almost uniform at 0.1 MPa gas pressure and with the average around 11 $\mu C/m^2$ while the charge distribution at 0.3 MPa has a large variation with maximum value 22 $\mu C/m^2$ and minimum value 15 $\mu C/m^2$.

Under a higher gas pressure, ionization does not occur easily by one collision because of shorter mean free path. Therefore, the corona inception voltage of a system increases with the gas pressure. The corona inception voltages for the configuration in figures 6.5 and 6.6 with nylon spacer are 14.0 kV, 24.4 kV,

and 34.8 kV at 0.1 MPa, 0.2 MPa, 0.3 MPa respectively. As discussed before surface charge initiation is closely related with the corona phenomena. As shown in figures 6.5, applied voltage 27 kV is higher than the corona inception voltage (14.0 kV) of the system under 0.1 MPa gas pressure, therefore there are significant surface charges on the spacer surface. Under 0.2 MPa gas pressure, the corona inception voltage (24.4 kV) is very close to the applied voltage 27 kV, therefore we can see some charges located on the center part of the top surface. when the gas pressure goes up to 0.3 MPa, the corona inception voltage (34.8 kV) is higher than the applied voltage 27 kV, therefore there are almost no charges on the spacer surface.

When an applied voltage is much higher than the corona inception voltage of a system, avalanches progress. During avalanche propagation, excitation of gas atoms in the vicinity occurs. The excited states have lifetime that can be as short as 10^{-13} second [56]. Photons will be emitted from these excited states as they return to the ground state during avalanche propagations. The number of photons increases with gas pressure [77]. These photons head in all directions and are absorbed at various distances from their origin. These distances, which are called optical path lengths, depend on the gas pressure as shown in equation (6.1):

$$q = \frac{T}{273} \cdot \frac{760}{P} \cdot \frac{1}{x} \cdot \frac{1}{n} \cdot \ln\left(\frac{I_0}{I}\right) \qquad cm^2 \tag{6.1}$$

where q is the absorption coefficient ($\sim$ 10^{-18} cm^2), n is the atomic or

molecular number density at 273 K and 760 Torr $(\approx 2.69 \times 10^{19}\ cm^{-3})$, T is the temperature and P is the gas pressure and x is the optical path length [57].

According to the above equation, the optical path lengths are 0.85 mm at 0.1 MPa, 0.43 mm at 0.2 MPa, and 0.21 mm at 0.3 MPa, corresponding to 90% photon absorption within these lengths. Photon absorption may lead to photoionization.

$$A + h\nu \rightarrow A^{+} + e \tag{6.2}$$

New electrons move rapidly toward the anode leaving behind positive ions. The optical lengths under different gas pressure are all much shorter than the distance between the probe head and spacer surface (i.e. 2 mm). Most of the positive ions caused by photoionization during avalanche propagation along the spacer surface are located near the surface, which can be scanned by probes after voltage applications. The surface charges due to photoionization may be increased under higher gas pressure due to the greater number of photons and the shorter optical lengths.

As comparisons, experiments under different gas pressures are also done in air and nitrogen gases. Figure 6.11 and figure 6.12 show the experimental results in air at 25 kV and 32 kV impulse voltages under three different gas pressures namely 0.1 MPa, 0.2 MPa, and 0.3 MPa. In air, the corona inception voltages are 12 kV, 21 kV, and 28 kV at 0.1 MPa, 0.2 MPa, and 0.3 MPa respectively for the configuration with 3.2 mm diameter rod electrode and no gap between the

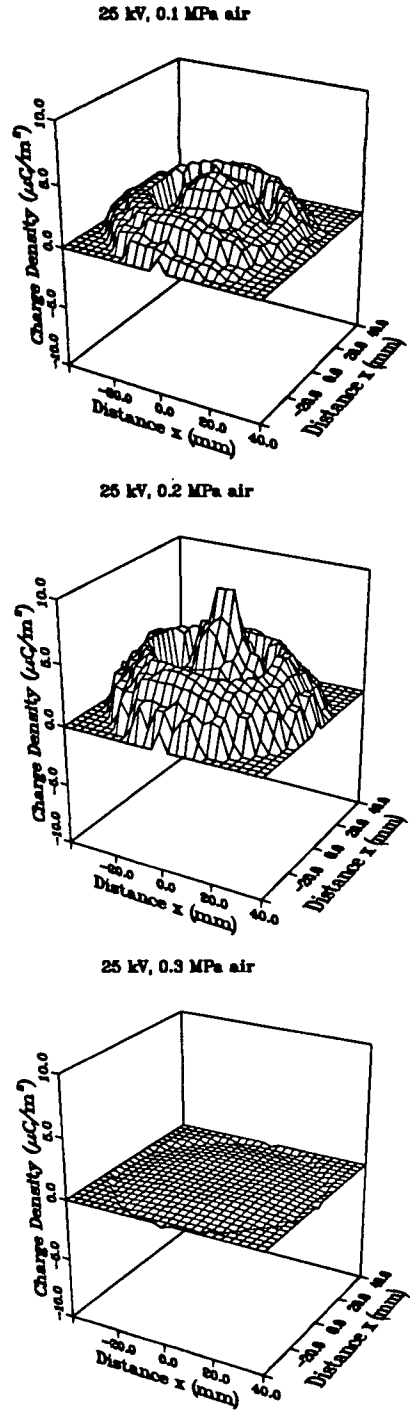

Figure 6.11 Surface charge patterns on nylon spacer surface under 25 kV lightning impulse with 3.2 mm rod diameter in air.

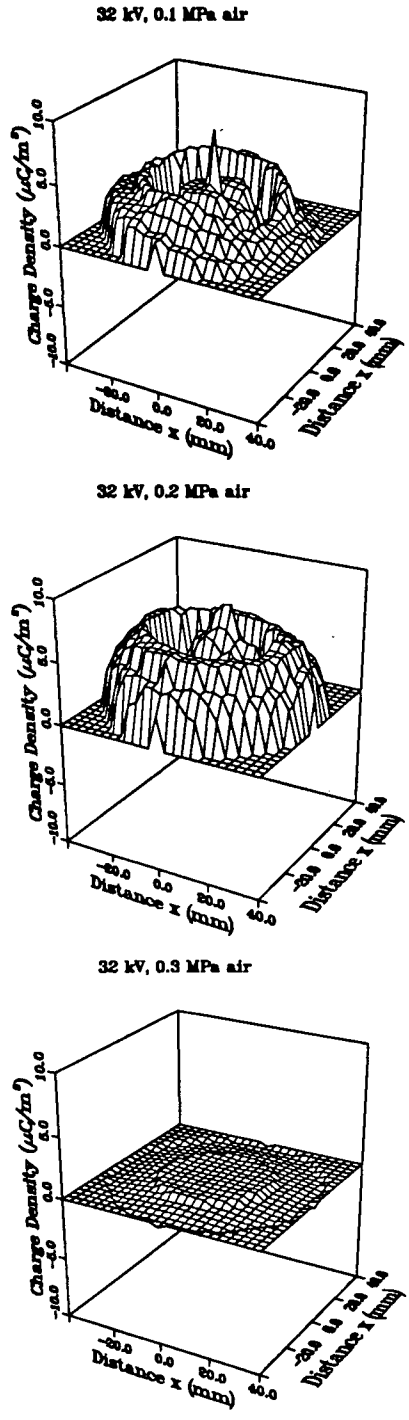

Figure 6.12 Surface charge patterns on nylon spacer surface under 32 kV lightning impulse with 3.2 mm rod diameter in air.

rod electrode and the spacer top surface. At gas pressures of 0.1 MPa and 0.2 MPa, significant positive surface charges were observed at both voltages 25 kV and 32 kV, which are higher than the corona inception voltages, and the charge magnitude increased with gas pressure. Under 0.3 MPa gas pressure, no positive charges were observed at 25 kV because the applied voltage is lower than the corona inception voltage of 28 kV. Slight positive charges were observed on spacer top surface at 32 kV, which is slightly higher than the corona inception voltage of 28 kV.

Figure 6.13 and figure 6.14 show the experimental results in nitrogen at 25 kV and 32 kV impulse voltages under 0.1 MPa, 0.2 MPa, and 0.3 MPa gas pressure. In nitrogen, the corona inception voltages are 13 kV, 20 kV, and 25 kV at 0.1 MPa, 0.2 MPa, and 0.3 MPa respectively. It appears to be true for SF_6 and air that surface charge density increases with gas pressure when applied voltage is much higher than the corona inception, while it does not appear to be true for N_2. The surface charge densities at both voltage 25 kV and 32 kV impulse voltage decrease with gas pressure.

The common feature of SF_6 and air is that they are electronegative. Electrons easily attach to molecules to form negative ions in electronegative gases like SF_6. A general criterion for negative-ion stability can be inferred from consideration of the neutral atom, which is stable because it possesses the lowest energy level of all the possible states, its total energy will be required to "knock out" the

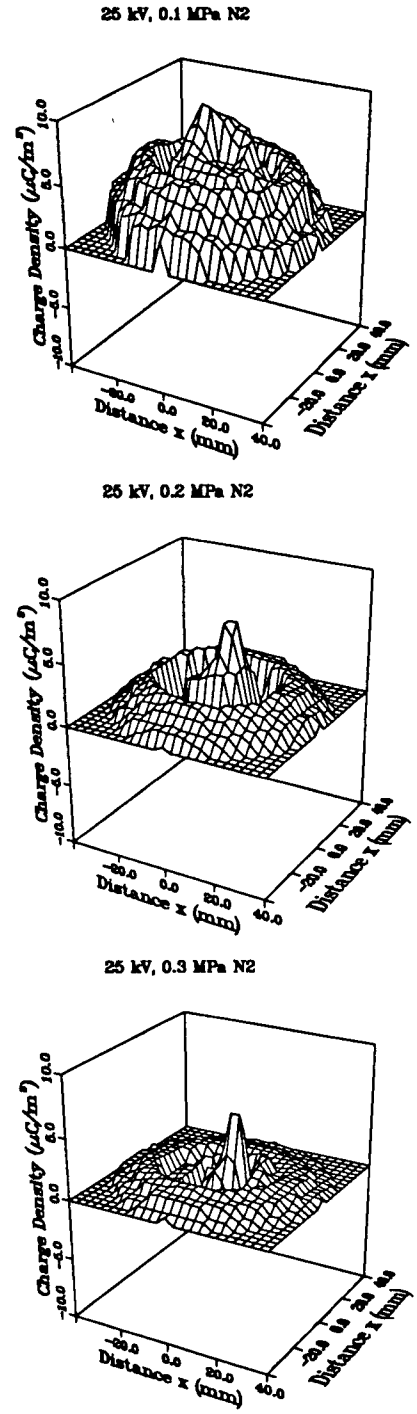

Figure 6.13 Surface charge patterns on nylon spacer surface under 25 kV lightning impulse with 3.2 mm rod diameter in N_2.

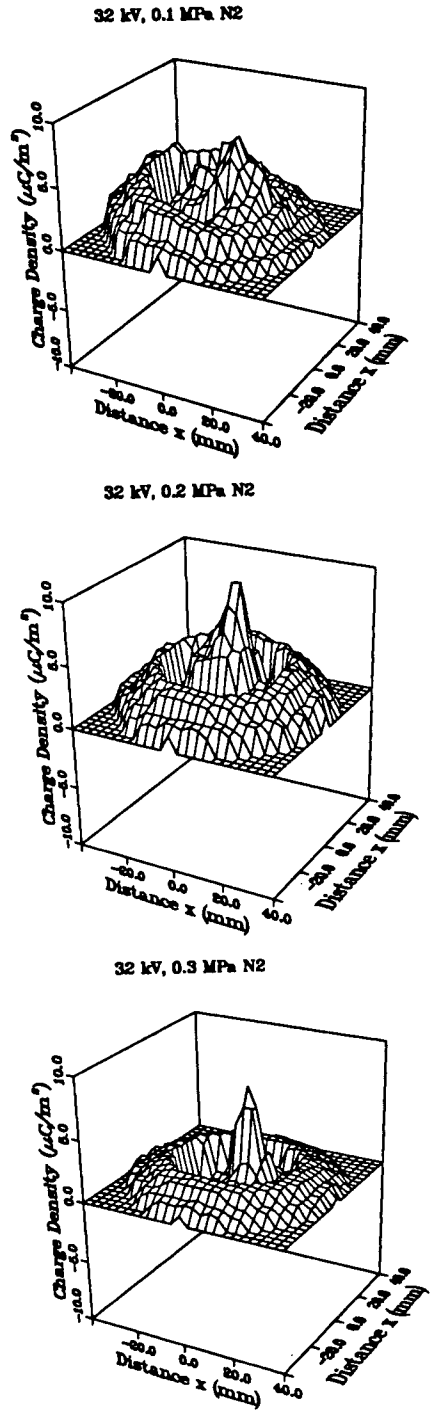

Figure 6.14 Surface charge patterns on nylon spacer surface under 32 kV lightning impulse with 3.2 mm rod diameter in N_2.

excess electron. In the absence of external energy, the ion is capable of existing indefinitely. It may lose the excessive electron when it acquires some energy by random collisions. The lifetime of negative ions is shorter at higher gas pressures where the collision frequency and energy exchanged are high. Also negative ions may lose the excessive electrons by absorbing photon, i.e. photo-detachment. Photons are emitted from these excited states as they drop to the ground state following

$$A^{**} \rightarrow A + h\nu \tag{6.3}$$

and from electron attachment to neutral molecular following

$$A + e \rightarrow A^{-} + h\nu \tag{6.4}$$

Therefore, at a certain voltage detachment probability is higher at higher gas pressure due to shorter negative ion lifetime and more numbers of photons. The electrons released from detachment move with much faster speed than negative ions so that corona discharges and avalanche propagation are enhanced. This may explain that in SF_6 and air surface charge density increases with gas pressure at the voltage much higher than the corona inception voltage.

The probability for radiative attachment in nitrogen is almost zero [78]. There are few negative ions, but free electrons and positive ions due to corona discharges are present. The mean paths of electrons decrease at high gas pressure so that the probability of ionization collision decreases due to small electron kinetic energy

with small mean free paths. Therefore, at same applied voltage, we get less surface charge density at higher gas pressure for nitrogen gas insulated systems.

6.4 Surface charge variation with ambient field near the rod electrode

As discussed before, surface charge accumulation directly relates with corona phenomena. With an applied voltage higher than the corona inception voltage, there is a dramatic increase of surface charges on the spacer surface. In a uniform field, corona inception voltage is the same as breakdown voltage. In a non-uniform field, corona inception voltage is much lower than the breakdown voltage, and the more non-uniform the field is, the lower the corona inception voltage. Therefore, experiments were conducted to see how surface charge patterns change with electric field non-uniformity. In order to get different electric field distribution, different diameter rod electrodes (1.6 mm, 5.0 mm, and 10.0 mm) and different material spacers (nylon and PTFE) were used in the experiments.

Figure 6.15 shows the charge patterns on nylon spacer surface when the rod electrode diameter is 1.6 mm, 5.0 mm, or 10.0 mm. In the experiments, there was no gap between the rod electrode and the spacer, the gas pressure is 0.1 MPa, and the applied voltage is 49 kV lightning impulse. From figure 6.15, we can see that the charge pattern with 1.6 mm diameter rod electrode has much higher magnitude than the charge patterns with 5.0 mm or 10.0 mm diameter rod electrode. The maximum charge magnitudes on the spacer top surfaces are

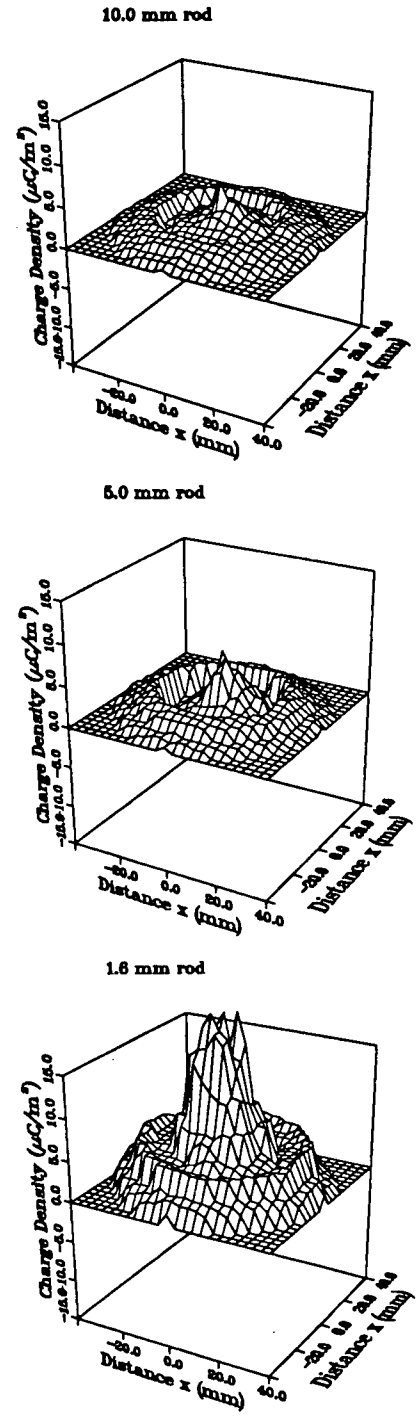

Figure 6.15 Charge patterns on nylon spacer surface with 1.6 mm, 5.0 mm, and 10.0 mm diameter rod electrodes under 49 kV impulse voltage in SF_6 with 0.1 MPa gas pressure.

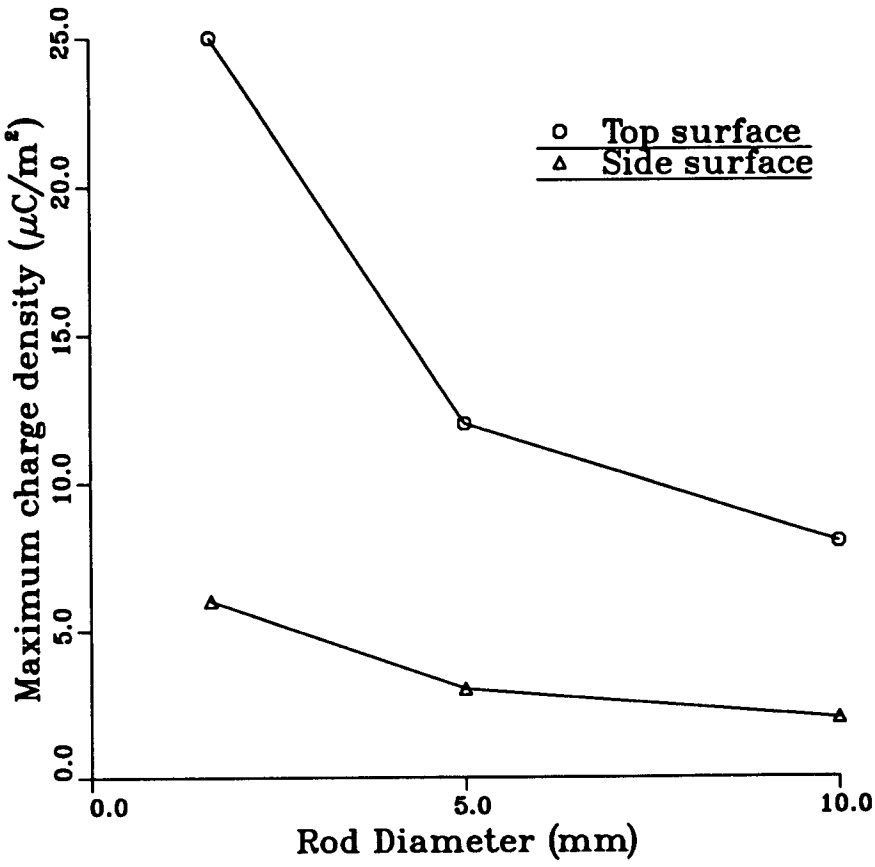

Figure 6.16 Maximum charge density on nylon spacer surface versus rod electrode diameter under 49 kV impulse voltage in SF_6 with 0.1 MPa gas pressure.

25 $\mu C/m^2$ with 1.6 mm rod electrode, 12 $\mu C/m^2$ with 5.0 mm rod electrode, and 8 $\mu C/m^2$ with 10.0 mm rod electrode. The maximum charge magnitudes on the spacer side surfaces are 6 $\mu C/m^2$ with 1.6 mm rod electrode, 3 $\mu C/m^2$ with 5.0 mm rod electrode, and 2 $\mu C/m^2$ with 10.0 mm rod electrode. They are shown in figure 6.16.

The corona inception voltages are 12 kV, 20 kV, and 33 kV for the electrode-spacer geometries with 1.6 mm, 5.0 mm, and 10.0 mm diameter rod electrodes at 0.1 MPa gas pressure. At the same 49 kV lightning impulse applied voltage, there are corona discharges in all three systems. However, the more non-uniform field distribution and the lower corona inception voltage for smaller rod electrodes result in the higher surface charge magnitude, which is shown in figure 6.15.

By using three different diameter rod electrodes, it was confirmed that surface charge magnitudes change with the ambient electric field in the vicinity of the rod electrode.

By using different material spacers, the electric field with high dielectric constant spacer is more non-uniform than the electric fields with low dielectric constant spacer. Experiments were conducted at two lightning impulse voltages namely, 27 kV and 77 kV in 0.1 MPa SF_6 gas with PTFE and nylon spacers. The rod electrode diameter is 3.2 mm and no gap was introduced between the rod electrode and the spacer. Figure 6.17 shows comparative charge density distribution on the top surfaces of nylon and PTFE spacers. It was observed that

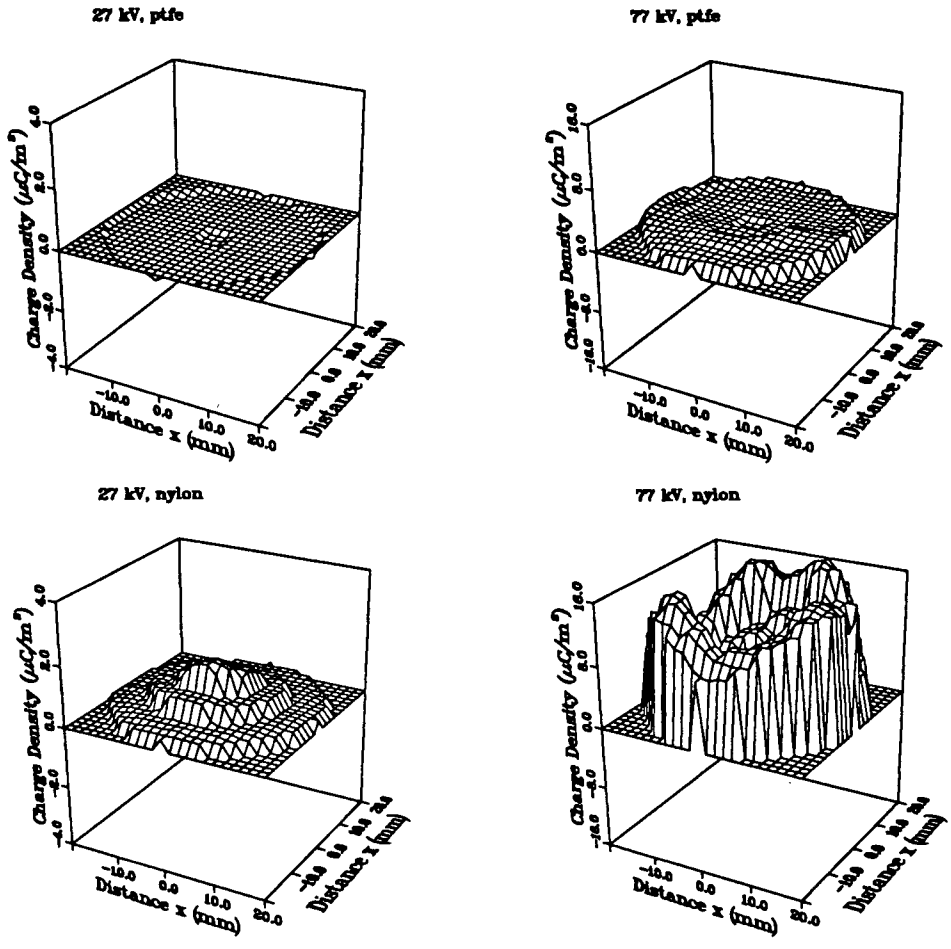

Figure 6.17 Charge patterns on PTFE and nylon spacer top surfaces at 27 kV and 77 kV impulse voltages with 0.1 MPa gas pressure with 3.2 mm rod diameter.

in the case of nylon at a low voltage of 27 kV and a gas pressure of 0.1 MPa there is a concentration of positive charges in the vicinity of the rod electrode, whereas in the case of PTFE the charge polarity continues to remain negative. The charge density is however, low. At 77 kV, the charge polarity is positive on both materials. The difference is that the charge densities on nylon are about 5 times higher as compared to that on PTFE.

The corona inception voltages are, respectively, 14 kV and 17 kV for nylon and PTFE spacer. For nylon and PTFE there appears to be a relatively large difference in charge densities for small difference in the corona inception values. The electric fields on nylon spacer surface ($\varepsilon_r = 3.8$) is more non-uniform than the electric fields on PTFE spacer surface ($\varepsilon_r = 2.1$). This is considered to be one of the reasons that surface charge density on the nylon spacer surface is higher than the surface charge density on the PTFE spacer surface. In addition, the spacer materials may play a role in surface charge accumulation and distribution. Further research is needed to identify the role of the spacer materials in surface charge accumulation.

6.5 Surface charge variation with pre-charging

A GIS system operating at the rated voltage could be stressed with either a switching or a lightning transient under abnormal conditions. It is important to know how charges on solid insulator surfaces in GIS systems accumulate and

change with voltage transients. Flashover may not occur after a transient impulse. However, the surface charges due to the transient impulse may induce a flashover thereafter. Four sets of experiments were carried out to investigate how pre-charging affects subsequent surface charge distributions and magnitudes.

In the first set of experiments, four voltage levels (25 kV, 60 kV, 75 kV, and 98 kV) were applied to a clean PTFE spacer one after another without discharging the spacer between each voltage application. Therefore, 25 kV is the pre-charging voltage for the charges after 60 kV impulse voltage application. 25 kV and 60 kV are the pre-charging voltages for the charges obtained after 75 kV impulse voltage. 25 kV, 60 kV and 75 kV are the pre-charging voltages for the surface charges obtained after 98 kV impulse voltage. In the second set of the experiments, a 98 kV impulse voltage was applied to a clean PTFE spacer without any pre-charging voltage application. In the third set of the experiments, a 60 kV impulse voltage was applied to a clean PTFE spacer without any pre-charging voltage application. In the fourth set of experiments, a 60 kV impulse voltage is applied to a clean PTFE spacer and then followed by a 98 kV impulse voltage without discharge between the two voltage applications. After the 98 kV impulse voltage application, a 60 kV impulse voltage is applied again to the pre-charged insulator. The experimental results are shown in figures 6.18 to 6.20.

Figure 6.18 shows the charge patterns on PTFE spacer surface with 60 kV impulse voltage applications. Figure 6.18 (a) is obtained from the third set of

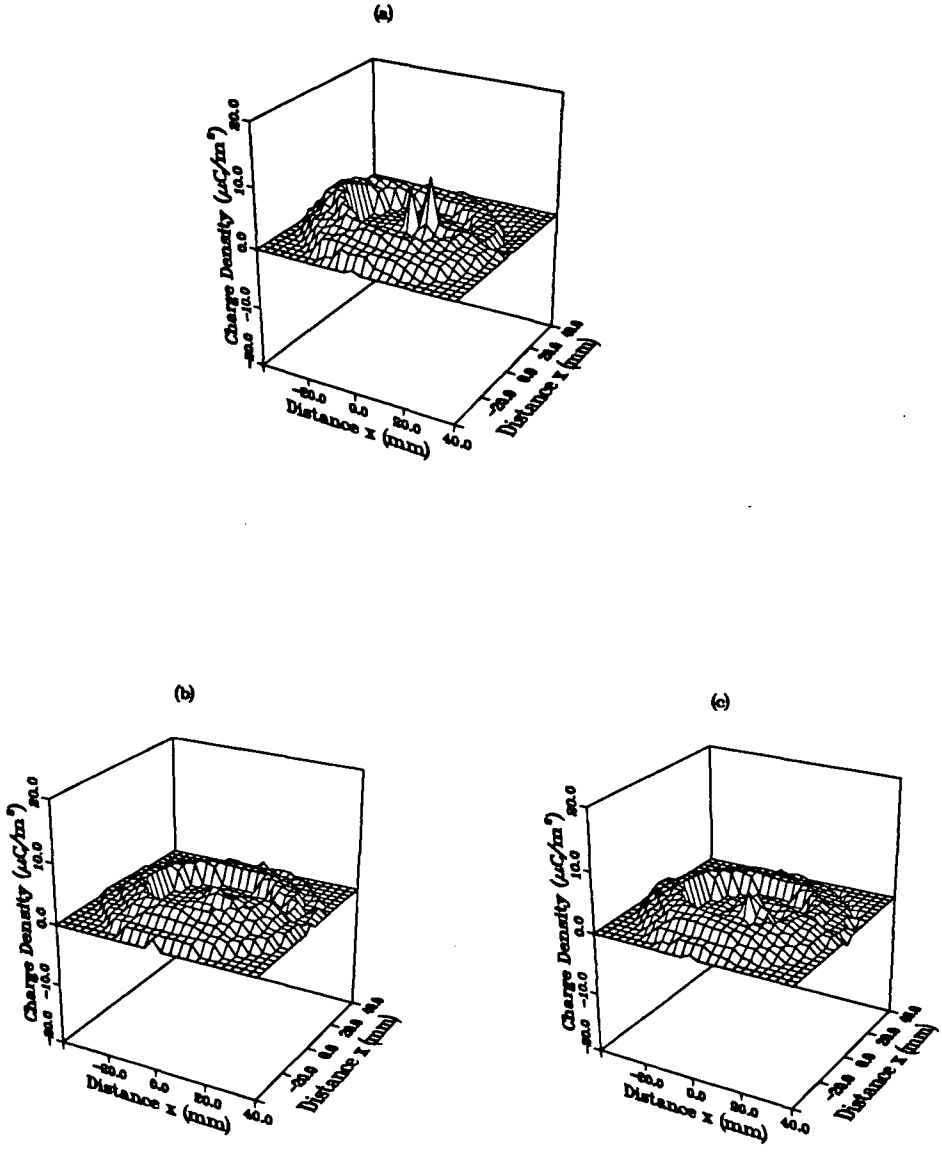

Figure 6.18 The charge patterns after 60 kV impulse voltage applications with 3.2 mm rod diameter in 0.1 MPa SF_6 gas. (a) no pre-charging; (b) and (c) 25 kV impulse pre-charging.

experiment with no pre-charging, i.e. 60 kV impulse voltage is the first voltage applied to the clean PTFE spacer. Figure 6.18 (b) and (c), obtained from the first set of experiments, have 25 kV lightning impulse pre-charging, which show that the charge patterns have very good repeatability. Comparing the top graph with the two on bottom in figure 6.18, we can see that the three graphs are more or less the same. The 25 kV impulse pre-charging has almost no effect on the general surface charge magnitudes and patterns for 60 kV impulse voltage application except for isolated peaks. These peaks may be due to individual surface streamers.

Figure 6.19 shows the charge patterns on PTFE spacer surface after 98 kV impulse voltage applications. Figure 6.19 (a) has no pre-charging, i.e. 98 kV impulse voltage is the first and the only voltage applied to the clean PTFE spacer. Figure 6.19 (b) and (c), obtained from the first set of experiments, have pre-charging twice once each with 25 kV and 60 kV impulse voltages before the 98 kV impulse voltage application. The three graphs are quite similar. The pre-charging by 25 kV and 60 kV have no visible or significant effect on the charge patterns with 98 kV impulse voltage application. Again, there are large isolated charge peaks, perhaps due to individual surface streamers.

Figure 6.20 shows the results obtained from the fourth set of experiments. A 60 kV impulse voltage was applied to a clean PTFE spacer, and the surface charge pattern is shown in figure 6.20 (a). Then, a 98 kV impulse voltage is applied to the same spacer without discharging the charges due to the previous

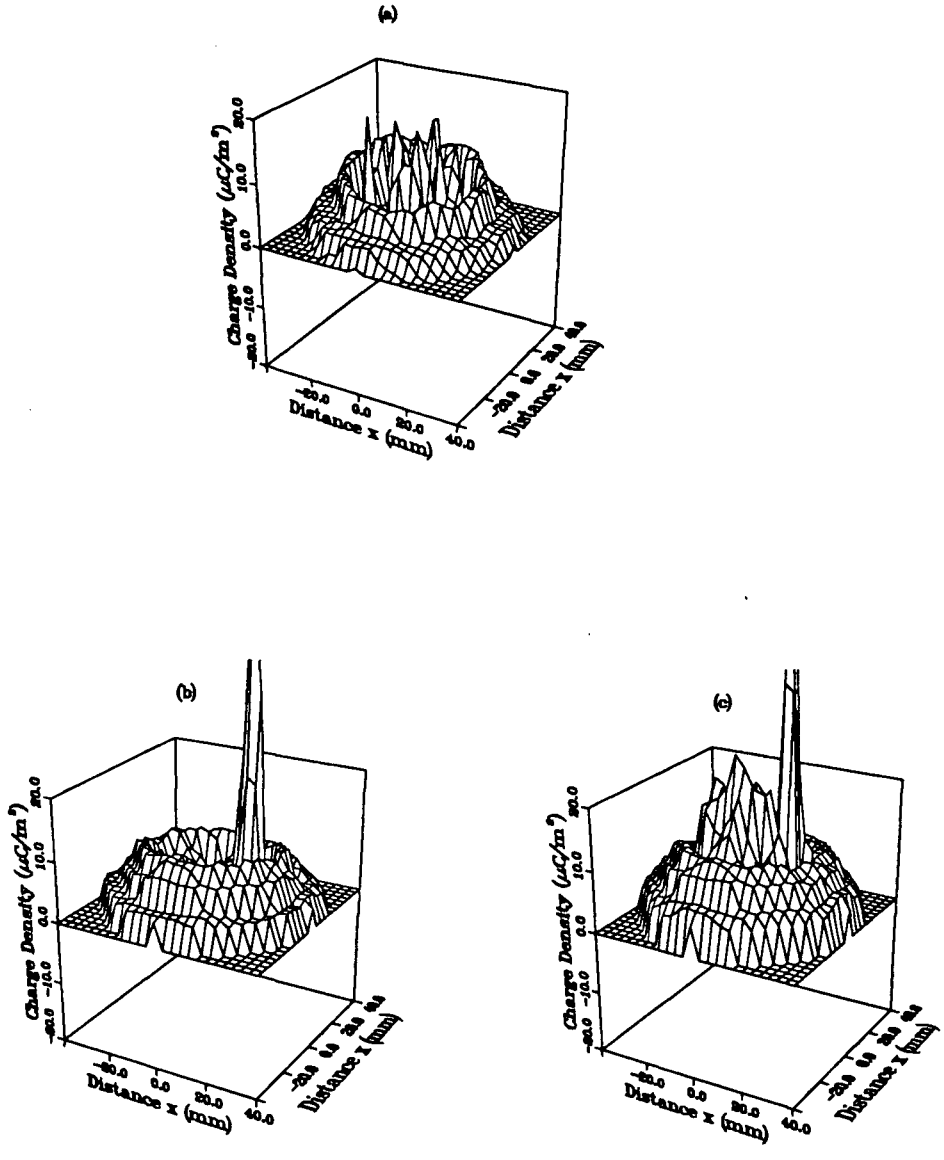

Figure 6.19 The charge patterns after 98 kV impulse voltage applications with 3.2 mm rod diameter in 0.1 MPa SF_6 gas. (a) no pre-charging; (b) 25 kV impulse voltage pre-charging; (c) 60 kV impulse voltage pre-charging.

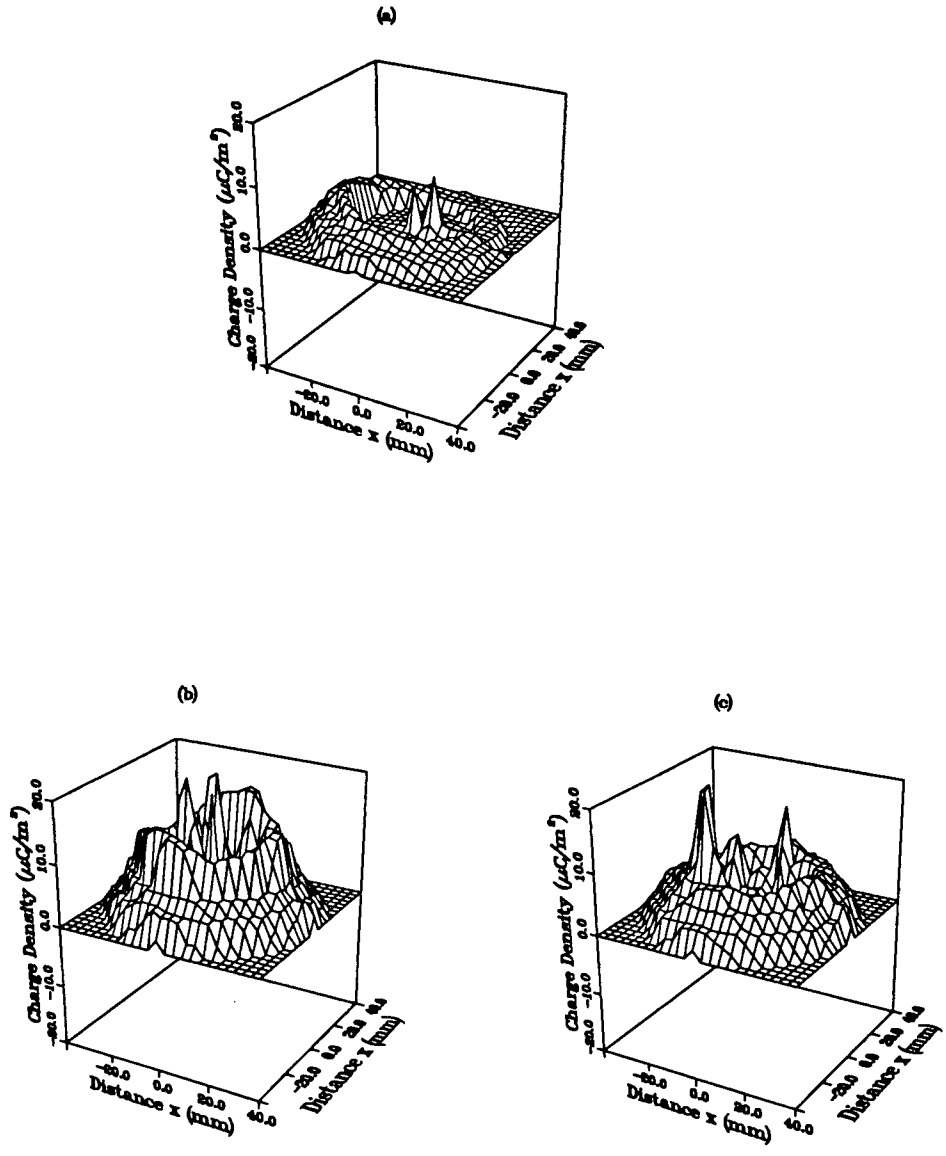

Figure 6.20 The charge patterns corresponding to sequence voltage applications (60 kV, 98 kV, and 60 kV impulse voltages) with 3.2 mm rod diameter at 0.1 MPa SF_6 gas.

voltage application. The surface charge pattern is shown in figure 6.20 (b). Figure 6.20 (c) is obtained after a 60 kV impulse voltage application with first the 60 kV and second the 98 kV impulse voltage pre-charging. The first graph on the top is the same as the ones shown in figure 6.18 and the graph on the bottom left is similar to the ones shown in figure 6.19. The graph on the bottom right obtained after 60 kV impulse with 60 kV and 98 kV pre-charging has much higher charge magnitude than the first graph on the top which has no pre-charging and the graphs in figure 6.18 with 25 kV pre-charging. This is due to the 98 kV impulse voltage application. The charge pattern after a 60 kV voltage application with 60 kV and 98 kV pre-charging is similar with the charge pattern after a 98 kV voltage application with only 60 kV pre-charging , except on the edge of the PTFE spacer top surface.

During pre-charging, a dynamic stable charge pattern is established on the spacer surface, which is directly related with the electric field between electrode and the spacer surface. If a voltage, which is higher than the pre-charging, is applied to the same spacer, the dynamic stable situation of the surface charges may be changed due to the higher electric field intensity between the electrode and the spacer surface. Therefore, more charges will be accumulated on the spacer surface due to corona, gas conduction and surface condition. If a voltage, which is lower than the pre-charging voltage, is applied to the same spacer, the dynamic stable situation of the surface charges due to the pre-charging may remain the same

because no significant corona or gas conduction is likely due to the weaker ambient electric field intensity. The surface charges may, however, slightly redistribute on the surface during the applied voltage due to local discharges.

The experimental results show that:

- the charge pattern at a certain voltage with pre-charging will be similar to the charge pattern at the same voltage without pre-charging if the voltage applied has higher magnitude than the pre-charging voltage.
- the charge pattern at a certain applied voltage with pre-charging will be similar to the pre-charging charge pattern if the applied voltage has lower magnitude than the pre-charging voltage.

6.6 Comparison of surface charging under impulse and DC voltages

In order to study the effect of the duration of applied voltage on surface charging, standard lightning impulses and DC for 5 minutes or 30 minutes were used as applied voltages. Figure 6.21 shows the charge patterns with a DC voltage and a lightning impulse ($1.2/50\mu s$) at 40 kV in SF_6 gas, both with positive polarity. In this experiment, a 4 mm gap was introduced between the rod electrode and the top surface of the spacer. Following a 40 kV lightning impulse voltage application, the positive charges can only be observed at the center of the top spacer surface; low magnitude, negative polarity charges still remain on

the rest of the surface. Also, no significant changes were observed among the results after 1, 5, and 20 applications of the impulse voltage. Very high surface charge densities were observed on the spacer surface after 5 minutes at 40 kV DC voltage application.

The mobility of the ions in SF_6 is 0.6 cm^2/Vs [79]. The time for ions to drift from the rod electrode to the spacer surface is longer than 7 μs, which is calculated by assuming that the field between the rod electrode and the spacer is uniform. With a lightning impulse voltage application, 40 kV is only the peak value and the duration of the voltage higher than the inception voltage is much shorter than 50 μs. Therefore, only the ions on the tip of the rod electrode, which are in highest electric field and have the shortest distance to travel, may move along the axis to deposit on the center of the surface. With 5 minutes DC voltage application, not only most of the positive ions around the rod electrode have enough time to travel across the gap along the electric field direction and deposit on the spacer surface, but also at the same time, corona charging continues so that surface charges increase with the time.

Experiments with 30 minutes at 40 kV DC voltage application were also conducted. The results show that there is not much difference in the results between 5 minutes and 30 minutes DC voltage applications. This may indicate that once there are positive ions deposited on the spacer surface, the electric field due to these surface charges reduces the overall electric field, and may

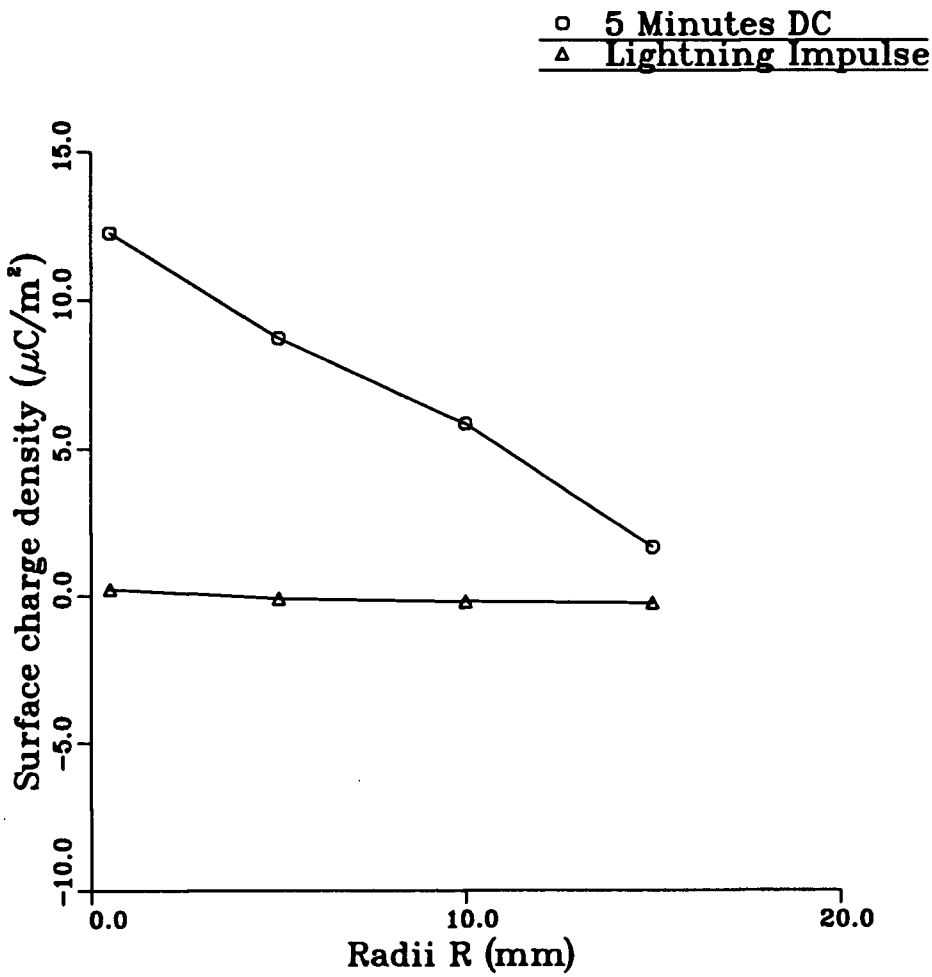

Figure 6.21 Charge patterns on nylon spacer top surface with 4 mm gap between the 1.6 mm diameter rod electrode and the spacer top surface after 40 kV voltage applications in SF_6 gas.

finally extinguish or inhibit the corona around the rod electrode. This leads to a saturation level of deposited charge for a given applied voltage.

It is conceivable that there is a period of time longer than that of a lightning impulse and shorter than 5 minutes, over which the charge density gradually builds up to a saturation level. The experiments conducted so far do not permit an accurate estimation of the duration of this transient period.

Figure 6.22 shows the charge patterns in different gases, namely air and SF_6, on nylon spacer with 4 mm gap between 1.6 mm diameter rod electrode and spacer top surface after 5 minutes of positive DC voltage application. In SF_6, at 20 kV DC voltage the residual surface charges have low magnitude and are of negative polarity. When the voltage is increased to 40 kV, the surface charges have a higher magnitude and are of positive polarity, which is the same as the polarity of the applied voltage. In air, at 5 kV DC voltage no measurable charge is deposited on the surface. At 10 kV, the surface charges have the same polarity as the applied voltage and have significant magnitude.

The calculated corona inception voltages are about 12 kV and 15 kV for the electrode-spacer geometry in air and SF_6 respectively. In air, deposited charges were observed at a low voltage of 10 kV due to lower corona inception voltage. In SF_6 gas, deposited charge become significant at about 20 kV due to the higher corona inception voltage

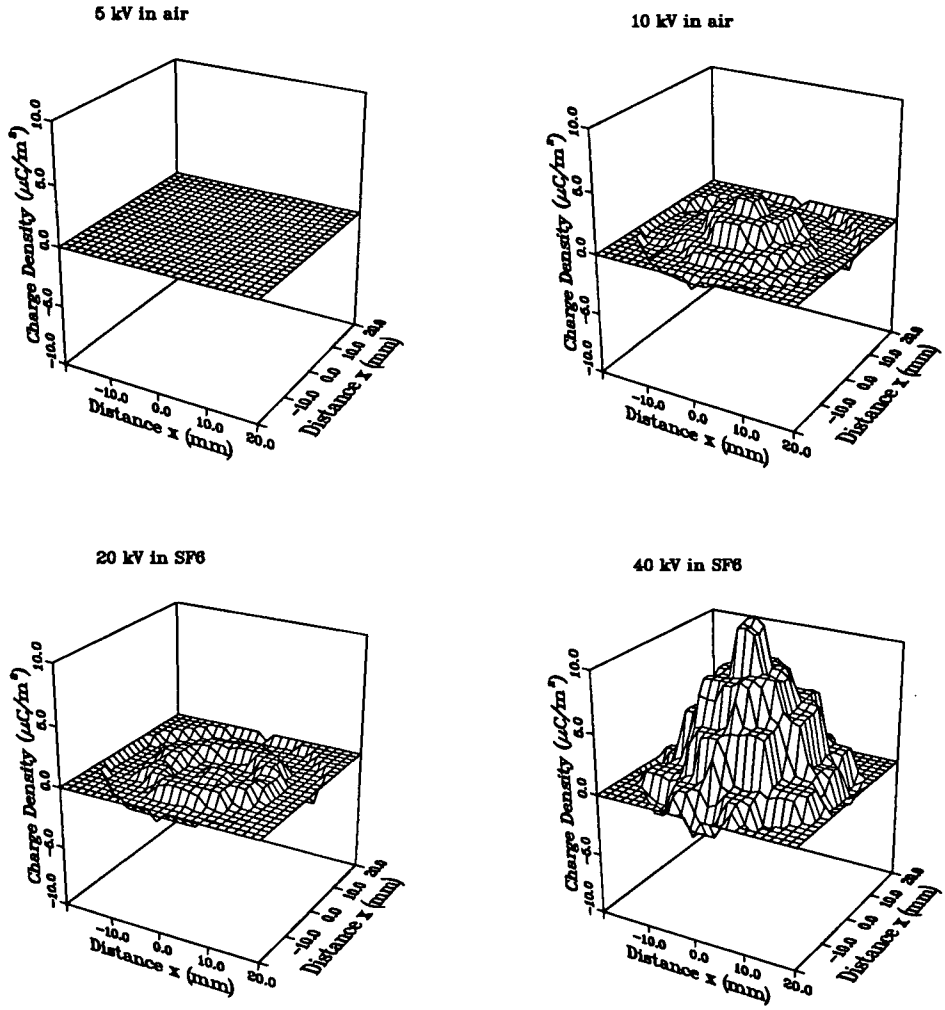

Figure 6.22 Charge patterns on the nylon spacer top surface with 4 mm gap between spacer top surface and 1.6 mm diameter rod electrode at 0.1 MPa gas pressure after applying 5 minutes DC voltages.

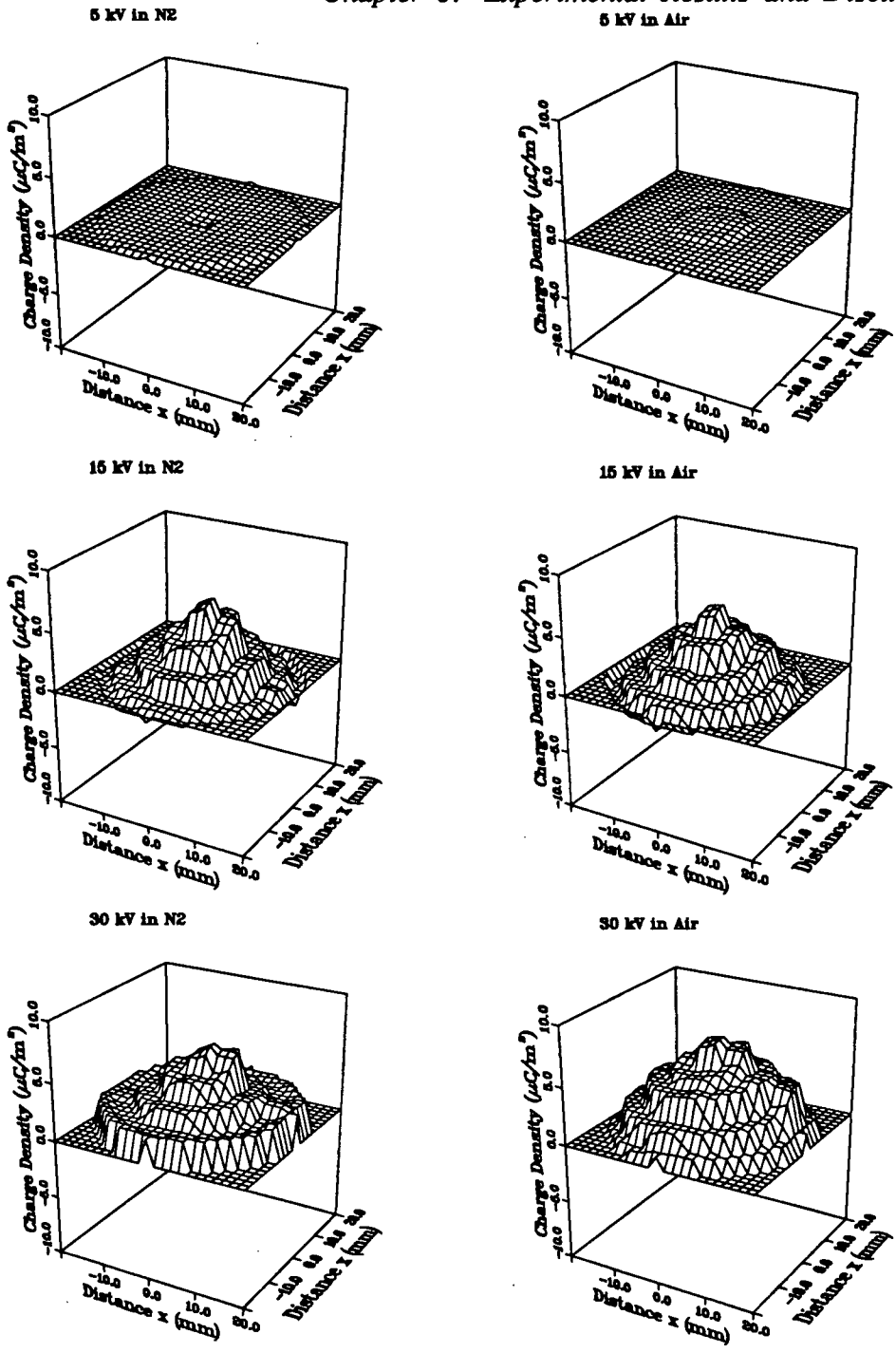

Figure 6.23 Charge patterns in N_2 and air on nylon spacer top surface under 5 minutes DC voltage with 3.2 mm diameter rod electrode.

For comparison, experiments were also performed with non-attaching nitrogen gas. Figure 6.23 shows the charge patterns in nitrogen compared with the charge patterns in air under the same experimental conditions. We see that the charge distribution and magnitude in the two gases are very similar. The ionization field for nitrogen gas is about 32.2 kV/cm, which is very close to the ionization field of air, 30 kV/cm. The calculated corona inception voltages are 12 kV and 13 kV for air and nitrogen respectively. Although air is a slightly electronegative gas, no significant effect on the surface charge magnitude or distribution was noticed.

Figure 6.24 shows the charge pattern in nitrogen as compared to the charge pattern in SF_6 gas. The corona inception voltages are 13 kV and 15 kV for nitrogen and SF_6 respectively. From figure 6.24, it can be seen that the charge magnitude with nitrogen at 15 kV, which is 2 kV higher than its corona inception, is much higher than the charge magnitude with SF_6 gas at 20 kV, which is 5 kV higher than its corona inception voltage.

The main reasons for the different charge patterns are the ionization fields of the gases and the electronegative characteristic of SF_6 gas. In a very non-uniform electric field, especially under DC voltage applications, corona-stabilization is present in SF_6 due to its strong electron-negative characteristics. With electronegative gases, the free electrons caused by corona may attach themselves to neutral atoms or molecules so that negative ions are formed. A cloud of negative ions collects very close to the positive rod electrode as shown in figure 6.25, thus

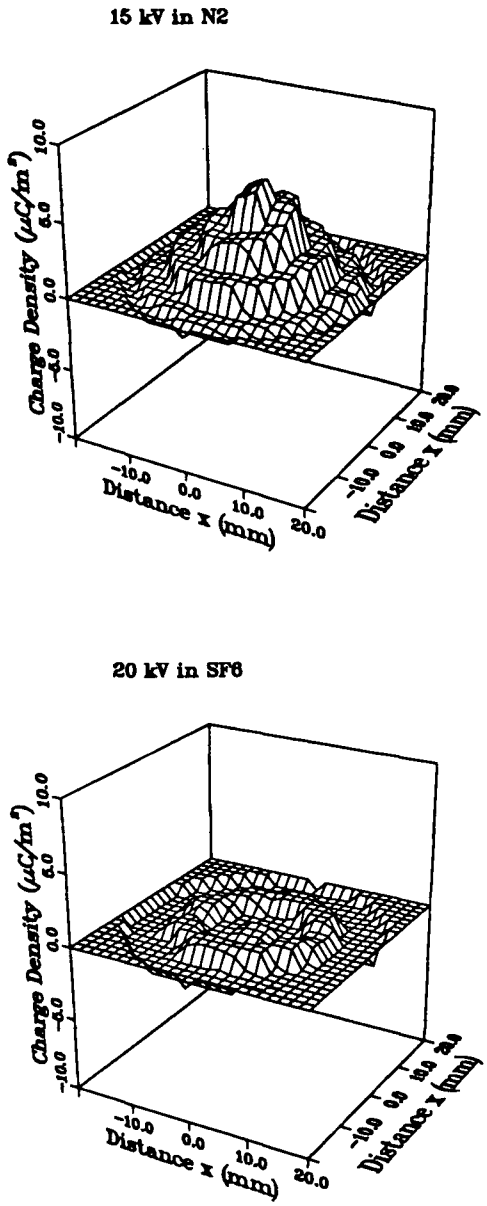

Figure 6.24 Charge patterns in N_2 and SF_6 on nylon spacer top surface under 5 minutes DC voltage with 3.2 mm diameter rod electrode.

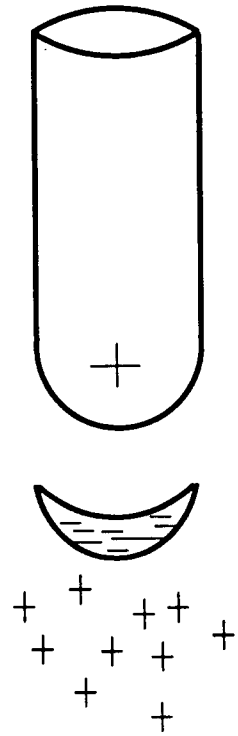

Figure 6.25 Negative ions around anode due to electron attachment in SF_6.

increasing the field near the rod electrode. This may increase corona activity near the rod tip and neutralize the space charges. The field in the space between the negative ion cloud and the ground electrode decreases thus suppressing corona avalanches and reducing the deposited charge. This may cause surface charges in SF_6 found only at higher voltage levels. The electric field between positive ions and the rod electrode decreases so that the velocity of positive ions moving towards the spacer surface decreases, thus inhibiting the progress of streamers towards the other electrode. Therefore, less charges accumulate on the spacer surface in SF_6 gas.

Figure 6.26 shows the charge distributions on nylon spacer top surface in air and SF_6 respectively after applying 40 kV positive DC voltage for 5 minutes. It is observed that the charge pattern in SF_6 is concentrated at the center of the surface, while charge pattern in air is distributed all over the surface, i.e. the charge pattern in air was more uniform than the charge pattern in SF_6.

The electric field along the rod electrode surface is calculated by a charge simulation method (CSM) and shown in figure 6.27. The electric field normal to the rod electrode surface increases along surface towards the axis. Because the ionization field in air ($\sim$ 30 kV/cm) is much lower than that ($\sim$ 89 kV/cm) in SF_6, the place having electric field of 89 kV/cm is much closer to the axis than the place having electric field of 30 kV/cm. Since the avalanches develop along

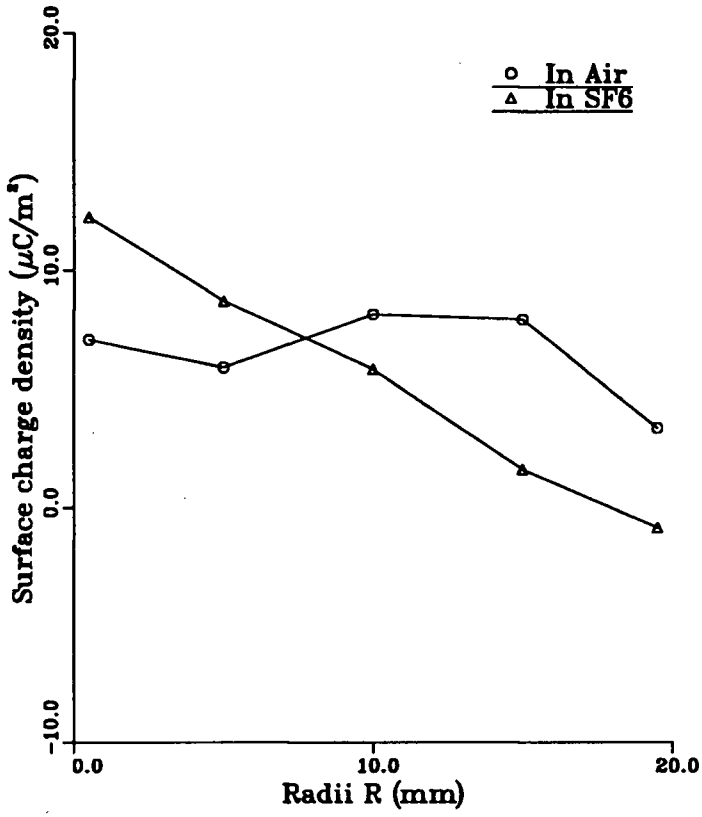

Figure 6.26 Charge patterns on the nylon spacer top surface with 4 mm gap between 1.6 mm diameter rod electrode and spacer after 40 kV positive DC voltage for 5 minutes at 0.1 MPa gas pressure.

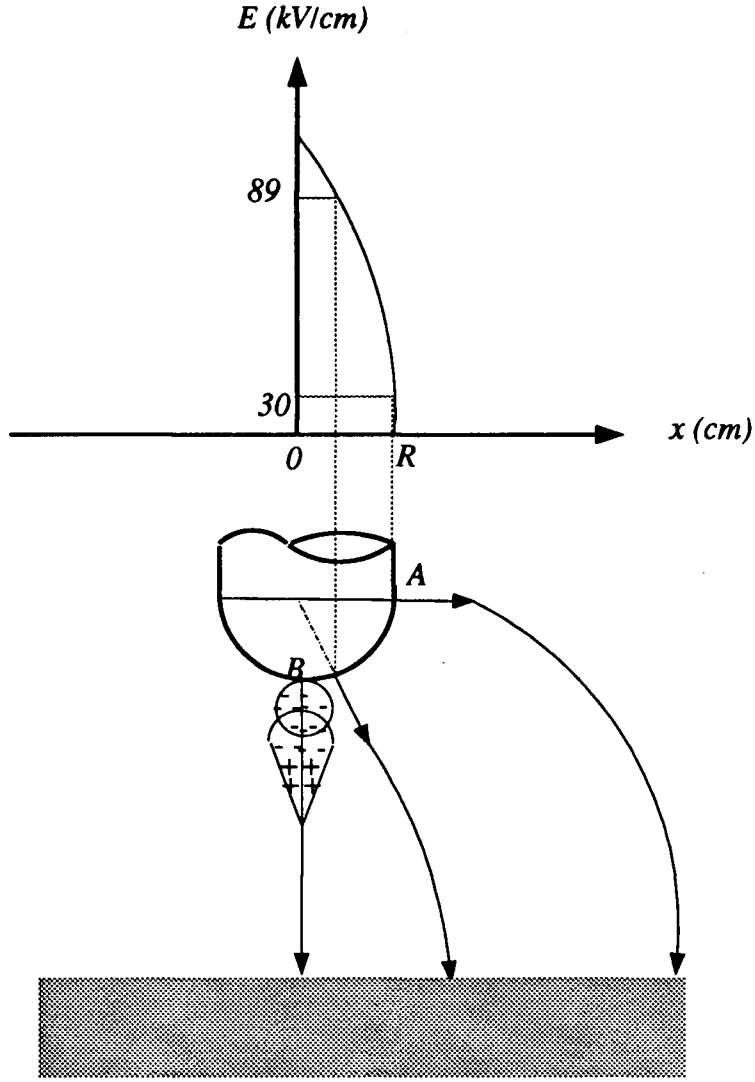

Figure 6.27 The electric field on the rod electrode surface with 4 mm gap at 9 kV and avalanche development in the space between the rod electrode and the spacer surface.

electric field lines, the deposited charges on the spacer top surface are spread over a larger area in air than in SF_6.

The surface charges measured on a spacer surface were employed for electric field computations by SSM program to study the effect of surface charges on total electric field and surface flashover. All the calculations and discussions are presented in Chapter 7.

Chapter 7

Field Calculations and Surface Flashover

7.1 Introduction

Surface flashover along a gas/solid interface is an important limiting factor for the withstand voltage and reliability of compressed-gas-insulated equipment. The flashover process may be viewed as a two-step event: initiation and propagation across the entire gap. The initiation results from a local field perturbation of sufficient size. Propagation is expected when sufficient electric field exists along the propagation path. For the initiation model, which has been well developed [56], the discharge initiation is expected when a local field exceeds the ionization field, which is 89 kV/cm for SF_6 at 0.1 MPa, and the avalanche grows to 10^8 electrons within the ionization zone. The propagation models are presently under investigation and they are not yet well developed. Surface flashover exhibits a strong sensitivity to field perturbations at or near the surface. Perturbations may arise for a variety of reasons, but in each case they may be interpreted as causing a disturbance in the electric field distribution. The disturbance introduces a local field enhancement which causes local ionization and when sufficient, triggers

flashover. There are four different types of perturbations which influence surface flashover [55]. They are:

- triple junction;
- conducting particulate;
- charges;
- irregular dielectric surface.

In this research, we concentrate on studying the effect of surface charges on surface flashover. Interesting results were obtained.

Cooke [55] studied static charges and surface discharges. In his studies, a 1 m long spacer was charged and by suddenly applying a ground electrode locally at one end, a discharge would propagate along the 1 m length. This study showed that even surface charges alone, with no applied voltage, can provide sufficient conditions to propagate an extended flashover, i.e. the static charges can enhance discharge propagation and in the limit, can even cause flashover when the end-to-end voltage is zero. In these systems, discharge propagation occurs when the charge density exceeds a critical value and the propagation velocity increases as the charge density increases. The surface flashover in compressed gases appears to be mainly a field-driven process. The necessary ambient field for propagation along a surface appears to be rather small, even below 10 kV/cm in SF_6 at 780 kPa.

Niemeyer and Pinnekamp [80] derived a simplified model of discharge propagation on insulator surface. The model relates the discharge characteristics such as leader onset voltage, maximum leader length, leader propagation velocity, and average leader field strength, to the discharge parameters such as pressure, voltage, geometry, and polarity. In the leader channel of an ionization zone, the electric field is critical and thus able to produce conduction electrons by electron impact ionization. For SF_6 such a critical conduction mechanism is consistent with the observed experimental field strength of the order of a few kV/cm.

In this research, the total electric field, which is surface charge field and applied field, is calculated and analyzed. A surface charge simulation program (SSM) was developed for the calculation. The model used in the calculations is the rod-plane electrode geometry with a cylindrical insulating spacer in between as shown in figure 4.1. The boundaries at the electrodes and the interfaces between the dielectrics are divided into small elements as shown in figure 7.1. The top surface of the spacer was divided into ten parts in the circumferential direction and four parts in the radial direction. Therefore, the areas of the elements on the top surface are between 8.0 mm^2 and 55 mm^2. The side surface of the cylindrical spacer was divided into five parts vertically and ten parts circumstantially. Therefore, the areas of elements on the side surface are 75 mm^2. The element areas were 0.53 mm^2 on rod electrode surface and between 5.0 mm^2 and 0.45 mm^2 on the plane electrode surface.

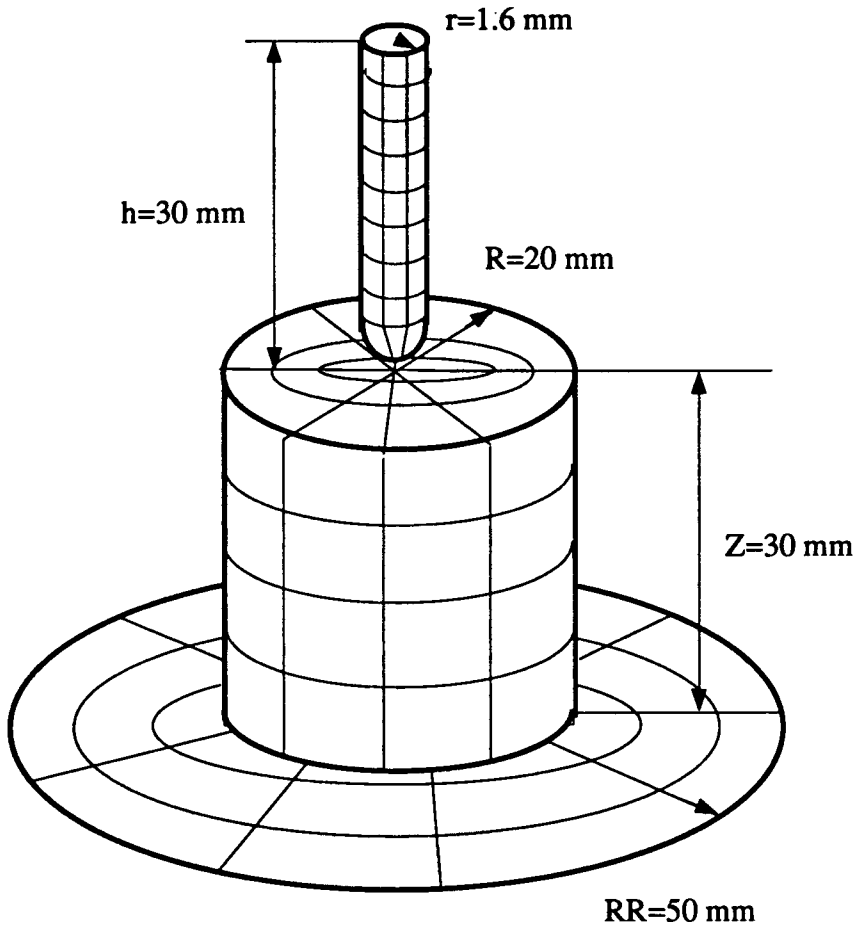

Figure 7.1 The rod-plane electrode and cylindrical insulator model.

7.2 Field distribution analysis

The surface charges used here are from the measurements on nylon spacer surface with a 3.2 mm diameter rod electrode, no gap between the rod electrode and the spacer, in 0.3 MPa SF_6 gas, as an example. The total electric fields and potentials on the spacer surface were calculated by the SSM program. In order to have visible images, color graphs are employed to display surface charge, total electric field, and surface potential distributions. The red color represents high magnitude and the blue color represents low magnitude.

Figure 7.2 shows the surface charge distributions on the nylon spacer surface at 27 kV, 50 kV, and 77 kV impulse voltage. A sketch is shown in figure 7.3 to indicate for the color graphs that the round surface corresponds to the top surface of a spacer and the rectangular surface is the cylindrical spacer side surface spread out. The highest value the red color represents is 1 $\mu C/m^2$ for figure 7.2 (a) and 21 $\mu C/m^2$ for figure 7.2 (b) and (c). The lowest value the blue color represents is – 0.16 $\mu C/m^2$ for figure 7.2 (a) and 0 $\mu C/m^2$ for figure 7.2 (b) and (c). It can be seen that at 27 kV, there are very few charges on the entire surface. Surface charges accumulate on some local areas at 50 kV and then extend to most of the surface when voltage increases to 77 kV. At 77 kV, the surface charge density is much higher than that at lower voltage levels.

Figures 7.4-7.6 show the total surface electric fields with and without surface

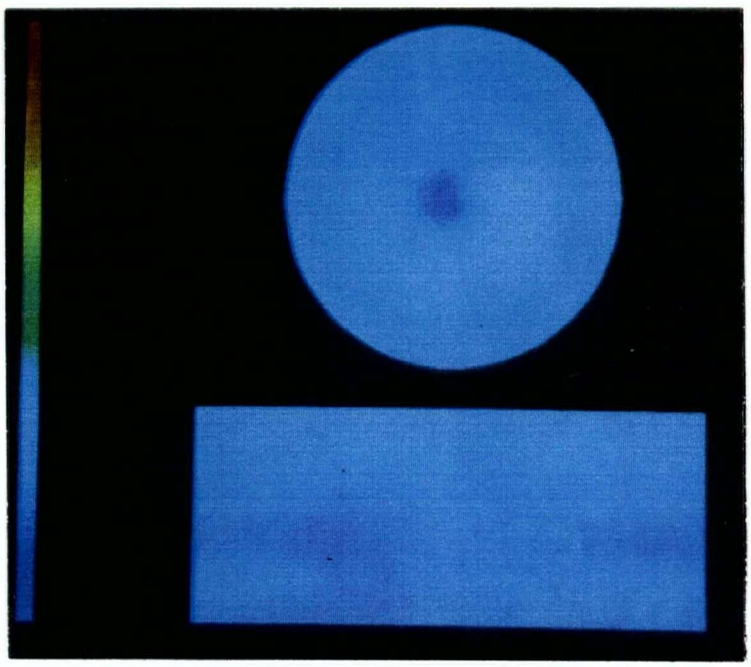

(a) 27 kV

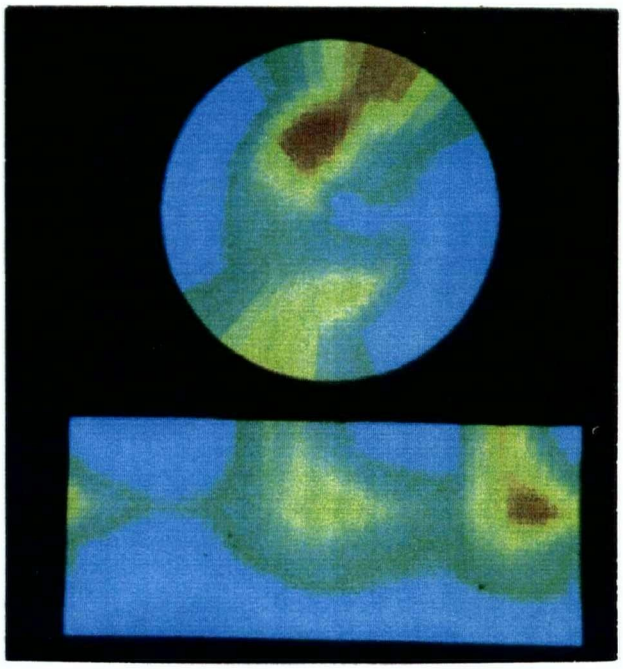

(b) 51 kV

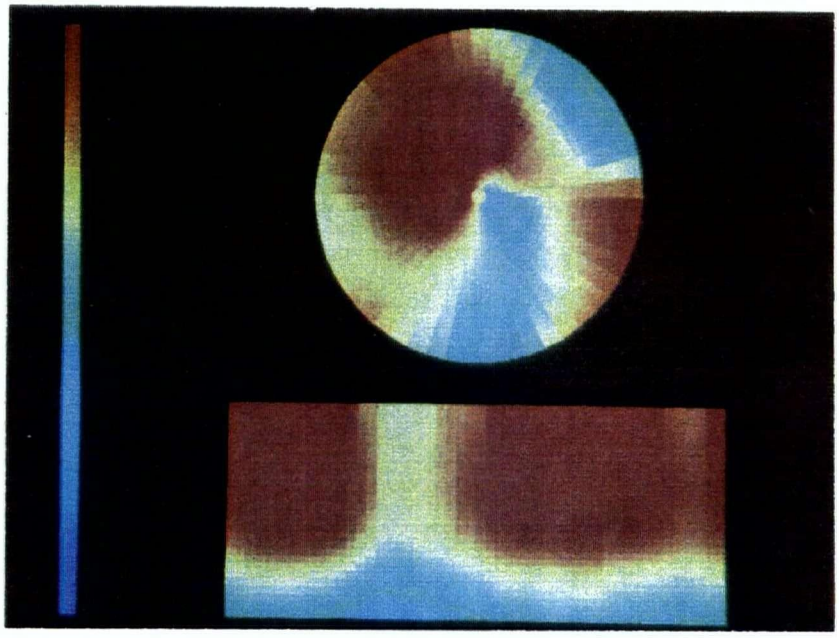

(c) 77 kV

Figure 7.2 Surface charge distributions on nylon spacer surface in 0.3 MPa SF_6 gas with 3.2 mm diameter rod electrode and no gap between rod electrode and spacer.

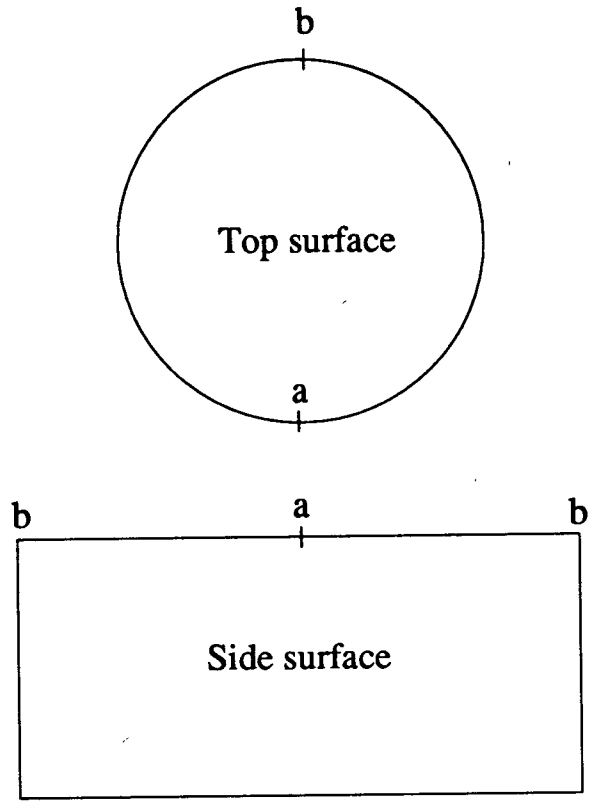

Figure 7.3 A sketch of spacer top and side surfaces for color graphs.

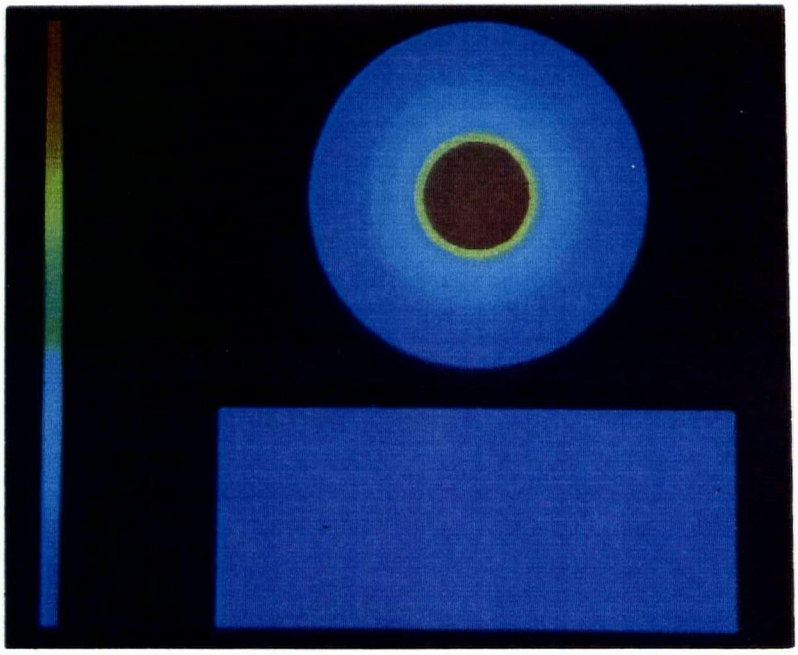

(a) Without surface charges.

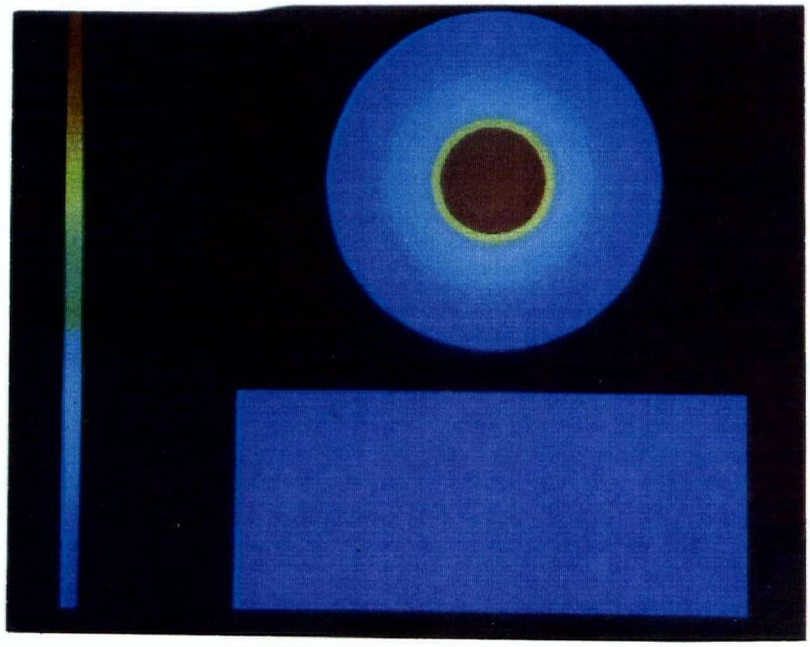

(b) With surface charges.

Figure 7.4 Magnitude of the total field at various positions on the nylon spacer surface at 27 kV in 0.3 MPa SF_6 gas with 3.2 mm diameter rod electrode and no gap between rod electrode and spacer.

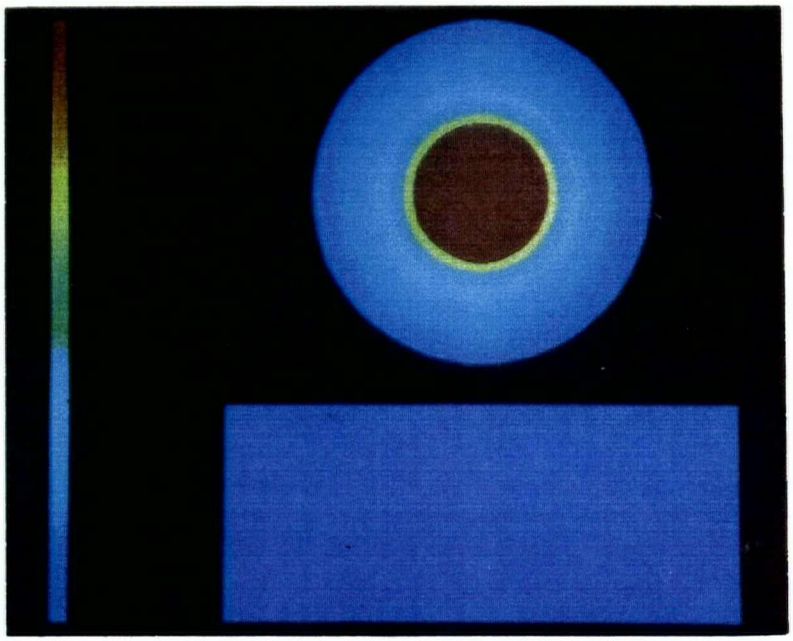

(a) Without surface charges.

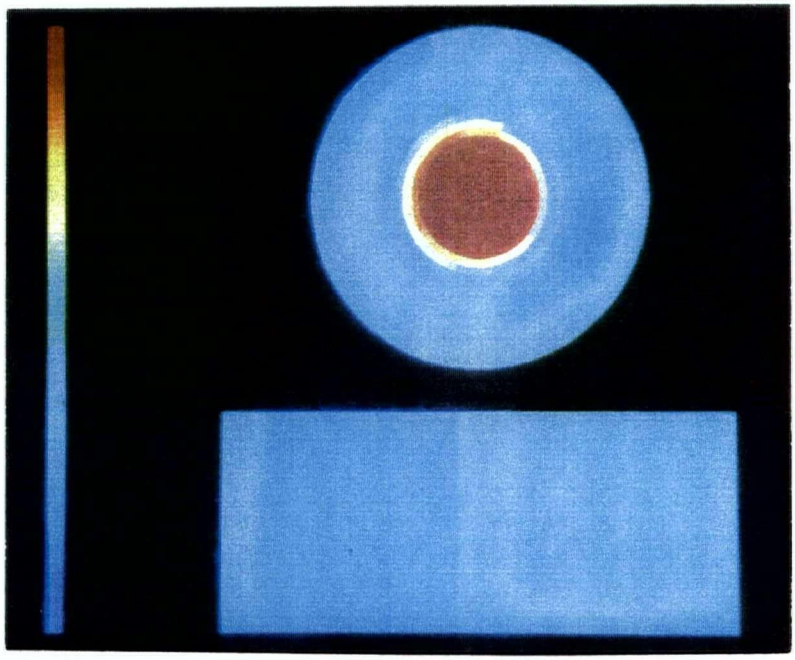

(b) With surface charges.

Figure 7.5 Magnitude of the total field at various positions on the nylon spacer surface at 50 kV in 0.3 MPa SF_6 gas with 3.2 mm diameter rod electrode and no gap between rod electrode and spacer.

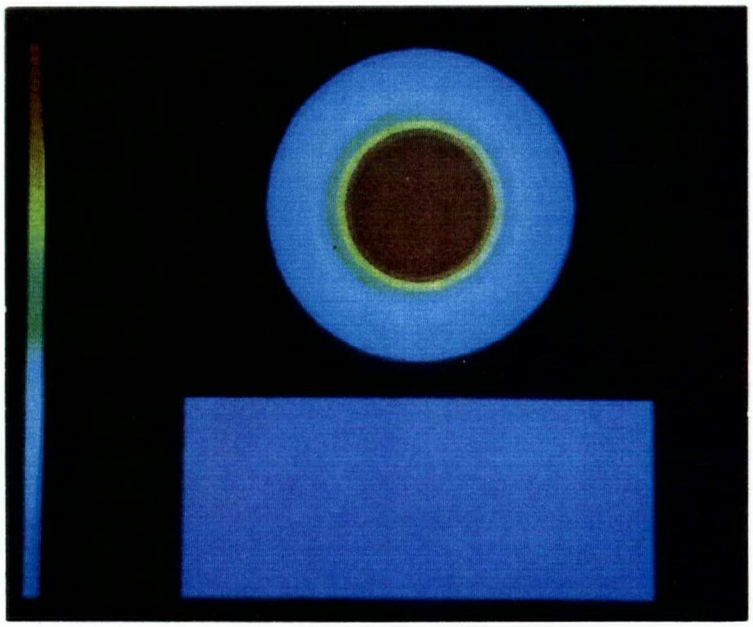

(a) Without surface charges.

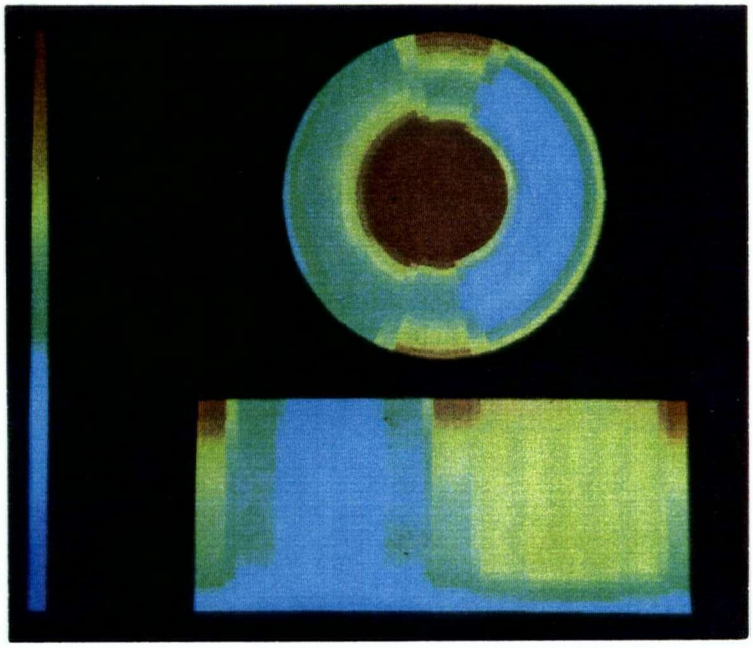

(b) With surface charges.

Figure 7.6 Magnitude of the total field at various positions on the nylon spacer surface at 77 kV in 0.3 MPa SF_6 gas with 3.2 mm diameter rod electrode and no gap between rod electrode and spacer.

charges present at 27 kV, 50 kV and 77 kV impulse voltages. At 27 kV, due to very few surface charges on the spacer surface, the total electric field with surface charges is almost the same as the field without surface charges as shown in figure 7.4 (a) and (b). At 50 kV, there are some charges accumulated on the spacer surface as shown in figure 7.2 (b). The total electric fields on most of the surface increase due to the effect of the surface charges, as shown in figure 7.5. The color changes from dark blue, representing lower value, to light blue, representing higher value. The total electric fields on the center of the top surface seem to be going down a little bit since the color changes from dark red to light red. At 77 kV, the total electric fields change significantly as shown in figure 7.6. Tremendous changes are found on the side surface and the edge of top surface (figure 7.6 (b)). Figures 7.7-7.9 show the changes of the surface potential distributions due to the effect of surface charges.

7.3 Electric field with surface charges by same-polarity pre-charging

The surface charges used for the field calculations were measured on a PTFE spacer surface after lightning impulse voltage applications. The medium is compressed SF_6 gas at 0.3 MPa pressure. The rod electrode diameter is 3.2 mm, with no gap between the rod electrode and the spacer. The resulting total electric fields, applied field and surface charge field due to same-polarity pre-charging,

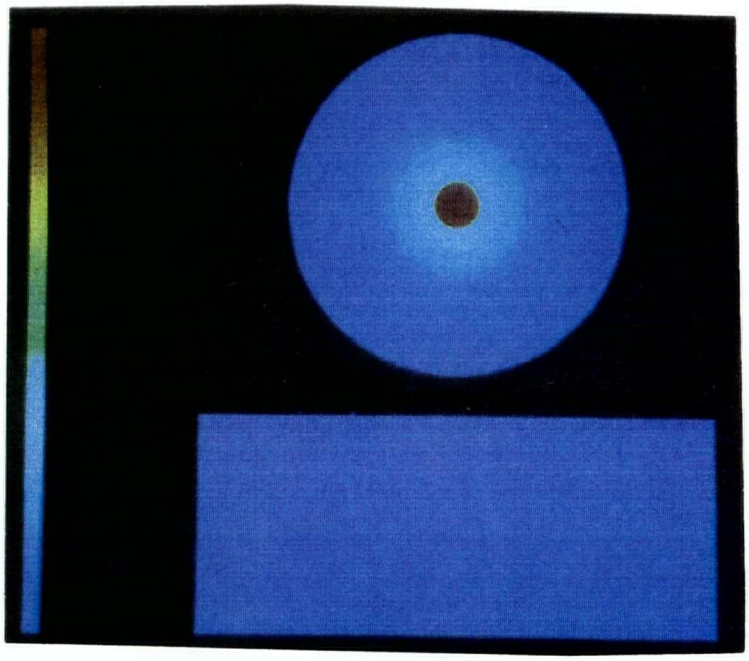

(a) Without surface charges.

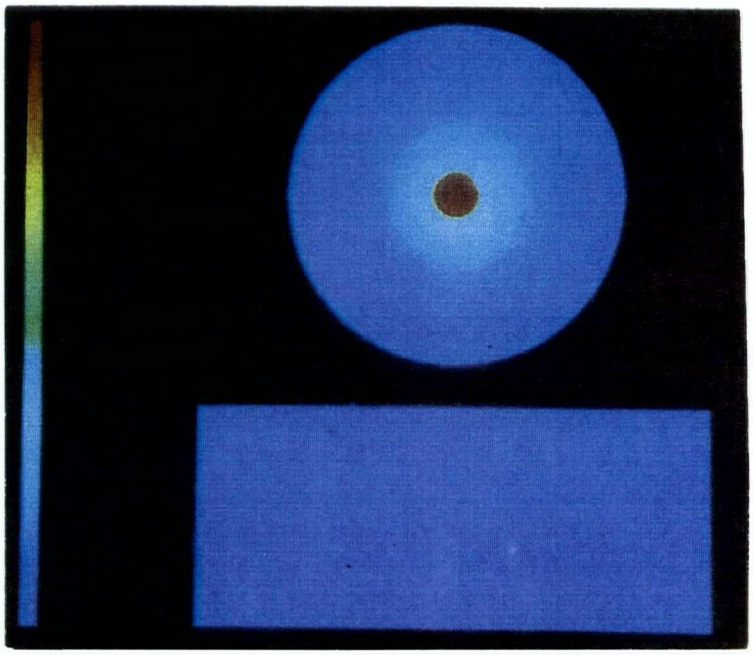

(b) With surface charges.

Figure 7.7 Surface potentials at 27 kV on nylon spacer surface in 0.3 MPa SF_6 gas with 3.2 mm diameter rod electrode and no gap between rod electrode and spacer.

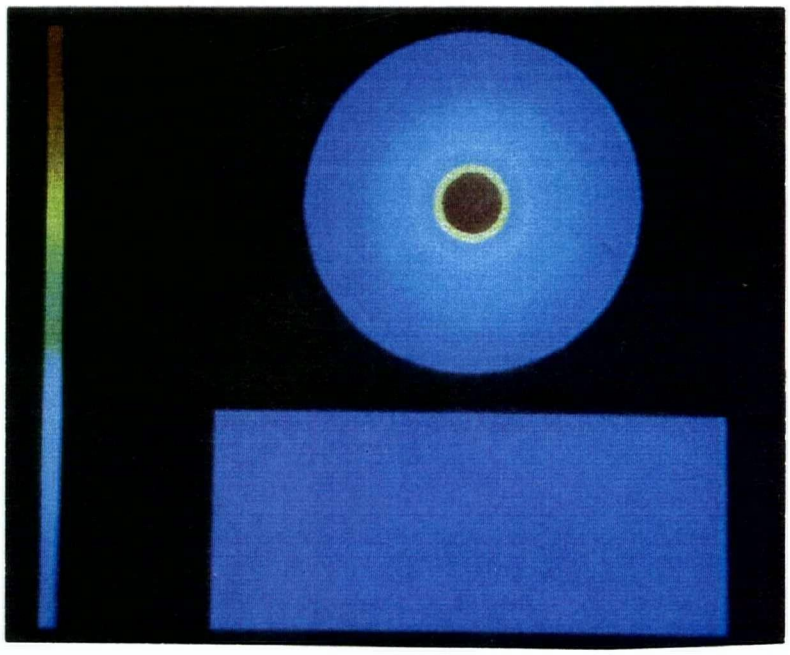

(a) Without surface charges.

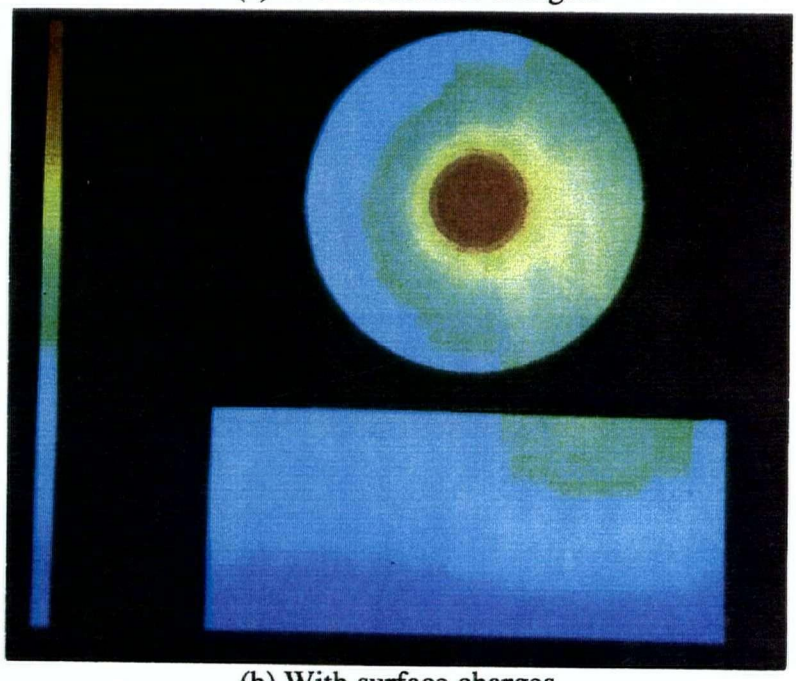

(b) With surface charges.

Figure 7.8 Surface potentials at 50 kV on nylon spacer surface in 0.3 MPa SF_6 gas with 3.2 mm diameter rod electrode and no gap between rod electrode and spacer.

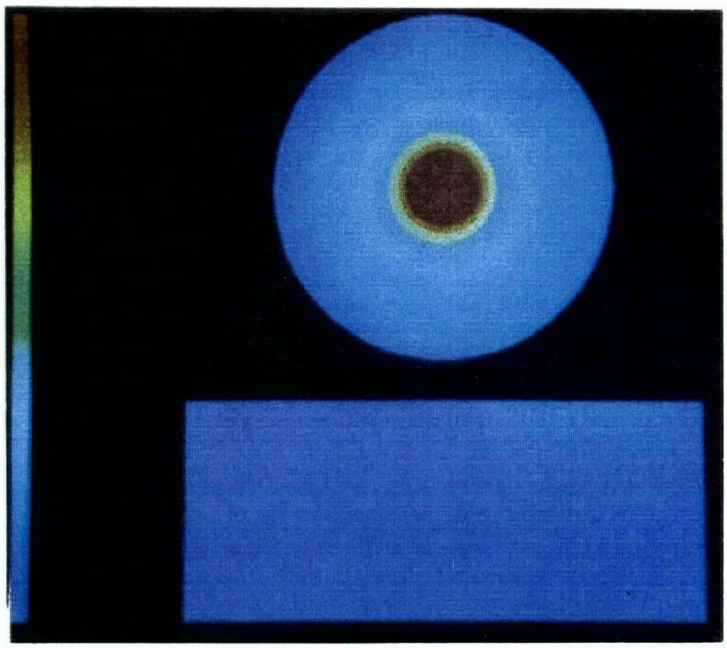

(a) Without surface charges.

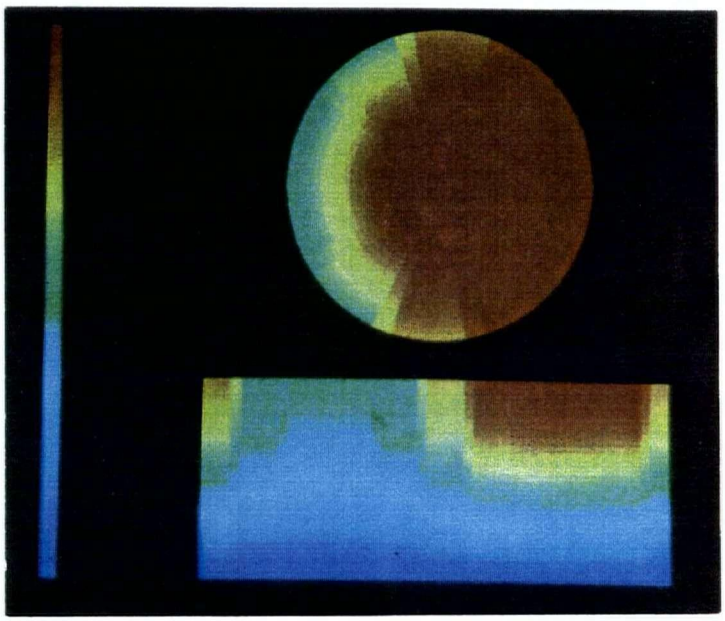

(b) With surface charges.

Figure 7.9 Surface potentials at 77 kV on nylon spacer surface in 0.3 MPa SF_6 gas with 3.2 mm diameter rod electrode and no gap between rod electrode and spacer.

are compared with the electric fields without the presence of surface charges for the spacer.

Figures 7.10 and 7.11 show that at a 99 kV lightning impulse voltage level surface charges do make a significant difference to the electric fields. On the top surface of the spacer, as shown in figure 7.10, the electric fields decreased on the center part of the surface and increased on the edge of the surface due to the surface charges. On the side surface of the spacer, as shown in figure 7.11, the electric fields increased significantly from the average of 3 kV/cm to approximately 10 kV/cm due to the surface charges.

From figures 7.10 and 7.11, it can be seen that with the presence of surface charges the lowest field on the entire surface is about 4.8 kV/cm. If the surface charges measured at 99 kV are used for the field calculation with 120 kV impulse voltage application, the calculated lowest electric field at flashover will be about 5.7 kV/cm. It is noted that the necessary ambient field for flashover propagation in SF_6 at 780 kPa appears to be rather small, below 10 kV/cm [55]. From these experimental results, it may be assumed that the flashover propagation field in SF_6 at a pressure of 0.3 MPa is between 5.7 kV/cm and 10 kV/cm.

Figures 7.12 and 7.13 show the magnitude of the total electric fields on PTFE spacer surface under four different voltage levels (99 kV, 77 kV, 60 kV, and 26 kV), with and without the effects of surface charges. With 26 kV impulse voltage, surface charges have little effect on the total electric field. This is because

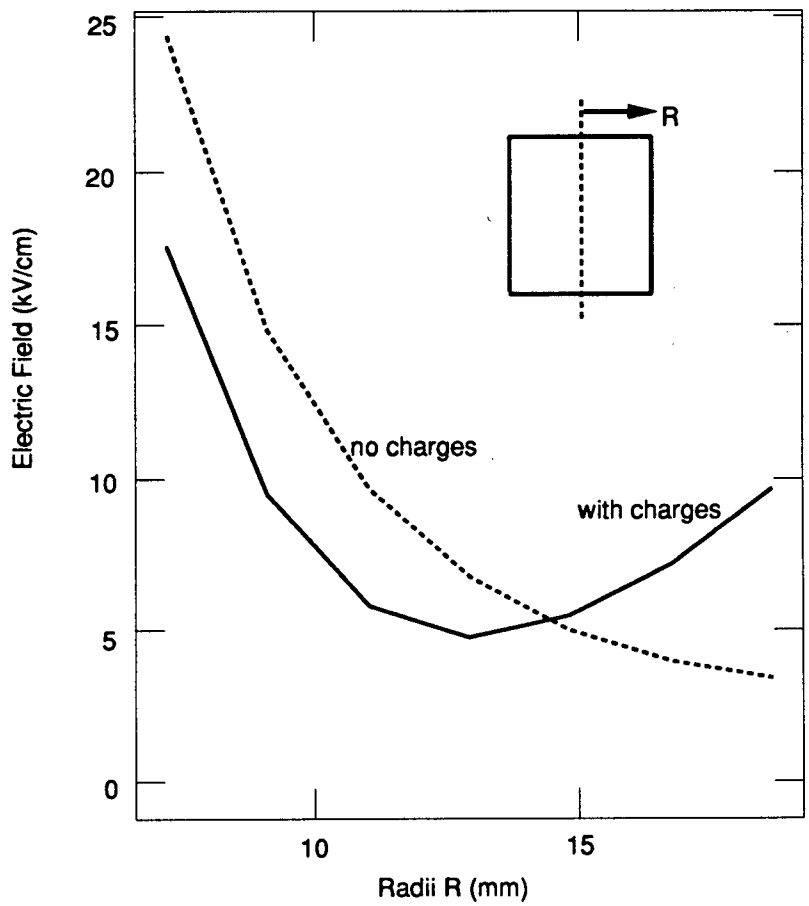

Figure 7.10 Magnitude of the total field at various positions on PTFE spacer top surface at 99 kV impulse voltage with 3.2 mm rod electrode in 0.1 MPa SF_6 gas.

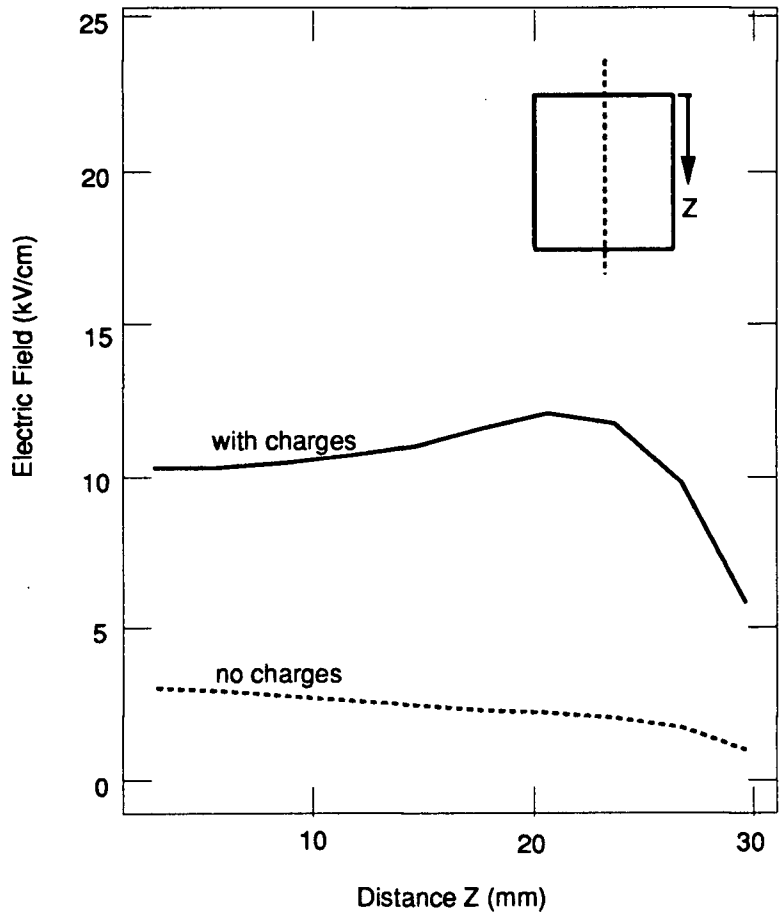

Figure 7.11 Magnitude of the total field at various positions on PTFE spacer side surface at 99 kV impulse voltage with 3.2 mm rod electrode in 0.1 MPa SF_6 gas.

at 26 kV there is no observable corona. All the surface charges measured with 26 kV impulse voltage application are initial residual charges with very low magnitude and negative polarity [81]. When the voltage is above the corona inception voltage, approximately 44.3 kV for the present geometry, there are dramatic changes in the charge distributions [81]. The changes in surface charges result in electric field perturbations. On the top surface of the spacer as shown in figure 7.12, the total electric fields near the edge increased significantly with the effect of surface charge. There is a cross over between the field distributions due to applied voltage alone and the field distributions due to both applied voltage and surface charges. With applied voltage increasing, the cross over point moves toward the center and the lowest electric field value increases. On the side surface of the spacer as shown in figure 7.13, the electric fields increase dramatically. For example, the electric field on the side surface at 60 kV with surface charges is even higher than the electric field at 99 kV without surface charges.

Surface charges not only change electric field magnitude, but also the directions at different points along the spacer surface. On the top surface of the spacer, in figure 7.14, the surface field due to applied voltage alone points into the spacer surface. However, with the surface charge present, the surface field directions are changed such that the angle between the field vector and the surface decreases and even reverses, i.e. the surface fields in regions close to the edge of the top surface point away from the surface. Therefore, the flashover may partially propagate

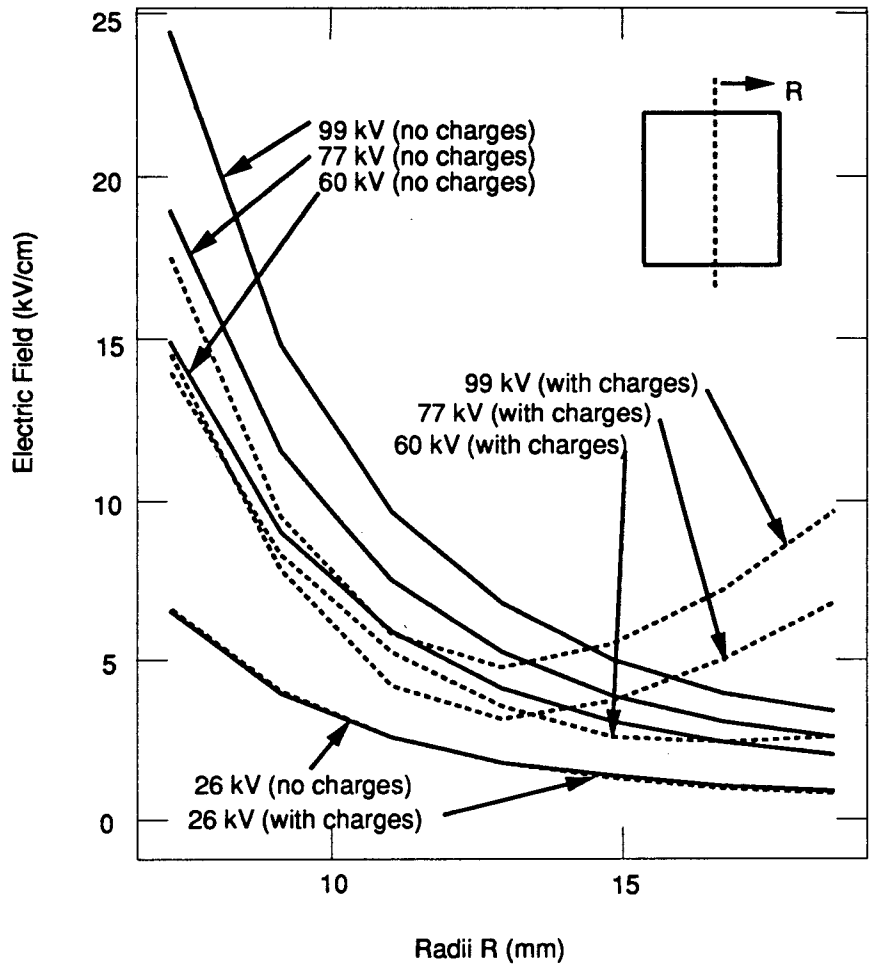

Figure 7.12 Magnitude of the total field at various positions on PTFE spacer top surface under impulse voltages with 3.2 mm rod electrode in 0.1 MPaSF_6 gas.

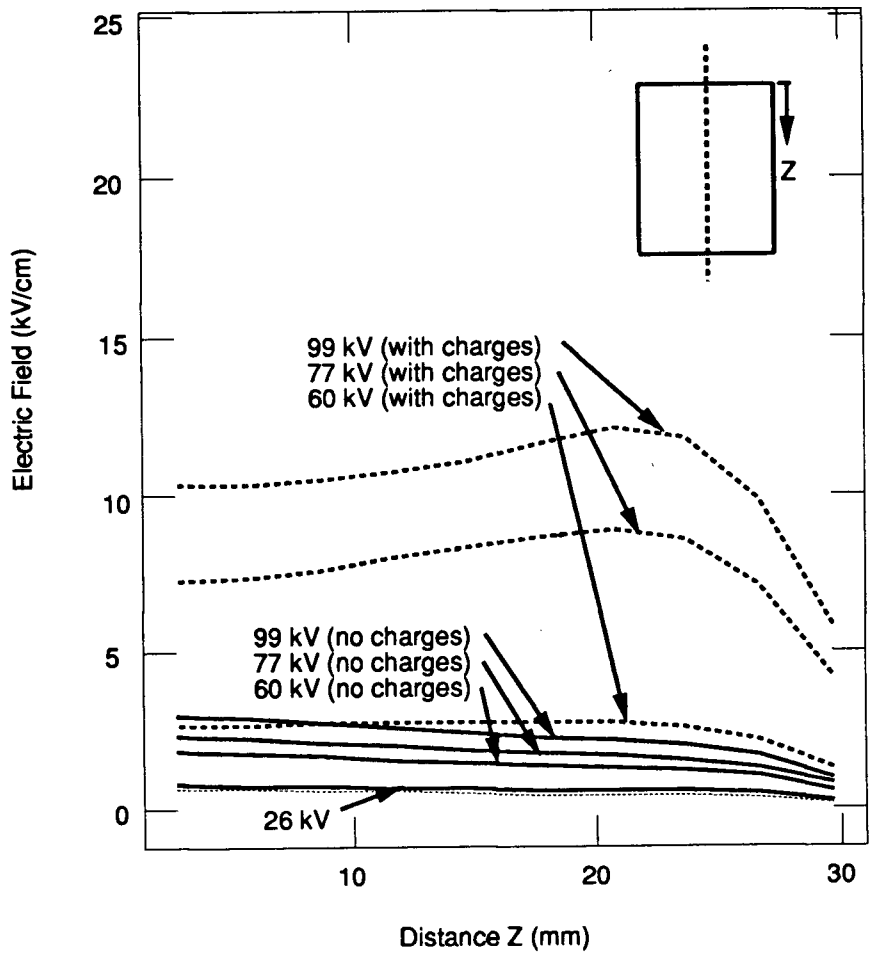

Figure 7.13 Magnitude of the total field at various positions on PTFE spacer side surface under impulse voltages with 3.2 mm rod electrode in 0.1 MPaSF_6 gas.

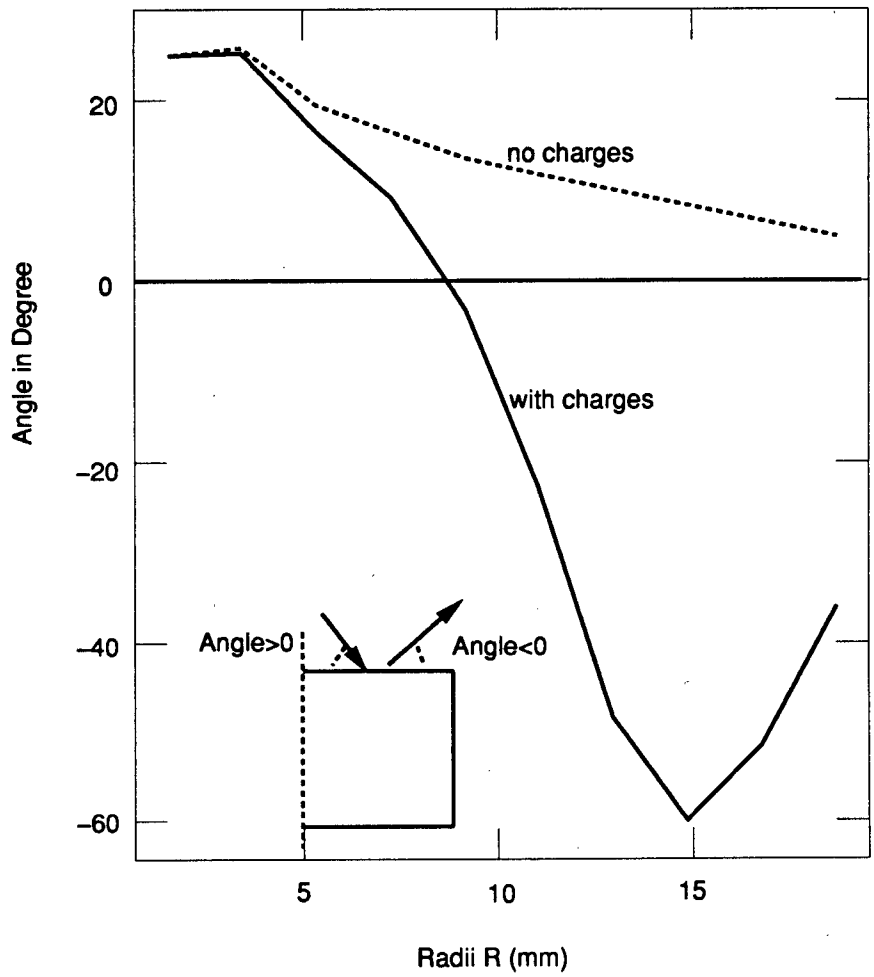

Figure 7.14 Electric field directions along the spacer top surface at 99 kV with 3.2 mm rod electrode in 0.1 MPa SF_6 gas.

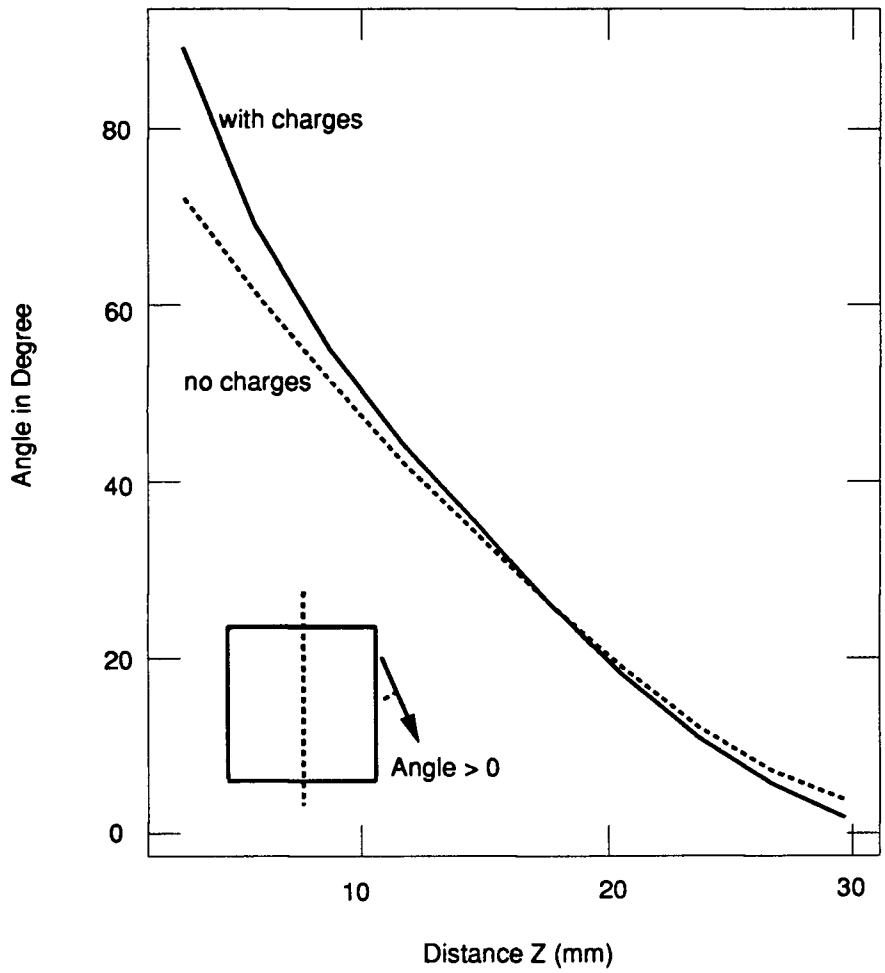

Figure 7.15 Electric field directions along the spacer side surface at 99 kV with 3.2 mm rod electrode in 0.1 MPa SF_6 gas.

along the surface, jump through the gas across the edge of the surface, and then along the side surface towards the ground electrode. On the side surface, in figure 7.15, the surface fields point away from the surface into the gas. The angle is defined as shown in the figure. Surface charges change the value of angles, and the total electric field in regions close to ground electrode is essentially parallel to the spacer surface. The decreased angle along the lower half of the side surface may make it much easier for the flashover to propagate towards the ground electrode. Similar electric field distributions were also observed on a nylon spacer surface.

7.4 Electric field with surface charges by opposite-polarity pre-charging

Surface charges may result in an increase or a decrease in flashover voltages [30] [80]. However, the flashover voltage of a highly charged spacer decreases considerably at the time of polarity reversal of the applied voltage [53]. This phenomena can be explained by reference to figure 7.16.

The surface charges used for the surface field calculations are from the measurements on a nylon spacer surface after a positive 77 kV impulse voltage application. The rod electrode diameter is 3.2 mm and there is no gap between the rod electrode and the spacer. There are three curves in figure 7.16. The solid curve is the applied field without surface charges on the spacer. The small dot curve is the total electric field with positive applied field and the surface charges due to positive pre-charging. The large dot curve is the total electric field with

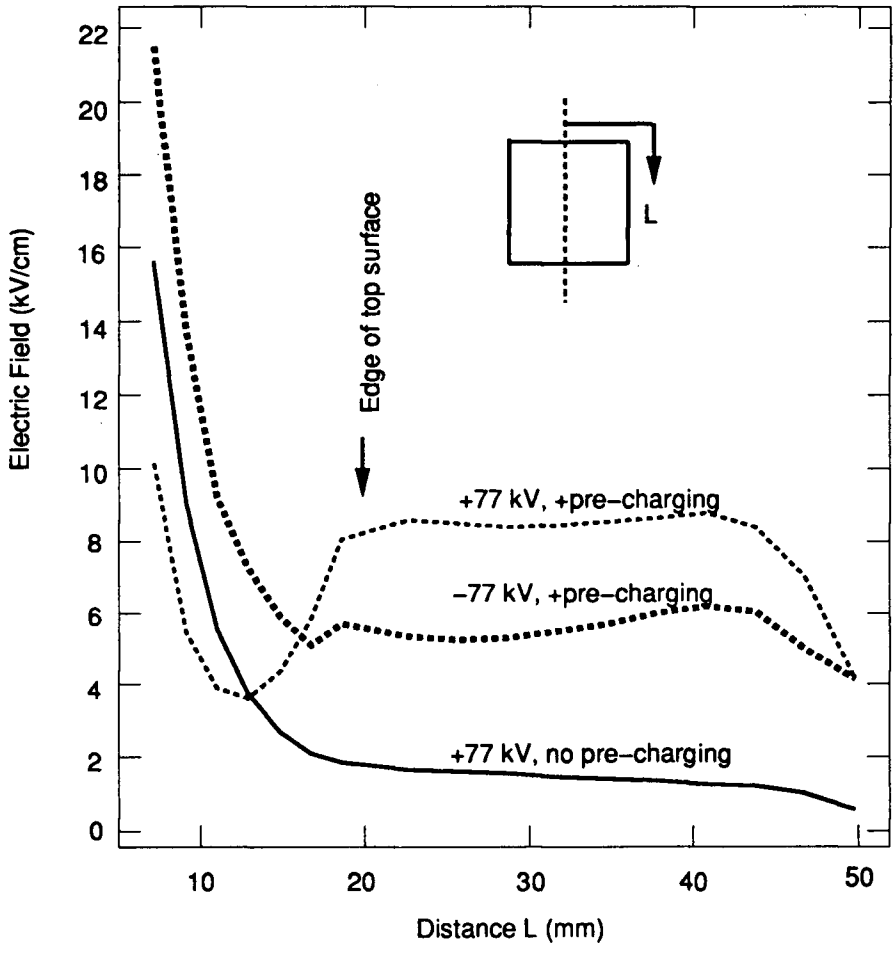

Figure 7.16 Magnitude of the total field at various positions on the nylon spacer surface under 77 kV impulse voltage with different pre-charging with 3.2 mm rod electrode in 0.1 MPa SF_6 gas.

negative applied field and the surface charges due to positive pre-charging, i.e. polarity reversal. The electric field intensity with polarity reversal is higher than the electric field intensity without surface charges all over the spacer surface. Since in SF_6 the ionization coefficients $\bar{\alpha}$ changes rapidly with small variations in electric field, such field enhancement can effectively increase the ionization yields of the second-generation auxiliary avalanches that may be started by some of the suitably located free electrons. Therefore, the intensified ambient electric field results in a lower flashover voltage.

With the same-polarity pre-charging, the electric field intensity decreases at the center near the rod electrode and increases on the rest of the surface. The reduction of electric field on the top surface may result in a higher flashover voltage than with the opposite-polarity pre-charging. The electric field intensity distribution and the location of the highest and lowest electric fields on the top surface of the spacer are critical for the final flashover voltage.

From the current measurements of surface charges [24], it is not clear how surface flashover propagates along the spacer surface after initiation close to the rod electrode. However, it is evident that the perturbations of surface fields due to surface charges play an important role on the flashover propagation.

7.5 Surface flashover of a spacer gap

Surface flashover is one of the major concerns in GIS and GITL systems.

In compressed gas insulated equipment solid insulators are necessary in order to support conductors. The interfaces between the compressed gas and the solid insulator may be one of the weakest points in such insulating arrangements. It was reported that with a geometry shown in figure 7.17, the flashover voltage in both N_2 and SF_6 is reduced by the insulator surface by about 10–15% [82]. The results for a coaxial conductor with a disc spacer and a composite-profile cone also show that the flashover voltage is reduced significantly by the insulating spacer [37]. For the geometry shown in figure 7.18, the flashover voltage decreases with opposite-polarity pre-charging and increases with same-polarity pre-charging [30]. It seems that insulating spacers may not always reduce the flashover voltage of a system and the flashover voltage largely depends on the insulating spacer geometry.

For the electrodes and spacer geometry used in this research shown in figure 4.1, $V_{50\%}$ flashover experiments were also done. The rod electrode diameter is 3.2 mm and there is no gap between the rod electrode and the nylon spacer. The experiments were conducted under three gas pressures (0.1 MPa, 0.2 MPa, and 0.3 MPa) in SF_6, air and N_2 gases. The results are shown in table 1.

Since the cylindrical spacer acts as an insulating barrier in a rod-plane electrode geometry, the flashover voltage values without spacer are generally lower than the flashover voltage values with a spacer. It is also interesting to note

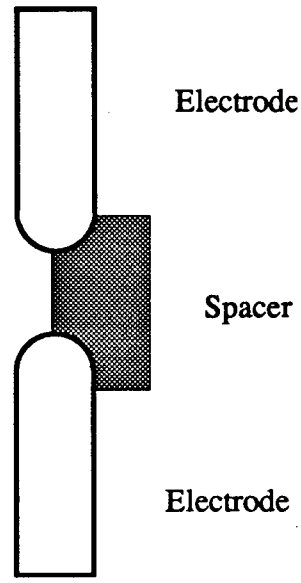

Figure 7.17 The cross section profile of the tested spacer in the reference [51].

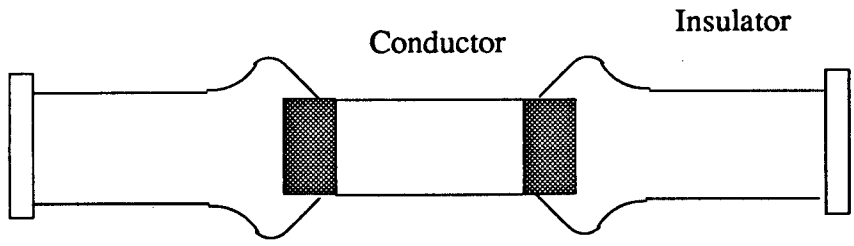

Figure 7.18 The cross section profile of the tested spacer in the reference [30].

Table 1. Flashover voltages under three gas pressures in SF_6, air and N_2.

Gas	Spacer	0.1 MPa	0.2 MPa	0.3 MPa
SF6	with spacer	122	121	123
	without spacer	61	83	95
Air	with spacer	53	62	61
	without spacer	46	57	66
N2	with spacer	36	54	50
	without spacer	23	31	45

that with a spacer present the breakdown voltage has a tendency to saturate as the gas pressure increases. This could be due to reverse discharges near the rod electrode [32] and also the saturation of the surface charge increases with the gas pressure, shown in figures 6.4 and 6.7–6.10. A more detailed analysis, coupled with high speed photographic observations, is needed to elucidate the interaction between surface charging and final stages of flashover. It may be worth noting that in practical GIS/GITL systems charged spacers may attract to the spacer surface any particle contamination present [83, 84] and such particle contaminations may cause lower flashover voltages.

Chapter 8

Summary and Conclusions

The object of this investigation has been to study the mechanisms and factors governing the magnitude and distribution of surface charges and their influence on flashover voltage. Surface charge accumulations on insulating spacer surfaces were studied experimentally with a rod-spacer-plane geometry under different experimental conditions such as ambient fields, gas pressures and duration of applied voltages. Surface charge fields were then calculated using the surface charge simulation program. From the experimental and calculation results, the following summary of observations and conclusions is made.

8.1 Surface charge accumulation

In order to study where surface charges come from and how surface charges are affected by certain environmental conditions, a series of experiments were designed and conducted.

First, surface charge accumulations versus corona were studied. Charge patterns were measured under lightning impulse voltages, with different levels, and

then compared with the corresponding calculated corona inception voltages. It was observed that surface charge density on the spacer surface increases dramatically at approximately the calculated corona inception voltage, which strongly suggests that the onset of corona causes the observed charge deposition. Moreover, for applied voltages well above the corona inception the observed charge density peak tends to saturate with voltage and gas pressure, figures 6.4, 6.7 to 6.10. The charge distribution becomes more and more non-uniform as the applied voltage and gas pressure increase. This indicates that perhaps local surface discharges take place on each impulse voltage application.

The experimental results are also analyzed in terms of gas pressures. For an electronegative gas such as SF_6, when the applied voltage level is close to and a little higher than the corona inception, surface charge magnitudes are significant and are lower at higher gas pressures, figure 6.5. When the applied voltage level is much higher than the corona inception, surface charge magnitudes increase with gas pressure and then start to saturate as the gas pressure reaches a certain value, figure 6.6. Also, inhomogeneity in surface charge distributions for both nylon and PTFE spacers increases with gas pressures. However, for nitrogen gas, surface charge magnitude is lower at higher gas pressures even at voltage levels much higher than the corona inception, figures 6.13 and 6.14. Under higher gas pressures, ionization by collision does not occur easily because of the shorter mean free path. Therefore, at a given applied voltage surface charge magnitude is

lower at higher gas pressures due to the higher corona inception. When the applied voltage is much higher than the corona inception voltage, avalanches progress. The negative ions in an electronegative gas, such as SF_6, have shorter lifetime at higher gas pressures where the collision frequency and energy exchanged are high. Furthermore, photo-detachment of negative ions is higher at high gas pressure because the number of photons increases with gas pressure. Therefore, more surface charges are observed on a spacer at higher gas pressures in electronegative gases.

Under uniform field conditions, insulating spacers subjected to impulse voltages in SF_6 do not acquire significant surface charges [24]. However, defects present on a spacer or the electrode surface can cause charge depositions. The reason is that in a uniform field the corona inception voltage is so high that it is almost the same as the flashover voltage of the system and no significant surface charges will be seen before observable corona and breakdown occur. In a non-uniform field, corona inception and avalanche propagation depend on electric field distribution. Corona occurs where the electric field magnitude is significantly high and avalanches propagate in the directions of the electric fields. The avalanches may stop where the electric fields are too weak. Therefore, very non-uniform electric field distribution causes non-uniform surface charge distribution and high surface charge magnitudes. This was confirmed by the experimental results shown in figures 6.15-6.17.

A GIS system is stressed with the rated AC voltage under normal operating conditions. However, switching or lightning transients can appear on a system under abnormal conditions. At rated AC voltage, charge deposition may occur on an insulating spacer surface. An impulse transient on the system can also cause charge deposition on the insulating spacer surface. How do the surface charges caused by the rated voltage affect the flashover of the system when an impulse transient appears on the system? How do the surface charges caused by an impulse transient under an abnormal condition affect the normal operation? The first question was answered by AC pre-charging experiments conducted in previous work [24]. The results show that the variation of the flashover voltage and the time to flashover due to the surface charges by AC pre-charging falls well within the statistical scatter for positive impulse with no AC pre-charging. The second question was answered in this research. Assume that a spacer is stressed twice. The first impulse application voltage is called the pre-charging voltage. It was found that if the pre-charging voltage is lower than the subsequent impulse voltage, the final charge pattern will be determined by the second impulse voltage. If the pre-charging voltage is higher than the subsequent impulse voltage, the final charge pattern will be determined by the pre-charging voltage. The dynamic stable charge pattern established during the pre-charging on a spacer surface does change significantly due to a higher subsequent impulse voltage application. Therefore, the surface charges caused by larger magnitude impulse transients may prove to

be dangerous under normal operation.

It was reported that similar surface charge patterns were observed under both switching and lightning impulse voltages [24]. The experiments with lightning impulses and DC for 5 minutes and 30 minutes were conducted in this work to study the effect of the duration of applied voltage on surface charging. The results, figure 6.21, show that much higher surface charge density was observed under a 5 minute DC voltage than a lightning impulse with the same voltage level. The results of experiments with 30 minute DC charging do not show much difference with the results of 5 minute DC with the same voltage level. It takes time for ions around the rod electrode to move to the surface of a spacer. With lightning impulse application, only the ions from the tip of the rod electrode, which are in the highest electric field and have shortest distance to travel, may move along the axis to deposit on the center of the surface. With 5 minute DC voltage application, the duration of voltage application is long enough for positive ions around the rod electrode to travel along the electric field directions and deposit on the spacer surface. The electric field due to these surface charges distorts the overall electric field, especially reducing the electric field around the rod electrode, and inhibiting corona around that area. Therefore, after a certain period of a voltage application, a saturation level of deposited charge for a given applied voltage level will be obtained.

Experiments were conducted with three different gases (air, SF_6, and N_2)

under DC voltages. A 4 mm gap was introduced between the rod electrode and the top surface of the spacer. Comparison of the charge patterns are shown in figures 6.22-6.24. Figures 6.22 and 6.24 show that the charge patterns in SF_6 are significantly different from the charge patterns in air and N_2, while figure 6.23 shows that the charge patterns in air and N_2 gases are similar. At a given voltage the surface charges in SF_6 have much lower charge density and become significant at higher voltage levels. The calculated corona inception voltages for the three gases are very close: 12 kV in air, 13 kV in N_2, and 15 kV in SF_6. The main reasons for the big difference in charge patterns may be the strong electronegative characteristic of SF_6 gas. In a very non-uniform field, especially under DC voltage applications, corona-stabilization is present in electronegative gases. Free electrons caused by corona in SF_6 attach to neutral atoms or molecules so that negative ions are formed. An ample space charge of negative ions accumulates around the anode and decreases the electric field between negative ion space charges and the plane electrode so that the progress of streamers towards a spacer surface is inhibited. Therefore, less charges accumulate in SF_6 gas.

The following conclusions can be made from the above summary:

1. Surface charging is directly related to the corona phenomena in the space between the rod electrode and the top surface of the spacer. The surface charge density increases significantly when the applied voltage reaches a

critical value and increases thereafter with the applied voltage. This critical voltage is determined by the onset of corona for a particular gas pressure and spacer material.

2. For electronegative gases, when the applied voltage is much higher than the corona inception, charge densities are higher under higher gas pressures, suggesting that photoionization may be one of the mechanisms for surface charges at high gas pressures and high voltages.
3. By varying the non-uniformity of ambient electric field, it was found that surface charge magnitude and distribution are very much field dependent. Greater field non-uniformity increases the non-uniformity of surface charge distribution and the charge magnitude.
4. Pre-charging studies show that with a series of impulse voltage applications on a spacer, the surface charge magnitudes are determined by the applied voltage with the highest magnitude. However, the surface charge distributions are slightly redistributed due to local discharges after each voltage application.
5. Experiments with lightning impulse and DC voltages show that the surface charging is related to the duration of a voltage application. A certain time is required for ions to travel from the rod electrode to the spacer surface.
6. Experiments with three different gases (SF_6, air, N_2) show that the charge patterns in SF_6 are very different from the charge patterns in air and N_2, which are similar. At a given DC voltage, there is much less charge magnitude

on spacer surface in SF_6 gas, suggesting that corona-stabilization plays an important role on surface charging in non-uniform field.

8.2 Surface Charge Field Analysis

Surface charge fields are calculated by the SSM program. The results in figures 7.4-7.6 show that surface charges do make significant differences to the overall electric fields. This is likely to be the reason that surface charges change the flashover voltages of GIS systems.

With the surface charges from same-polarity pre-charging, the electric fields on the edge of a PTFE spacer top surface are enhanced, while the electric field on the center of the spacer top surface are weakened, figure 7.10. The electric fields on the spacer side surface are enhanced from an average value of 3 kV/cm to approximately 10 kV/cm at 99 kV, figure 7.11. The minimum value of the surface field on the top surface increased by about 45% from 3.3 kV/cm to 4.8 kV/cm at 99 kV.

Surface charges not only change the electric field magnitudes, but also the electric field directions. The inclination of electric field on the top surface of spacer decreases in the radial direction due to surface charges, figure 7.14, and the electric field directions reverse and point away from the surface into the gas near the edge of the top surface. Beyond the spacer edge and along the side surface,

the electric field directions point away from the surface and the angles decrease, making the field almost parallel to the side surface near the plane electrode.

With opposite-polarity pre-charging, the electric fields over the entire spacer surface are enhanced considerably. Therefore, the flashover voltage of a highly charged spacer decreases noticeably at the time of polarity reversal of the applied voltage.

The following conclusions can be made from the above summary:

1. Surface charges on spacer surfaces do make significant differences to the surface electric fields. For example, the minimum surface field on a PTFE spacer top surface at 99 kV increases by about 45% from 3.3 kV/cm to 4.8 kV/cm.
2. The flashover propagation field on a PTFE spacer surface may be between 6 kV/cm and 10 kV/cm.
3. Surface charges on spacer surface distort the total surface field directions. This may make flashover partially propagate along the surface, jump across the edge of the surface through the ambient gas to reach the opposite electrode.
4. The electric field intensity all over the spacer surface at the time of polarity reversal is higher than the electric field intensity without the effect of surface charges. This results in lowering the flashover voltage of a system.
5. The decrease of the electric field on the center of the top surface with same-

polarity pre-charging may result in a higher flashover voltage than that with opposite-polarity pre-charging.

8.3 Suggestions for future research

The present work has shown that surface charges significantly distort electric fields and may explain the anomalous flashover in GIS systems. The mechanism of surface charges are identified to be corona, gas conduction, and photoionization.

In this research, two different materials were used, namely PTFE and nylon. The significant difference in charge patterns between PTFE and nylon may not be fully explained only by the different dielectric constants. Further research is needed to study the role of spacer materials on surface charging and the interaction of spacer surfaces with developing discharges. Perhaps, suitable spacer materials or spacer coatings could be identified, which trap less surface charges or provide quick dissipation of any accumulated charges.

Experiments with lightning impulse and DC voltages show that a certain period of time is required for ions to travel from the rod electrode to deposit on a spacer surface. The experiments conducted so far do not permit an accurate estimation of the duration of this transient period. A possible solution could be to use transient corona current measurements to correlate the deposited charges with the measured current.

For future research, it is important to know how a flashover propagates along a spacer surface. An image intensifier is suggested to visually observe the propagation. Therefore, the propagation pattern can be compared with the actual electric field distribution pattern to build a reasonable model to predict spacer flashover in SF_6 gas.

References

[1] S. A. Boggs, "Canadian experience with gas-insulated switchgear," CEA Position Paper February, Ontario Hydro Research, 1982.

[2] R. F. Swoish *et al.*, "The environmental and technical aspects of terminating HV to UHV connections at substations," Paper 23.08 , Paris, CIGRE, 1976.

[3] "Compressed gas cables in use internationally," Electra No. 94 , pp. 55-56, CIGRE Working Group 21.12, 1984.

[4] A. H. Cookson, "Compressed gas insulated transmission lines: the present and the future," in *Gaseous Dielectrics I*, (Pergamon Press), pp. 198–201, 1978.

[5] H. W. Graybill and J. A. Williams, "Underground power transmission with isolated phase gas insulated conductors," *IEEE Transaction on Power Apparatus and Systems, Vol. PAS-89*, pp. 17–23, 1970.

[6] B. O. Pedersen *et al.*, "Development of compressed gas-insulated transmission lines," *IEEE Transaction on Power Apparatus and Systems, Vol. PAS-90*, pp. 2631–2640, 1971.

[7] A. H. Cookson, "Gas-insulated cables," *IEEE Transaction on Electrical Insulation, Vol. EI-20, No. 5*, pp. 859–890, October, 1985.

[8] S. A. Boggs, F. Y. Chu, and N. Fujimoto, "Gas insulated substations," in *Proceedings of the Third International Symposium on GIS*, (Toronto, Pergamon Press), 1985.

[9] T. W. Dakin and D. Berg, "Theory of gas breakdown," in *Progress in Dielectrics, Vol. 4*, (London, Heywood & Co.), pp. 153–198, 1962.

[10] J. M. Braun, F. Y. Chu, and R. Seethapathy, "Characterization of gis-spacer exposed to SF_6 decomposition products," *IEEE Transactions on Electrical Insulation, Vol. EI-22*, pp. 187–193, 1987.

[11] F. Y. Chu and V. Tahiliani, "Gas-insulated substations fault survey," *IEEE Transactions on Power Apparatus and Systems, Vol. PAS-99, No. 6*, pp. 2351–2356, Dec. 1980.

[12] J. G. Trump and J. Andrias, "High voltage dc flashover of solid insulators in compressed nitrogen," *Trans. AIEE 40*, pp. 986–989, 1941.

[13] T. Takuma, T. Watanabe, and T. Kuomo, "Effect of a narrow gas gap on the surface flashover of spacer in SF_6," in *International Symposium on High Voltage Engineering*, (Zurich), pp. 440–450, 1975.

[14] V. R. Laghari and A. H. Quereshi, "Flashover studies of cylindrical spacers in SF_6 and N_2 mixtures," in *IEEE Power Engg. Society Winter Meeting*, (New York, USA), Paper No. A80-055-4, 1980.

[15] T. Nitta *et al.*, "Factors controlling surface flashover in SF_6 gas insulated systems," *IEEE Transactions on Power Apparatus and Systems, Vol. PAS-97*, pp. 959–965, 1978.

[16] C. M. Cooke *et al.*, "Compressed gas insulation for advanced $HVDC$

transmission equipment," in *CIGRE Insulation Session*, (Paris), March 1982.

[17] H. Kuwahara *et al.*, "Effect of solid impurities on breakdown in compressed SF_6 gas," *IEEE Transactions on Power Apparatus and Systems, Vol. PAS-93, No. 5*, pp. 1546–1555, 1974.

[18] M. Hara and M. Akazaki, "A method for prediction of gaseous discharge threshold voltage in the presence of a conducting particle," *Journal of Electrostatics, Vol. 2*, pp. 223–239, 1976/1977.

[19] H. Parekh and K. D. Srivastava, "Breakdown voltage in particle contaminated compressed gases," *IEEE Transactions on Electrical Insulation, Vol. EI-14, No. 2*, pp. 101–106, 1979.

[20] H. Parekh, K. D. Srivastava, and R. G. van Heeswijk, "Lifting field of free conducting particles in compressed SF_6 with dielectric coated electrodes," *IEEE Transactions on Power Apparatus and Systems, Vol. PAS-98, No. 3*, pp. 748–758, 1979.

[21] H. C. Doepken, "Compressed gas insulation in large coaxial systems," *IEEE Transactions on Power Apparatus and Systems, Vol. PAS-88*, pp. 364–369, 1969.

[22] A. H. Cookson, "Recent research in the united states on the effect of particle contaimination reducing the breakdown voltage in compressed gas insulated systems," in *CIGRE*, (Paris), Paper 15.09, 1976.

[23] A. H. Cookson, "Review of high-voltage gas breakdown and insulators in compressed gas," *IEE Proceedings, Vol. 128, Pt. A, No. 4*, pp. 303–312, 1981.

[24] S. E. Cherukupalli, *Surface charges accumulation on spacers under switching impulses in sulphur hexafluoride gas*. PhD thesis, University of British Columbia, July, 1987.

[25] A. H. Cookson in *Sixth IEE Conference on Gas Discharges and Their Applicationa - review Lectures*, (Edinburgh), pp. 21–43.

[26] T. Stoop, J. Tom, H. F. A. Verhaart, and A. J. L. Verhage, "The influence of surface charges on flashover of insulators in gas-insulated systems," in *Fourth International Symposium on High Voltage Engineering*, (Athens), Paper 32.10, 1983.

[27] C. W. Mangelsdorf and C. E. Cooke, "Bulk charging of epoxy insulators under dc stress," in *IEEE International Symposium on Electrical Insulation*, (Boston, USA), pp. 146–149, 1980.

[28] A. Knecht, "Development of surface charges in epoxy resin spacers stressed with dc voltage," in *Gaseous Dielectrics III*, (Pergamon Press), pp. 356–362, 1982.

[29] K. Nakanishi, Y. Yoshioka, and Y. Arahata, "Surface charging on epoxy spacer at dc stress in compressed SF_6 gas," *IEEE Transactions on Power Apparatus and Systems*, vol. PAS-102, No. 12, pp. 3919–3926, Dec. 1983.

[30] C. Y. Yu, S. Rusck, and A. E. Vlastos, "The influence of charge accumulation on the impulse falshover of spacers in compressed SF_6," in *Fourth International Symposium on High Voltage Engineering*, Paper No. 34-06, 1983.

[31] V. N. Maller and K. D. Srivastava, "Corona discharge studies in SF_6 with insulators under positive switching impulse," *IEEE Transactions on Electrical Insulation, Vol. EI-18, No. 5*, pp. 528–535, 1983.

[32] M. A. Abdul-Hussain and K. J. Cornick, "Charge storage on insulation surfaces in air under unidirectional impulse conditions," *IEE Proceedings, Vol. 134, Pt. A, No. 9*, pp. 731–740, November, 1987.

[33] H. F. A. Verhaart, J. Tom, A. J. L. Verhage, and C. S. Voss, "Avalanches near solid insulators," in *Fifth International Symposium on High Voltage Engineering*, (Braunschweig), Paper 15-02, 1987.

[34] V. N. Maller and K. D. Srivastava, "Effect of field non-uniformity on time-to-corona inception in SF_6 with insulator," in *Gaseous Dielectrics IV*, (Pergamon Press), pp. 99–104, 1984.

[35] J. B. Neilson, K. D. Srivastava, S. R. Naidu, and P. T. de Madeiros, "Spacer flashover time lags in SF_6 under fast front impulse voltages," in *Gaseous Dielectrics V*, (Pergamon Press), pp. 445–451, 1987.

[36] T. Tsukiji, T. Matsumoto, and T. Matsumoto, "The effect of charges remaining on a dielectric plane upon the 50% impulse surface flashover," in *IEEE*

Conference on Interfacial Phenom. in Practical Insulating Systems, Natl. Bur. of Stand., IEEE Pub. 83CH1946-3, (USA), pp. 53–57, 1983.

[37] N. G. Trinh, G. Mitchel, and C. Vincent, "Influence of an insulating spacer on the v-t characteristics of a coaxial gas-insulated cable part 1: Study on a reduced-scale coaxial conductor," *IEEE Transactions on Power Delivery, Vol. 3, No. 1*, pp. 16–25, January, 1988.

[38] S. E. Cherukupalli, K. Tsuruta, and K. D. Srivastava, "Mechanism of pre-breakdown spacer charging in non-uniform fields under unidirectional voltages," *IEEE Transactions on Electrical Insulation, Vol. EI-25, No. 4*, pp. 642–654, 1990.

[39] H. Parekh and K. D. Srivastava, "Some computations and observations on corona stabilized breakdown in SF_6," *IEEE Transactions on Electrical Insulation, Vol. EI-15*, pp. 87–94, 1980.

[40] O. E. Ibrahim and O. Farish, "Impulse breakdown and pre-breakdown corona processes in SF_6 and SF_6/N_2 mixtures," in *Gaseous Dielectrics II*, (Pergamon Press), pp. 356–364, 1980.

[41] B. H. Crichton, D. Blair, and D. I. Lee, "Pre-breakdown phenomena in SF_6 at high pressures in uniform-field gaps with anode-mounted projections," in *Proc. of Second International Conference on Gas Discharges*, (IEE Pub. No. 189, Part I), pp. 5–8, 1980.

[42] H. Anis and K. D. Srivastava, "Breakdown on rod-plane gaps in SF_6 under switching impulses," in *IEEE Transactions on Power Apparatus and Systems, Vol. PAS-101, No. 3*, pp. 537–546, 1981.

[43] H. Anis and K. D. Srivastava, "Pre-breakdown discharges in rod-plane gaps in SF_6 under positive switching impulses," *IEEE Transactions on Electrical Insulation, Vol. EI-16*, pp. 552–563, 1981.

[44] A. Knecht, "Development of surface charges on epoxy resin spacers stressed with direct applied voltages," in *Gaseous Dielectrics III*, (Pergamon Press), pp. 356–364, March 1982.

[45] K. Nakanishi, A. Yoshioka, and Y. Shibuya, "Charge accumulation on spacer at dc stress in compressed SF_6 gas," in *Gaseous Dielectrics III*, (Pergamon Press), pp. 365–373, March 1982.

[46] H. Fujinami, M. Yashima, and T. Takuma, "Mechanism of the charge accumulation on gas insulated spacers under dc stress," in *Fifth International Symposium on High Voltage Engineering*, (Braunschweig, F. R. of Germany), Paper No. 13.02, 1987.

[47] H. Ootera, K. Nakanishi, and Y. Shibuya, "Measurement of charge accumulation on control spacer for 500 kV DC GIS," in *Fourth International Symposium on High Voltage Engineering*, Paper No. 52, 1983.

[48] O. Yamamoto, T. Hara, and M. Matumura, "Space charge distribution of

surface discharge in SF_6 gas," Mem. Fac. Eng. vol. 48, No. 4, Kyoto University, 1986.

[49] K. Tsuruta, S. E. Cherukupalli, and K. D. Srivastava, "Charge accumulation on spacers in non-uniform field SF_6 gaps under dc and lightning impulse voltages," in *IEEE International Symposium on Electrical Insulation*, (Washington DC, USA), Paper F5, 1988.

[50] A. H. Cookson, "Review of high-voltage gas breakdown and insulators in compressed gas," *IEEE Proceedings, Vol. 128, Pt. A, No. 4*, pp. 303–312, 1981.

[51] W. Pfeiffer, M. Giesselmann, and P. Volker, "Spatial and temporal predischarge development at insulator surfaces in compressed gases," *IEEE Gas Discharges*, pp. 277–279, 1980.

[52] J. R. Laghari and A. H. Qureshi, "Surface flashover of spacers in compressed gas insulated systems," *IEEE Transaction on Electrical Insulation, Vol. EI-16, No. 5*, pp. 373–387, October, 1981.

[53] T. Takuama, "Discharge characteristics of gaseous dielectrics," *IEEE Transactions on Electrical Insulation, Vol. EI-21, No. 6*, pp. 855–867, December, 1986.

[54] H. F. A. Verhaart and A. J. L. Verhage, "Insulator falshover in SF_6 gas," Kema Scientific & Technical Report 6 (9), 1988.

[55] C. M. Cooke, "Surface flashover of gas/solid interfaces," in *Gaseous Dielectrics III*, (Pergamon Press), pp. 365–373, March 1982.

[56] E. Nasser, *Fundamentals of Gaseous Ionization and Plasma Electronics.* Ames, Iowa: Wiley-Interscience, 1971.

[57] J. M. Meek and J. D. Craggs, *Electrical Breakdown of Gases.* University of Liverpool: John Wiley & Sons, 1978.

[58] R. E. Hebner, R. A. Malewski, and E. C. Cassidy, "Optical methods of electrical measurements at high voltage levels," *IEEE Proceedings, Vol. 65*, pp. 1524–1548, 1977.

[59] R. Lee, H. Rhinehart, H. Thompson, and T. S. Sudarshan, "Pre-discharge current measurements and optical surface measurements associated with insulator surface flashover," in *Gaseous Dielectrics III*, (Pergamon Press), pp. 349–355, 1982.

[60] P. E. Secker, "The design of simple instruments for measurement of charge on insulating surfaces," *Journal of Electrostatics, Vol. 1*, p. 27, 1975.

[61] T. R. Foord, "Measurement of the distribution of surface electric charge by use of a capacitive peobe," *Journal of Scientific Instruments (Journal of Physics E), Vol. 2*, pp. 411–413, 1969.

[62] M. Yashima, H. Fujinami, and T. Takuma, "Measurement of accumulated charge on dielectric surfaces with an electrostatic probe," in *Gaseous*

Dielectrics V, (Pergamon Press), pp. 242–248, May 3-7 1987.

[63] A. Pedersen, "On the electrostatics of probe measurements fof surface charge densities," in *Gaseous Dielectrics V*, (Pergamon Press), pp. 414–420, May 3-7 1987.

[64] P. Connolly and O. Farish in *Gaseous Dielectrics IV*, (Pergamon Press), pp. 405–412, 1984.

[65] A. Pedersen, "On the electrostatic field ofr a charged surface of an insulator with spacial reference to surface charge probe measurements," in *Gaseous Dielectrics IV*, (Pergamon Press), pp. 414–420, 1984.

[66] J. Zhou, S. E. Cherukupalli, and K. D. Srivastava, "Surface charging of insulators in SF_6 at different pressures under impulse voltages," in *Canadian Conference on Electrical and Computer Engineering*, (Vancouver, BC, Canada), pp. 39–44, November 1988.

[67] X. Zhang, J. Zhou, and K. D. Srivastava, "D.c. corona charging of insulating surfaces," in *Canadian Conference on Electrical and Computer engineering*, (Montreal, PQ, Canada), pp. 881–884, September 1989.

[68] S. Sato and B. Bachmann, "A three dimension high speed surface charge simulation method (3d-hsssm)," in *Fourth International Symposium on High Voltage Engineering*, Paper No. 11.08, 1983.

[69] S. Sato, *Effective three-dimensional electric field analysis by surface charge*

simulation method. PhD thesis, Swiss Federal Institute of Technology, 1987.

[70] S. Sato, "Effective 3-dimensional electric field calculation by surface charge simulation method," *IEE Proceedings, Vol. 133, Pt. A, No. 2*, pp. 77–83.

[71] H. Singer, "Flachenladungen zur felberechnung von hochspannungssystemen," *Bull SEV/VSE*, vol. 65, 10, pp. 739–746, 1974.

[72] T. Misaki, H. Tsuboi, and K. Itaka, "An analysis of three-dimension field problems by surface charge method and its application," *Electrical Engineering in Japan*, vol. 101, No. 5, pp. 24–31, 1981.

[73] T. Misaki, H. Tsuboi, and K. Itaka, "Computation of three-dimension electric field problems by a surface charge method and its application to optimum insulator design," *IEEE Transactions on Power Apparatus and Systems, Vol. PAS-101, No.3*, pp. 627–634, 1982.

[74] H. Singer, H. Steinbigler, and P. Weiss, "A charge simulation method for the calculation of high voltage fields," *IEEE Transactions on Power Apparatus and Systems, Vol. PAS-93*, pp. 1660–1668, 1974.

[75] S. Kato, "An estimation method for the electric field error of a charge simulation method," in *Third International Symposium on High Voltage Engineering*, (Milan), August Paper 11.09, 1979.

[76] T. Shimazaki and I. Tsuneyasu, "Flashover processes on the surface of solid insulators under positive impulse voltage in the atmosphere," *IEEE*

Transactions on Electrical Insulation, Vol. EI-25, No. 6, pp. 1161–1169, 1990.

[77] J. M. Meek and J. D. Craggs, *Electrical Breakdown of Gases*. Wiley-Interscience, 1978.

[78] L. B. Loeb, *Basic processes of Gaseous Electronics*. California: University of California, 1955.

[79] C. M. Cooke, "Charging of insulator surfaces by ionization and transport in gases," *IEEE Transactions on Electrical Insulation, Vol. EI-17, No. 2*, pp. 172–178, 1982.

[80] L. Niemeyer and F. Pinnekamp, "Surface discharge in SF_6," in *Gaseous Dielectrics III*, (Pergamon Press), pp. 379–385, March 1982.

[81] A. H. Cookson, "Review of high-voltage gas breakdown and insulators in compressed gas," *IEE Proceedings, Vol. 128, Pt. A, No.4*, pp. 303–312, May, 1981.

[82] A. H. Cookson, "Recent research in the united states on the effect of particle contamination reducing the breakdown voltage in compressed gas insulated systems." CIGRE, Paris, paper 15.09, 1976.

[83] A. K. Chakrabarti, R. G. V. Heeswijk, and K. D. Srivastava, "Spacer involvement in conducting particle initiated breakdown in compressed gas insulated systems," *IEEE Transactions on Electrical Insulation, EI-22, No. 4*, pp. 431–438, 1987.

[84] A. K. Chakrabarti, R. G. V. Heeswijk, and K. D. Srivastava, "Free particle initiated breakdown of a spacer surface in a gas insulated bus," *IEEE Transactions on Electrical Insulation, Vol. EI-24, No. 4*, pp. 549–560, 1989.